

THESIS FOR THE DEGREE OF LICENTIATE OF ENGINEERING

**The influence of modelling parameters  
on the simulation of car tyre rolling losses and  
rolling noise**

CARSTEN HOEVER

Department of Civil and Environmental Engineering  
Division of Applied Acoustics, Vibroacoustics Group  
CHALMERS UNIVERSITY OF TECHNOLOGY  
Gothenburg, Sweden 2012

**The influence of modelling parameters on the simulation of car tyre  
rolling losses and rolling noise**

CARSTEN HOEVER

© CARSTEN HOEVER, 2012.

Lic / Department of Civil and Environmental Engineering,  
Chalmers University of Technology  
Technical report no. lic 2012:11  
ISSN 1652-9146

Department of Civil and Environmental Engineering  
Division of Applied Acoustics, Vibroacoustics Group  
Chalmers University of Technology  
SE-412 96 Gothenburg  
Sweden  
Telephone: +46 (0)31-772 2200

Printed by  
Chalmers Reproservice  
Gothenburg, Sweden 2012

# The influence of modelling parameters on the simulation of car tyre rolling losses and rolling noise

CARSTEN HOEVER

Department of Civil and Environmental Engineering  
Division of Applied Acoustics, Vibroacoustics Group  
Chalmers University of Technology

## ABSTRACT

Due to legislative changes within the EU there is an increased demand for improvement in car tyre rolling resistance and noise generation. Yet, apart from empirical data based on measurements, there is little information concerning the relationship between rolling resistance and rolling noise generation. The purpose of this work is to establish a simulation framework which allows to explore the underlying physical processes connecting both areas. Special emphasis is put on the development of an accurate and efficient condensation procedure for the estimation of the necessary tyre input data from detailed design data available to the manufacturer. The method is exemplified by the derivation of the input deck for a 175/65 R14 tyre which was previously not implemented in the modelling tool.

For the simulations a waveguide finite element model of the car tyre is combined with a non-linear 3D model of the tyre/road contact to simulate the structural dynamics of a tyre rolling under steady-state conditions on a real road. Rolling resistance is calculated based on the power input into the tyre while the velocity field on the tyre surface is used to determine the radiated sound pressure based on a boundary element method approach. The applicability of the approach is shown by calculating rolling resistance and sound radiation for an initial setup of modelling parameters. In the further course of the study the influence of a variety of modelling parameters on the outcome of the rolling loss and rolling noise simulations is investigated.

A number of key parameters for the simulation of one or both of the quantities are identified. It can be shown that especially the contact stiffness and the geometry of the BEM mesh are crucial parameters for the rolling noise simulations. Some remarks on the required quality of tyre input data are made. Further results show that it is not generally possible to relate variations in input and transfer mobilities to changes of rolling resistance or rolling noise and vice versa.

**Keywords:** tyres, tyre/road noise, rolling resistance, tyre/road interaction, radiation, waveguide finite element, modelling parameters, parameter study



*I became insane, with long intervals of horrible sanity.*  
Edgar Allan Poe



# Preface

This thesis is a self-contained monograph. The work presented in it is partly based on the following two papers:

## **Paper I**

Waveguide-finite-element based parameter study of car tyre rolling losses.

C. Hoever, P. Sabiniarz, and W. Kropp.

In: Proceedings 6th Forum Acusticum, Aalborg, Denmark, 2011, pp. 789–794.

## **Paper II**

A simulation-based parameter study of car tyre rolling losses and sound generation.

C. Hoever and W. Kropp.

In: Proceedings Euronoise 2012, Prague, Czechoslovakia, 10-13 June 2012, pp. 926–931.

The content of these papers is based on a previous, different tyre than the one implemented and used in this thesis. For reasons of coherence it was therefore decided not to write this thesis as a collection of Papers I and II.



# Acknowledgements

When I came back to Sweden at the end of 2009 to start my Phd studies at Chalmers' Division of Applied Acoustics I was not sure how keen I was to work with tyre/road noise or rolling resistance. Nevertheless, I was sure that I was not making a mistake. The four months I had spend at Chalmers as an exchange student in 2008 had not only shown me that Göteborg is a nice place to live. They had foremost convinced me that Applied Acoustic is a terrific place to work. In view of this I was more than willing to take the risk and see if the tyres and I would make for a good team. As with most relationships there were some up and downs, but at the end of the day I can say that I enjoy working on such complex but also exciting topics as rolling resistance and rolling noise.

The complexity is reflected in the length of this thesis, for which I apologise. I nevertheless hope that at least a few readers will appreciate my decision to describe the most fundamental concepts for the modelling of rolling noise and rolling resistance in such a way that they can be understood without the need for too much further literature.

A work like this is never possible without the guidance, support, help, and friendship of other people. I have to thank my friends and colleagues at Applied Acoustics for the last three years, it has been a pleasure. I would especially like to thank Bart, Julia, and Patrik for their valuable comments on this thesis. "Ein großes Danke" to my supervisor, Wolfgang Kropp. I am looking forward to at least two more years of interesting (late-night) discussions.

I am grateful for the support from the NVH group at Continental Reifen Deutschland. Particular thanks to Dr. Achillefs Tsotras for never getting annoyed by my questions about tyre material properties. Thanks to Freddy Rietdijk for support with the measurements.

The funding from the BMWi project *LeiStra3* (Leiser Straßenverkehr 3) is gratefully acknowledged.

Ein großes Danke meinen Eltern, die mir eine Inspiration sind. Last but not least many thanks to Hanna. I would have not been able to finish this thesis without your support, understanding, and love.



# Contents

<b>Preface</b>	<b>v</b>
<b>Acknowledgements</b>	<b>vii</b>
<b>List of Figures</b>	<b>xv</b>
<b>List of Tables</b>	<b>xvii</b>
<b>1. Introduction</b>	<b>1</b>
1.1. Background - The environmental impact of car tyre rolling losses and sound radiation . . . . .	1
1.2. Scope of the thesis . . . . .	3
1.3. Outline . . . . .	4
<b>2. On rolling resistance and rolling noise</b>	<b>5</b>
2.1. Fundamentals of rolling resistance . . . . .	5
2.2. Fundamentals of rolling noise . . . . .	6
2.2.1. Vibrational mechanisms . . . . .	8
2.2.2. Aerodynamical mechanisms . . . . .	11
2.2.3. Propagation effects . . . . .	12
<b>3. Review of existing models</b>	<b>13</b>
3.1. Requirements for a combined rolling resistance and tyre/road noise simulation tool . . . . .	13
3.2. Review of rolling resistance models . . . . .	13
3.3. Review of tyre/road noise models . . . . .	15
3.3.1. General overview . . . . .	15
3.3.2. Tyre models . . . . .	17
3.3.3. Contact models . . . . .	20
3.3.4. Radiation models . . . . .	22
3.4. The proposed simulation tool for rolling resistance and tyre/road noise . . . . .	24
<b>4. The tyre/road noise and rolling resistance model</b>	<b>27</b>
4.1. The waveguide finite element tyre model . . . . .	27

4.1.1.	Basic WFE formulation . . . . .	27
4.1.2.	Free response, forced response and damping . . . . .	31
4.1.3.	Element formulation . . . . .	35
4.1.4.	Advantages of WFEM . . . . .	35
4.2.	The tyre/road interaction model . . . . .	36
4.2.1.	Basic contact formulation . . . . .	36
4.2.2.	Contact springs . . . . .	38
4.2.3.	Implementation details and input parameters . . . . .	39
4.3.	The half-space boundary element method radiation model . . . . .	40
4.3.1.	Governing equations . . . . .	40
4.3.2.	Numerical implementation . . . . .	42
4.3.3.	Tyre/road noise specialities . . . . .	43
4.4.	Calculating rolling resistance . . . . .	46
4.5.	Additional remarks on the simulation process . . . . .	48
4.5.1.	Temporal and spatial resolution . . . . .	48
4.5.2.	Conversion between Euler and Lagrange reference system . . . . .	48
4.5.3.	Rotational effects . . . . .	49
4.5.4.	Large-deformation non-linearity . . . . .	50
<b>5.</b>	<b>Estimation of Material Properties for the WFE tyre model</b>	<b>51</b>
5.1.	Available information . . . . .	54
5.2.	Condensation of tyre material properties for shell elements . . . . .	55
5.2.1.	Stress-strain relations for individual layers . . . . .	55
5.2.2.	Force and moment resultants for laminates . . . . .	60
5.2.3.	Transverse shear . . . . .	62
5.2.4.	Determination of the elastic stiffness matrix for a shell element . . . . .	63
5.3.	Stiffness parameters for solid elements . . . . .	64
5.4.	Pretension . . . . .	65
5.5.	Damping properties . . . . .	67
5.6.	Additional implementation considerations . . . . .	68
5.7.	Validation . . . . .	70
<b>6.</b>	<b>Simulation results</b>	<b>71</b>
6.1.	Initial tyre configuration . . . . .	71
6.1.1.	Setup . . . . .	71
6.1.2.	Rolling noise . . . . .	72
6.1.3.	Rolling resistance . . . . .	75
6.2.	Operating conditions . . . . .	78
6.2.1.	Rolling speed . . . . .	78
6.2.2.	Static load . . . . .	80
6.2.3.	Inflation pressure . . . . .	80
6.3.	Tyre properties . . . . .	82

---

6.3.1.	Temperature effects . . . . .	82
6.3.2.	Material parameters without optimisation . . . . .	85
6.3.3.	Coupling-terms in the shell element rigidity matrix . . . . .	86
6.4.	Modelling parameters . . . . .	88
6.4.1.	Centrifugal effects . . . . .	88
6.4.2.	Contact model . . . . .	90
6.4.3.	Radiation model . . . . .	94
<b>7.</b>	<b>Conclusions and future work</b>	<b>99</b>
7.1.	Conclusions . . . . .	99
7.1.1.	Condensation of material properties . . . . .	99
7.1.2.	Initial simulation results . . . . .	100
7.1.3.	Tyre temperature . . . . .	100
7.1.4.	Influence of material parameter optimisation on rolling noise and rolling resistance calculations . . . . .	101
7.1.5.	Coupling terms in the rigidity matrix . . . . .	101
7.1.6.	Centrifugal effects . . . . .	101
7.1.7.	Contact parameters . . . . .	101
7.1.8.	Radiation parameters . . . . .	102
7.2.	Future work . . . . .	102
<b>A.</b>	<b>Reference frames and coordinate systems</b>	<b>105</b>
A.1.	Reference frames . . . . .	105
A.2.	Coordinate systems . . . . .	106
<b>B.</b>	<b>Genetic algorithm</b>	<b>109</b>
<b>C.</b>	<b>Measurement of tyre mobilities</b>	<b>111</b>
C.1.	Setup . . . . .	111
C.2.	Measurement results . . . . .	112
	<b>References</b>	<b>129</b>



# List of Figures

1.1. EU label for replacement tyres. . . . .	3
2.1. Main regions of a tyre. . . . .	6
2.2. Examples for typical third-octave band rolling noise spectra. . . . .	7
2.3. Vibrational behaviour of a tyre. . . . .	9
3.1. The three parts of tyre/road noise modelling. . . . .	16
3.2. The difference between <i>apparent</i> and <i>real area of contact</i> . . . . .	20
3.3. Change of contact area during the loading phase. . . . .	21
4.1. Flowchart of the tyre/road noise and rolling resistance simulations. . . . .	28
4.2. The tyre as a curved waveguide. . . . .	29
4.3. WFEM mesh of a slick 205/55 R16 tyre. . . . .	30
4.4. Examples for three free response solutions. . . . .	32
4.5. Contact geometry between tyre and road. . . . .	36
4.6. Small-scale contact modelling using contact springs. . . . .	38
4.7. Example for a road surface profile with pronounced waviness. . . . .	39
4.8. Example for tyre/road interaction. . . . .	40
4.9. Domain definition for the exterior BEM problem. . . . .	41
4.10. The BEM tyre representation, the reflecting ground and the evaluation surface. . . . .	43
4.11. The effect of static deformation on the BEM mesh. . . . .	46
4.12. Rearranging a contact force from the Euler to the Lagrange system. . . . .	49
5.1. Tyre cross section with the most important functional parts. . . . .	52
5.2. Comparison of detailed tyre cross section and WFEM mesh. . . . .	53
5.3. The 175/65R 14T XL tyre modelled in this thesis. . . . .	54
5.4. Shell element. . . . .	55
5.5. Fibrous composite layer . . . . .	56
5.6. Definition of rotation direction between principal material axes of the fibrous composite and the curvilinear WFEM shell coordinates. . . . .	59
5.7. Laminated shell element. . . . .	60
5.8. Solid element. . . . .	65
5.9. Tyre cross section geometry for pretension calculations. . . . .	65

5.10. Pretension along the tyre cross section. . . . .	67
5.11. Loss factor data. . . . .	68
5.12. WFEM mesh of the tyre cross section. . . . .	69
6.1. The first segment of the ISO road profile. . . . .	72
6.2. sound pressure levels for the initial configuration. . . . .	73
6.3. Directivity of the radiated sound pressure. . . . .	74
6.4. Distribution of dissipation over the tyre cross section for initial configuration. . . . .	75
6.5. Rolling losses for the initial configuration as a function of frequency and circumferential wave order. . . . .	77
6.6. Dispersion relations. . . . .	78
6.7. Dependency of rolling resistance and rolling noise on the speed. . .	79
6.8. Dependency of rolling resistance and rolling noise on the static load. .	80
6.9. Third-octave band sound pressure levels for different static loads. .	81
6.10. Input mobilities for tyre configurations based on material data for 55°C. . . . .	82
6.11. Distribution of dissipation over the tyre cross section for 55°C. . .	83
6.12. Third-octave band sound pressure levels for different tyre configurations based on material data for 55°C. . . . .	84
6.13. Rolling losses and rolling noise for material parameters before optimisation. . . . .	85
6.14. Input and transfer mobilities for tyres without coupling terms. . .	86
6.15. Position of shell elements without $P_{i3}/Q_{i3}$ coupling terms. . . . .	87
6.16. Third-octave band sound pressure levels for tyre models without coupling terms. . . . .	88
6.17. Input and transfer mobilities with and without centrifugal stiffening for 110 km/h. . . . .	89
6.18. Third-octave band sound pressure levels with and without centrifugal stiffening for different speeds. . . . .	90
6.19. Third-octave band sound pressure levels for different contact stiffnesses. . . . .	91
6.20. Side view of tyre deformation due to static loading for two different contact stiffnesses. . . . .	92
6.21. Average contact force power spectra for two different contact stiffnesses. . . . .	93
6.22. Third-octave band sound pressure levels for rolling on a drum. . .	94
6.23. Tyre deformation and contact force spectrum for a tyre on a drum. .	95
6.24. Third-octave band sound pressure levels for different heights of the tyre above the road surface. . . . .	96
6.25. Third-octave band sound pressure levels for BEM mesh with and without static deformation. . . . .	97

A.1. The Euler and Lagrange reference systems for a tyre rotating at an angular speed $\Omega$ . . . . .	105
A.2. Overview of the different coordinate systems. . . . .	106
C.1. Position of measurement positions and excitation point on tyre cross section. . . . .	111
C.2. Pictures of measurement setup. . . . .	112
C.3. Translational semi-rigid body mode. . . . .	112
C.4. Measured and calculated mobilities and coherence for $0^\circ$ . . . . .	113
C.5. Measured and calculated mobilities and coherence for $45^\circ$ . . . . .	114
C.6. Measured and calculated mobilities and coherence for $90^\circ$ . . . . .	115
C.7. Measured and calculated mobilities and coherence for $135^\circ$ . . . . .	116
C.8. Measured and calculated mobilities and coherence for $180^\circ$ . . . . .	117



# List of Tables

- 6.1. Simulation results for the initial configuration. . . . . 75
- 6.2. Time and frequency resolutions for different rolling speeds. . . . . 79
- 6.3. Dependency of rolling resistance and rolling noise on the inflation pressure. . . . . 81
- 6.4. Dependency of rolling resistance on centrifugal stiffening. . . . . 89
- 6.5. Dependency of rolling resistance and rolling noise on the stiffness of the contact springs. . . . . 90
  
- C.1. Measurement equipment. . . . . 112



# 1. Introduction

## 1.1. Background - The environmental impact of car tyre rolling losses and sound radiation

Greenhouse gas emissions and exterior traffic noise are two major environmental issues associated with the road transportation sector.

In 2006 the fuel consumption in the road transportation sector was responsible for 23 % of the CO<sub>2</sub> emissions in the European Union (EU) [1] and 26 % in the United States [2]. In both cases the absolute emission values remained constant or even increased since 1990. As there is sustained demand for personal mobility and transportation services in most societies, it seems unlikely that a reduction of CO<sub>2</sub> emissions can be achieved by a reduction of mileage travelled. Instead, one possible way of reducing CO<sub>2</sub> emission is by finding ways to increase the energy efficiency of existing means of transportation.

For cars powered by classical combustion engines, only about 10 % to 40 % of the chemical energy stored in the fuel is available as mechanical energy from the engine, the remainder being consumed by engine inefficiency in form of waste heat [3]. Further reductions caused by friction in the driveline, standby operation or auxiliary appliances (e.g. the A/C system) result in even less mechanical energy being actually available at the axles to drive the wheels. The remaining energy is finally consumed by aerodynamic drag, rolling resistance and acceleration. Depending on vehicle type and driving conditions, eventually about 5 % to 30 % of the fuel consumption are due to hysteretic losses in the tyres, i.e. rolling resistance [3]. For trucks and other heavy vehicles the figures are even higher, ranging from 15 % to 40 %. Accordingly, decreasing energy losses due to rolling resistance has a strong potential of reducing a vehicle's overall fuel consumption. The Transportation Research Board of the United States, for example, has come to the conclusion that "a 10 percent reduction in average rolling resistance [...] promises a 1 to 2 percent increase in fuel economy"<sup>1</sup> [4]. Similar numbers have also been reported for the EU [5]. Additionally, Barrand and Bokar [3] have shown that lower rolling resistances not only help in bringing down greenhouse gas emissions but also reduce the release of local pollutants such as CO and NO<sub>x</sub>.

---

<sup>1</sup>This equivalent a reduction of the overall yearly fuel consumption in the USA by  $3.7 \cdot 10^9$  l to  $7.5 \cdot 10^9$  l.

For hybrid and electrically powered cars the influence of the rolling resistance on the overall energy efficiency is expected to be even higher as these vehicle classes feature a greatly improved power train efficiency when compared to vehicles with combustion engines [6]. Though the actual impact of rolling resistance reductions on CO<sub>2</sub> emissions is more difficult to assess for these alternative propulsion techniques, it is safe to assume that an increase in energy efficiency is always ecologically beneficial.

Besides being a significant source of greenhouse gas emissions, the road transportation sector places a further severe burden on a large part of the population in form of road traffic noise. A recent report by the World Health Organization (WHO) [7] estimates that within the EU about 50 % of the population are regularly exposed to A-weighted road traffic noise levels exceeding the WHO guideline value for outdoor sound levels of 55 dB, and about 10 % to A-weighted road traffic noise levels exceeding 65 dB, i.e. levels with an increased risk of suffering from cardiovascular problems. Other possible noise related health problems include cognitive impairment in children, sleep disturbance, tinnitus and annoyance. As a consequence, the WHO assumes that “at least one million healthy life years are lost every year from traffic-related noise in the western part of Europe” [7]. Although the contribution of noise originating from rail and air traffic cannot be neglected, road traffic noise comprises the main burden of this traffic-related noise [7, 8].

Road traffic noise can be separated into a vehicle’s power train noise, rolling noise and aerodynamic noise. At the most common driving speeds of 30 km/h to 100 km/h rolling noise is the dominating noise source [9], while power train noise dominates at lower and aerodynamic noise at higher speeds.

In sum, two of today’s major environmental issues originating from the road transportation sector, namely CO<sub>2</sub> emissions and traffic noise, can be related to tyres. This has been recognised by legislative policy makers, for instance resulting in a new EU-wide labelling scheme for replacement tyres [10] which includes (simplified) information about both the rolling resistance as well as the external rolling noise, see Fig. 1.1. The goal is to encourage end-users to purchase tyres which are more fuel-efficient and generate less noise.

In spite of the environmental relevance of tyre properties with regard to rolling resistance and sound radiation and the recent effort to put these in a common context, there is astonishingly few detailed information available on the relation between rolling resistance and rolling noise generation of car tyres. In particular there is a lack of knowledge regarding the question whether some of the underlying mechanisms might be the same in both areas.

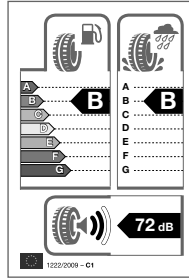


**Fig. 1.1.** EU label for replacement tyres. Source: [11].

## 1.2. Scope of the thesis

The aim of this thesis is to investigate the fundamental physical processes connecting car tyre rolling resistance and rolling noise. Of special interest is the question of how the hysteretic losses in the tyre structure are linked to the vibrational behaviour (e.g. in terms of dominant frequencies or wave types and orders). Apart from helping to design tyres with a low rolling resistance and/or rolling noise, this knowledge is invaluable for evaluating whether reductions can be achieved in both areas simultaneously or whether this is a contradictory requirement.

For this, an acoustical tyre/road interaction model aimed at calculating rolling noise is significantly extended to allow detailed calculations of rolling losses. Using a standard tyre configuration the physical connections between rolling resistance and sound generation are evaluated. In a parameter study the effect of tyre properties and external parameters (road surface, speed etc.) on dissipation and sound radiation is evaluated.

Every numerical simulation is only as good as the input data it is based on. Accordingly, special emphasis is put on the proper definition of tyre input data. A rigorous, yet efficient, scheme for deriving the necessary input data from tyre design data is presented. This facilitates the future use of the simulation package by reducing the necessary implementation effort for new tyres and allowing for more detailed design variations in parameter studies.

Modelling rolling resistance and/or rolling noise is a complex task which involves several different simulation stages. At each of these stages decisions about certain modelling parameters have to be made. The influence of some of these parameters on the simulated rolling noise and rolling resistance is evaluated.

As a final note it shall be added that, unless noted otherwise, only exterior rolling noise is covered in this study. No efforts are made to investigate the influence of tyre/road interaction on noise and/or vibrations inside the vehicle compartment.

### 1.3. Outline

The thesis is structured as follows.

In *Chapter 2* background information on rolling resistance and rolling noise is given. It is tried to identify the most important physical processes which need to be accounted for in simulations.

A literature review on existing models for rolling resistance and rolling noise calculations follows in *Chapter 3*. Special attention is paid to the question whether the existing models can be used to simulate rolling losses and rolling noise in a common context. Based on the findings, a simulation tool is proposed.

This tool is explained more in detail in *Chapter 4*. The fundamental concepts behind the waveguide finite element tyre model, the non-linear time-dependent contact model, the boundary element radiation model, and the rolling loss calculations are described. It is furthermore explained how this sub-modules interact with each other.

*Chapter 5* describes the necessary procedures to derive the tyre's material properties in the simulation tool from actual manufacturer design data. The process is exemplified for a 175/65 R14 tyre. Results are validated with respects to mobility measurements.

The outcome of the rolling loss and rolling noise simulations is presented in *Chapter 6*. Results for an initial set of modelling parameters are thoroughly analysed. To what extent the simulations are influence by variations of operating conditions or tyre, contact, and radiation parameters if investigated as well.

A summary of the work is finally given in *Chapter 7*. Some suggestions for future work are presented.

## 2. On rolling resistance and rolling noise

### 2.1. Fundamentals of rolling resistance

Traditionally, rolling resistance has been associated with a drag force  $F_R$  of unit Newton opposing the direction of motion. In ISO 18164:2005 [12], however, it is more generally defined as the mechanical energy converted into heat,  $E_{\text{loss}}$ , over a distance travelled,  $L$ , with a unit of J/m, i.e.

$$F_R = \frac{E_{\text{loss}}}{L} . \quad (2.1a)$$

For steady-state rolling at a speed of  $V$ , the rolling resistance can also be expressed in terms of the dissipated power  $P_{\text{loss}}$

$$F_R = \frac{P_{\text{diss}}}{V} . \quad (2.1b)$$

As a consequence of Equations (2.1) the term *rolling loss* can be used as an equivalent expression for *rolling resistance*. Because there is a linear dependency of the rolling resistance on the axle load  $F_z$  under normal operation conditions [13], the *rolling resistance coefficient*  $C_r$  has also become a widely used measure to express rolling losses:

$$C_r = \frac{F_R}{F_z} = \frac{P_{\text{loss}}}{F_z V} . \quad (2.2)$$

There is a slight uncertainty attached to the dependency of (2.2) on the rolling speed  $V$  as rolling losses are not in all cases linearly dependent on speed [13, 14]. In spite of this, the rolling resistance coefficient is still a quantity worthwhile to consider due to its widespread use in literature.

About 80% to 95% of rolling losses can be attributed to hysteresis. During rolling, the tyre material is periodically deformed. Due to the viscoelastic properties of the rubber compound, not all of the stored elastic energy can be regained in each cycle. Instead a part of it is dissipated. The size of this part is to some

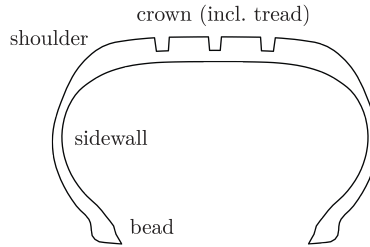


**Fig. 2.1.** Main regions of a tyre.

extent determined by external factors, because the viscoelastic properties of the rubber compound are highly temperature and frequency dependent [15].

The main cause of deformation for a rolling tyre is the flattening of the contact patch. This causes bending of the crown, the sidewalls and the bead area, compression of the tread and shearing of the tread and the sidewall [13] (cf. Fig. 2.1). This leads to a propagation of disturbances inside the tyre structure as waves in a variety of different mode shapes and orders, ultimately resulting in dissipation and also sound radiation.

For the nowadays nearly exclusively used radial tyres, most of the dissipation occurs in the crown and shoulder areas while passing the contact patch [13]. As these areas enter and leave the contact zone, they are subjected to large deformations. In combination with the high loss factor of the tread's rubber material this ultimately results in high hysteretic losses. Possible ways of reducing the rolling resistance are changing the tread geometry or rubber compound, or reducing the tread thickness. Any change, however, does not only affect rolling losses, but also other important aspects like wear, traction or noise generation. Additionally, the rolling resistance shows a more or less prominent dependence on a variety of other features such as tyre load, tyre geometry, tyre pressure, driving speed, (road) surface geometry, condition and roughness, etc. A thorough description of these effects is outside the scope of this study, detailed information can for example be found in [14, 13, 16].

## 2.2. Fundamentals of rolling noise

A rolling tyre is a complex dynamic system. The tyre/road interaction leads to time-varying changes of the tyre geometry which ultimately result in sound

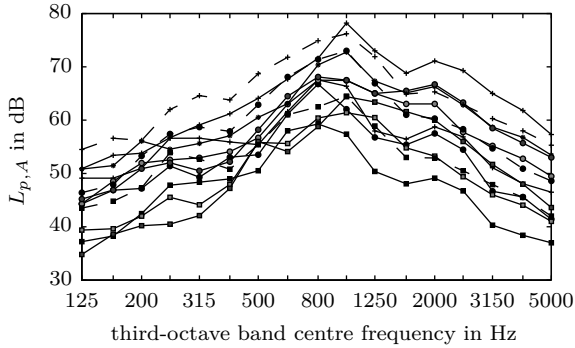


**Fig. 2.2.** Examples for typical third-octave band rolling noise spectra: coast-by measurements for a 195/65 HR15 tyre on four different road surfaces at speeds of 50 km/h (■), 80 km/h (●), and 100 km/h (+). Microphone position 7.5 m from the road axis at a height of 1.2 m.

generation. Exterior rolling noise is characterised by a very typical A-weighted<sup>1</sup> third-octave band spectrum, see Fig. 2.2 for some examples. The frequency range of interest is in the range of 100 Hz to roughly 4 kHz, with a broad but pronounced peak around 800 Hz to 1.25 kHz. This behaviour is typical for nearly all tyre/road noise spectra [18]; changes are only seen for unusual tyre/road combinations or operating conditions.

Several physical mechanisms contribute rolling noise. It is usually distinguished between

1. vibrational mechanisms, caused by
  - a) impact, or
  - b) adhesion and friction, and
2. aerodynamical mechanisms, and
3. propagation effects, such as
  - a) the horn effect, and
  - b) pipe resonances.

<sup>1</sup>In accordance with the *International System of Units* [17], the unit for A-weighted sound level spectra will not be changed to dB(A) within this work. If A-weighting is applied, it will be clearly denoted in text form or by adding the subscript  $A$  to the quantity symbol.

Items 1a and 1b lead to vibrations of the tyre tread, belt and sidewall, which in turn are radiated as sound. The processes described by item 2 are direct sources of airborne sound. The transmission of sound generated by both of these processes is affected by the mechanical, geometrical and acoustical properties of the tyre and the road surface. This effect is described by item 3.

It is believed that mainly vibrational mechanisms are responsible for low frequency rolling noise up to about 1 kHz, whereas aerodynamical mechanisms dominate above [18]. Yet, the exact contribution of each individual source mechanism is still not completely clear. Certain is only that the relevance can vary considerably depending on tyre, road surface and operating conditions.

### 2.2.1. Vibrational mechanisms

#### Impact mechanisms

Impact mechanisms could be described as macro-scale mechanical phenomena leading to tyre vibrations. They can be divided into

- running deflections,
- tread impact, and
- texture impact.

Running deflections are the large scale-deformations of the tyre tread, belt and sidewall at the leading and trailing edges of the contact zone.

Time varying contact forces due to tread patterns or road texture lead to further, mostly radial, excitation of the tread and belt area. While all mechanisms mostly excite the tyre tread and belt, there is also wave propagation to the sidewalls. Due to the high damping of the tyre material, structural vibrations are mostly limited to the proximity of the contact patch region.

Impact mechanisms are the dominating source below 1 kHz to 1.6 kHz. In addition, there is a strong indication that the aforementioned broad peak, which is typically visible in tyre/road noise spectra at around 800 Hz to 1.25 kHz, is at least partly related to macro-scale tyre vibrations [18]. Because of the importance of the vibrational behaviour of a tyre for rolling noise, the typical dynamic properties of a tyre are reviewed briefly here. For this the mobility  $Y$ , i.e. the complex ratio of velocity  $v$  and a harmonic force  $F$  in a dynamic system, is introduced

$$Y(\omega) = \frac{v(\omega)}{F(\omega)}, \quad (2.3)$$

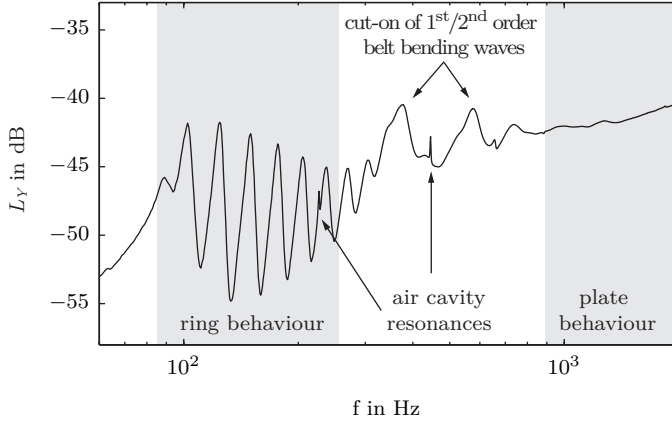


**Fig. 2.3.** Vibrational behaviour of a tyre as exemplified by a measured radial input mobility of a 205/55 R16 slick tyre for excitation at tread centre line.  $L_Y = 20 \log_{10}(|Y/Y_0|)$ ,  $Y_0 = 1 \text{ N}/(\text{ms})$ .

where  $\omega = 2\pi f$  is the angular frequency.  $Y$  is an input mobility if  $v$  is taken at the same location as  $F$ , otherwise is a transfer mobility.

In Fig. 2.3 the measured radial input mobility at tread centre line of a slick 205/55 R16 tyre is shown. In the low frequency region (below 300 Hz) the behaviour is dominated by the rigid body modes and the first circumferential modes. In this region the tyre acts like a pretensioned ring on an elastic foundation. The behaviour is mostly dominated by the inflation pressure (i.e. the pretension), the sidewall stiffness and the mass per unit length of the tyre structure. Damping is relatively low. Because of the tyre curvature, there is strong coupling between in-plane and out-of-plane motion. With increasing frequency the influence of curvature becomes weaker; after the ring frequency (where the longitudinal wavelength equals the tyre circumference) the tyre can be interpreted as a beam [19]. For typical tyres the ring frequency is located between 200 Hz and 400 Hz. The beam behaviour is often not very pronounced because of the appearance of the first cross-sectional modes which generally also occurs around 300 Hz to 400 Hz. Around their cut-on frequencies, these belt-bending modes dominate the tyre's dynamic behaviour, visible by the distinct peaks at 370 Hz and 580 Hz in Fig. 2.3. Interestingly, none of these two peaks is resulting from only one cross-sectional mode. Both are rather given by the combination of groups of modes with the same cross-sectional order (i.e. one or two) but different orders in circumferential direction. In this frequency region the tyre behaviour depends to a large extent on the bending stiffness of the belt region and to less extent the pretension.

For frequencies above some 800 Hz the tyre dynamics can no longer be attributed to individual modes or mode groups. The tyre mobility resembles that of an infinite flat plate. The most important material property is the tread's Young's modulus.

For even higher frequencies, typically above 2 kHz, in-plane shearing starts to play a role [20, 21]. In [22] it was also observed that for medium to high frequencies the local stiffness of the tread cannot be neglected. Locally, the tread rubber shows a spring-like behaviour which is influenced by the size of the excitation area.

Fig. 2.3 also shows two sharp peaks at 230 Hz and 450 Hz. These are caused by the first two circumferential resonances inside the air cavity. While especially the first of these resonances is known to be of importance for noise inside the vehicle cabin [23], they are only of minor relevance for exterior rolling noise [18].

### **Adhesion and friction mechanisms**

Micro-scale adhesion and friction mechanisms are responsible for phenomena like

- stick/slip, and
- stick/snap.

Stick/slip occurs due to tangential forces in the contact zone which are created by the change of tyre radius. These forces are resisted by frictional forces between the tread and the road surface. Friction is caused by hysteresis and adhesion, with the latter describing effects like molecular bonding, mechanical interlocking or pressure differences. When the frictional forces can no longer balance the tangential forces, the tread rubber is free to slip over the road surface, causing mostly tangential vibrations of the tread. Stick/snap occurs when the tyre/road contact is sticky (e.g. for winter tyres on warm days and/or very clean roads). During the separation process at the trailing edge, strong adhesive bonds between the tread rubber and road surface have to be overcome. When a certain number of micro-scale contact junctions have been broken, the remaining will break as well. This avalanche-like effect causes a very sudden acceleration of the tread and maybe also a transient air-flow through the opening slid.

The influence of stick/slip motion on sound generation depends on the slip velocity and the tread geometry. In general it is a rather high-frequency phenomena which is only of secondary relevance for rolling noise under steady-state rolling conditions [13]. However, it can be a significant source of noise under acceleration, braking or cornering.

### 2.2.2. Aerodynamical mechanisms

All sound generation processes which are directly related to air displacement (as opposed to being caused by vibrations) are included in this group. These processes include

- air turbulence,
- air-pumping, and
- Helmholtz resonances.

Due to the translational and rotational motion of a rolling tyre air is displaced and dragged around the spinning tyre and wheel. It is assumed that the resulting air turbulences are of relevance for overall noise levels for combinations of high speed, high frequencies and low-noise road surfaces [18].

A phenomenon of great importance is air-pumping. The physical processes behind it have not yet been fully understood. A common theory describes it as the displacement of air in and out of all sorts of cavities formed by the tread and the road surface during contact[18]. At the leading edge air is compressed and forced away from the contact while at the trailing edge air expands and is drawn back into the cavities. Further air displacements occur within the contact patch itself. Air-pumping might also be caused by the displacement of tread rubber by road roughness peaks. The volume of displaced rubber is larger than the volume of the peak, thus causing air displacement [24]. Regardless of which theory is applied, high air pressure gradients make air-pumping a significant if not the main noise source for frequencies above approximately 1 kHz. The rate of air displacement is mainly dependent on the rolling speed; the radiated sound power is assumed to be proportional to the fourth power of vehicle velocity [19].

Helmholtz resonances may be seen as special cases of air-pumping. A Helmholtz resonator is a mass-spring system which is formed by the motion of air in a cavity. When a tread cavity moves out of contact, a mass-spring system is created in the moment the cavity opens again. The air inside the cavity acts as a spring and the air in the just created small channel as a mass. The frequency and amplitude of this resonator change continuously as the cavity moves further out of contact, resulting in a tone burst. In [25] it is shown that this effect has a significant effect on sound radiation for cross-bar type tyres in the 1 kHz to 2.5 kHz range.

The tyre cavity resonances which have been briefly mentioned in Sec. 2.2.1 constitute another example of aerodynamical sources.

### 2.2.3. Propagation effects

#### The horn effect

Close to the contact region, the geometry between tyre and road resembles that of a horn. The exponentially widening geometry when moving away from the contact patch provides a gradual and smooth impedance match between the narrow throat at the contact edge and the ambient air. This has a significant amplification effect on sound radiation because a majority of the rolling noise sources are situated at or near the contact patch. The amplification affects the whole frequency range from roughly 300 Hz and upwards. The maximum lies between 1 kHz and 3 kHz, where amplifications of up to 25 dB in the tyre plane have been reported. At high frequencies interference becomes important and complex directivity patterns form [26, 27]. Even for complex pass-by situations, in which distance and angle to the tyre vary continuously and the car body affects the sound propagation, average amplifications of 5 dB to 12 dB per third-octave band have been reported [26]. The horn effect is strongly affected by tyre width and road surface, with smaller tyres and higher surface porosity reducing the amplification effect [26, 27].

#### Pipe resonances

Pipe resonances occur when standing waves are excited inside the grooves of the tyre tread by nearby vibrational or aerodynamic sound sources. This amplifies the sound created by the source. The resonance frequency depends on the length the pipe and whether it is open at one of two of the ends. Systems of pipe resonators are formed for every tread pattern in contact with a smooth road surface. The effect on sound radiation depends to a great amount on the individual, hard to determine geometrical properties during contact, and is not speed dependent. In an idealised test case pipe resonances have shown to increase the total A-rated sound pressure level by 3.5 dB(A) [28]. Pipe resonances are also sometimes classified as a source mechanism, often seeing them as a special case of air-pumping.

## **3. Review of existing models**

### **3.1. Requirements for a combined rolling resistance and tyre/road noise simulation tool**

Despite the growing public awareness of the environmental and health benefits associated with reductions of rolling losses and rolling noise generation of car tyres, the actual physical processes responsible for both rolling resistance and rolling noise are not yet fully understood. In particular there is a lack of knowledge regarding the question whether some of the underlying mechanisms might be the same in both areas. Of special interest is the question of how the hysteretic losses in the tyre structure are linked to the vibrational behaviour, e.g. in terms of dominant frequencies or wave types and orders. Besides facilitating the reduction of rolling resistance and/or rolling noise, knowledge in this field is invaluable for evaluating whether reductions can be achieved in both areas simultaneously or whether this is a contradictory requirement. Extensive experimental data obtained by several authors [29, 30, 31] suggests that there is no incompatibility between simultaneous noise and rolling resistance improvements. However, because of the empirical nature of the results, not much insight into the physical processes has yet been obtained. More recently, Boere et al. [32] investigated the influence of different road textures on rolling noise and rolling resistance. However, with the main focus being on the impact of the tyre/road interaction, there was no examination of the physical processes in the tyre. While several authors [33, 34, 35] used models capable of capturing the tyre dynamics for rolling resistance calculations, none of them included sound radiation.

In the next two sections, existing rolling resistance and tyre/road noise models are evaluated regarding their suitability for combined simulations of both quantities in a common context. The model proposed in this study is finally described in Sec. 3.4.

### **3.2. Review of rolling resistance models**

Numerous examples for calculations of rolling resistance are available in the literature (see [4] for an overview). Besides some approaches partly based on measured data [36, 37], most of them follow the same conceptual approach of using a steady-

state rolling tyre model to calculate rolling resistance either as a drag force or based on energy dissipation.

Stutts and Soedel [38] used a stationary tension band on an elastic foundation to model the tyre and calculated the rolling resistance from the deflection in the contact zone. In [39] instead a model of an elastic ring supported by a viscoelastic foundation is used to calculate the hysteretic energy dissipation. Miège and Popov [40] compared several analytical methods for computing rolling resistance, including a flexible ring model. All of the mentioned models are quite similar to the shell and ring models often used for acoustical tyre modelling. They either already allow for the calculation of tyre vibrations (cf. [40] where frequency response functions up to 200 Hz are calculated) or could be extended to do so. Geometrically, however, the used tyre models are over-simplified, limiting the usable frequency range and preventing the calculation of the dissipation distribution over the tyre cross-section.

Another commonly used approach is based on finite element modelling (FEM) of the tyre, often combining mechanical and thermal models. Typically, an elastic model of the tyre is used to calculate the strain cycles for free rolling. An viscoelastic simulation then gives the heat generation rate as input for a thermal simulation. This process is repeated until the thermal state has converged. Rolling resistance is then calculated in terms of the hysteresis per cycle. The thermal FE model allows identification of the relative contributions of different tyre parts to the overall rolling loss. Models following this approach have for example been proposed by Park et al. [41], Hall and Moreland [14], Rao et al. [42], and Lin and Hwang [43], with the latter only calculating the temperature distribution but not the rolling resistance. A slightly different approach was used by Ghosh et al. [44], who calculated the dissipated energy directly out of the strain energy density distribution in a steady-state rolling FE model. An expression involving the ratio of dissipated energy to input energy over one cycle was then used to calculate the rolling resistance. Another method which directly computes the energy loss during the mechanical FEM process was introduced as the *directional incremental hysteretic model* in [45]. Again, rolling resistance was determined as hysteretic loss per cycle.

The advantage of methods based on FEM is that it is usually possible to use commercial software, thus reducing the implementation effort. The models are also rather geometrically detailed, allowing the extraction of information on the distribution of dissipation inside the tyre. It is furthermore conceivable that most of the mentioned FE models, with the exception of the *directional incremental hysteretic model* [45], could be extended to allow calculations of tyre vibrations. However, resolution requirements on the FE mesh would most probably be too high to allow for models of acceptable numerical complexity.

A general problem with all mentioned methods is the contact implementation. The used tyre/road interaction models are limited to the large scale deformations

caused by static loading of a tyre rolling under steady-state conditions on a smooth road. The small scale variations of road roughness and the complex interrelation between tyre deformation and contact forces which are both essential for the correct modelling of tyre vibrations are not included. Recently, a two-step process was proposed by Boere et al. [32] to overcome this limitation. It superposes a dynamic, local tread/road interaction on the large scale deformations obtained from FEM. Rolling resistance was calculated by means of input power into the system and results for different road surfaces were compared to rolling noise measurements for the same surfaces. However, with the main focus being on the impact of the road surface on rolling resistance and rolling noise, there was no examination of the physical processes in the tyre.

Bschorr and Wolf [33] seem to be the first to have used a model of the tyre's structural dynamics to draw conclusions about the rolling resistance. However, their rolling resistance estimation was not very detailed as it was merely a by-product of their study on tyre vibrations.

A substantial contribution was made by Fraggstedt [35]. He used a waveguide finite element model (WFEM) to calculate the vibrations and rolling losses of a rolling tyre. Frequency and wave order distributions were shown as well as individual element contributions to the overall dissipation. However, the deviations between simulated and measured rolling resistances were slightly higher than for some of the other mentioned methods. Furthermore, a detailed analysis of the results was missing and it was never investigated how changes in tyre parameters affected the dissipation. As radiation was not included in the model, rolling noise could not be calculated.

## 3.3. Review of tyre/road noise models

### 3.3.1. General overview

Methods for tyre/road noise simulations can generally be divided in three main categories:

1. Statistical models,
2. physical models, and
3. hybrid models.

The statistical models try to establish relations between different sets of measured data, e.g. measured road surface profiles and measured sound pressure levels [46, 47]. The mechanical processes in the tyre are of no interest; they are neither simulated nor are any efforts made to understand them. Consequently, statistical models are not a suitable choice within the scope of this study.

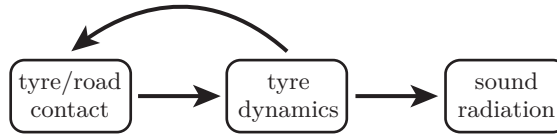


**Fig. 3.1.** The three parts of tyre/road noise modelling.

Physical models, in contrast, try to simulate the actual physical processes responsible for tyre vibration and sound radiation using basic physical laws. The models often either follow an analytical approach in which the tyre is replaced by a simplified structure (like a ring or plate), or they are based on numerical tools like FEM or boundary element modelling (BEM). Measured data is only used for validation purposes.

Hybrid models combine features of statistical and physical models. A typical example would be a statistical model which no longer directly relies on measured road surface profiles because of the non-linearity of the tyre/road interaction. Instead, contact forces calculated by a physical contact model are used as input into the statistical part. This approach is for example used by the SPERoN model [48]. Hybrid models share most of the limitations of statistical models with regards to the obtained physical insight. Because of the limitations of statistical and hybrid models, the focus will be purely on physical models in the following<sup>1</sup>.

Tyre/road noise modelling is typically seen as three-part process as shown in Fig. 3.1. The core is a model of the tyre dynamics which allows for free or forced response calculations. To simulate the excitation of the tyre by the road surface, a tyre/road contact module is needed. Because of the interdependency of contact forces and tyre vibrations — the forces cause vibrations, yet at the same time the vibrations influence the forces — there is usually a two-way coupling between the tyre/road contact module and the tyre dynamics module. While these two modules are sufficient to estimate for example hub forces or rolling resistance, an additional module is needed to calculate the actual sound radiation, i.e. the tyre/road noise, caused by the tyre vibrations. Variations or extensions of this three-stage process are obviously conceivable, e.g. to include air pumping or for interior noise calculations.

As the complexity of each of the three mentioned sub-modules is rather high, very few models exist which are actually able to calculate tyre/road noise. Many models only focus on the tyre dynamics (with or without road contact), and omit sound radiation. For many applications this is sufficient, and if needed, most of these models could be extended by a radiation module. Accordingly, the following

<sup>1</sup>The interested reader can find more information about statistical and hybrid models in [9, 49]

review will start with a general selection of tyre models found in the open scientific literature which is not limited to include only complete tyre/road noise models. Contact and radiation models are then described in the subsequent sections.

### 3.3.2. Tyre models

Since the mid-1960s, a variety of different analytical models for simulating the dynamic response of tyres have been developed. These range from analytical models, based on more or less coarse simplifications of the geometrical and material properties, to highly sophisticated numerical models, accounting for the detailed physical properties of tyres.

One of the first models was presented by Böhm [50]. He calculated low frequency free and forced responses of a tyre by modelling the tyre as a pretensioned, circular ring (the belt) on an elastic foundation (the sidewall). Through the years, many variations of the same basic approach have been used to model various aspects of tyre dynamics, e.g. by Heckl [19], Kung et al. [51], Kropp [52], or more recently Kindt et al. [53] or Tsotras [54]. The models usually perform quite well for frequencies below roughly 300 Hz or 400 Hz but generally fail for higher frequencies at which wave propagation across the tyre cross section starts. This is because the approach do not allow for lateral wave propagation.

Kropp [55] proposed a method to overcome this shortcoming by modelling the complete assembly of belt and sidewalls as an pretensioned, orthotropic plate on an elastic foundation. Agreement between modelled and measured input mobilities was generally quite good for frequencies up to 2 kHz, with the exception of the lower frequency regions below the ring frequency which were negatively affected by the negligence of curvature. By combining the orthotropic plate model with a two-dimensional multipole based radiation model and a non-linear contact model in which the tread was modelled by massless uncoupled springs, tyre/road noise could be calculated as well. Agreement to measurements was good below 1.5 kHz. In [56, Paper C] the same tyre model was combined with a BEM radiation approach to investigate differences between full 3D and quasi-3D contact models. Later variations of the orthotropic plate model included incorporating curvature to increase low-frequency performance [57], modelling the sidewalls as separate orthotropic plates being perpendicularly attached to the belt plate [58], or using a two-layer setup of isotropic plates in order to investigate the influence of the tread layer on wave propagation and forced responses in normal and tangential direction [21]. O'Boy and Dowling [59] modelled tyre/road noise for a patterned tyre rolling over a rough road using a bending plate model in conjunction with a contact model similar to Kropp's and a modified Rayleigh integral approach for radiation.

Another variant of the plate approach was proposed by Pinnington [20, 60]. He modelled the tyre as a combination of a flattened, tensioned Timoshenko beam for

the belt and line impedances for the sidewalls, however with mixed results. He later extended the model by implementing belt and sidewalls as coupled, curved and tensioned Mindlin plates [61, 62]. With the exception of the cut-on frequencies of the higher-order cross-belt modes good agreement between modelled and measured mobilities was achieved for frequencies below roughly 3 kHz. An additional model which explicitly includes the sidewalls is the one by Lecomte et al. [63]. They combined an orthotropic cylindrical shell for the belt with membrane sidewalls in order to simulate the tyre behaviour in the low frequency region up to about 500 Hz.

The presented analytical models are usually comparably simple and fast, and often provide worthwhile insight into physical processes. However, problems arise due to the geometrical simplifications inherent to all of the models. This includes problems with capturing the dynamic behaviour adequately over the whole frequency range of interest for tyre/road noise, the lack of the possibility to determine localised effects, and the need for usually rather involved procedures to determine the needed simplified material properties. The ring models are also not very well suited for proper contact modelling because lateral effects cannot be included.

The rapid development of computer capacity during recent decades has made it possible to perform detailed numerical modelling of tyres using FEM. While early FE models [51, 64, 65] were geometrically only slightly more complex than their analytical counterparts, current implementations are detailed enough to individually model nearly every different material group in the tyre [66, 67]. FE based tyre dynamics models have been the basis for a number of different applications. Kung et al. [51] determined natural frequencies and mode shapes and then used these to calculate the dynamic response at the wheel axle. Richards [66] presented an FEM method which allowed for structural-acoustic coupling between the tyre structure and the air cavity. This method was used to determine the influence of the air cavity resonances on tyre vibrations and force transmissibility through the hub. Force transmissibility, along with point mobility, was also simulated using FEM by Pietrzyk [68]. The response of tyres rolling on a smooth surface were modelled by Fadavi et al. [69] and Lopez et al. [70], who also included rotational effects. The latter model was subsequently also used for rolling resistance predictions [32, 71].

A very extensive FEM approach for rolling car and truck tyres was developed by Brinkmeier et al. [67, 72]. The model is geometrically very detailed, usable for frequencies well above 1 kHz and included material non-linearity, rotational effects, ground contact and excitation by the road texture. For tyre/road noise calculations the structural model was used as input to a finite/infinite element model [72, 73]. Alas, sound radiation was considerably overestimated for rolling tyres at frequencies above 150 Hz to 200 Hz [73], probably due to shortcomings of the contact model, see Sec. 3.3.3.

Generally, FE models have proven to be valuable tools. They are flexible and can easily account for non-linearities, complex materials and geometries. Using FE,

objects and processes which are far too complicated to be covered by analytical models can be easily simulated. The use of commercial FEM software can reduce implementation time and the widespread use in industry facilitates data exchange. However, there are still two major problems associated with FEM. Firstly, finite element calculations often provide less insight into the physical processes leading to a result than a comparable analytic model (assuming that this exists). Secondly, requirements on computer capacity are high. The available computation power limits the discretisation size which in turn determines the upper frequency limit of the simulations. Due to this, simulations are usually restricted to frequencies below approximately 500 Hz. In the model of Brinkmeier et al. the frequency range was extended to above 1.5 kHz, but this required a mesh consisting of over 60 000 elements [67]. Even with today's computational resources it seems hardly practical to use FEM for parameter studies covering the whole relevant frequency region for tyre/road noise, i.e. up to around 2 kHz. The practical limits on mesh size also affect contact modelling. To accurately capture three-dimensional road surface and tyre profile variations a high resolution is necessary.

In order to reduce computational costs several approaches which combine parts of traditional FE modelling with analytical methods have been presented in recent years. Finnveden and co-workers developed a model called waveguide finite element method (WFEM) [35, 74, 75]. In this technique the tyre is considered to have constant cross sectional material and geometrical properties along the circumference. This allows to combine FE modelling of the cross-section with a wave propagation ansatz in the circumferential direction. The resulting eigenvalue problem is formulated in the wave domain and requires specially development elements. Computational costs remain low because only the cross section of the tyre needs to be modelled numerically. This considerably extends the usable frequency range; transfer functions were calculated up to 1.6 kHz [74]. The method was first used for tyre modelling by Nilsson [74], who considered the structural as well as fluid domain, using waveguide finite elements of the thin shell type, fluid type and fluid–structure coupling type. Calculated transfer functions showed mostly good agreement with measurements up to 1.6 kHz. Thick curved shell and solid waveguide finite elements were developed in [75] and used to model the free and forced response as well as the rolling resistance of a car tyre in [35], low frequency interior and exterior tyre/road noise [76], dispersion and wave phenomena [77], hub forces [78], and tyre/road noise [79].

Waki et al. [80] presented a similar approach in which the tyre is considered as a periodic structure along the circumference. Initially, a short section of the waveguide is modelled using standard commercial FEM. A periodicity condition is then applied. This results in an eigenvalue problem from which the forced response can be calculated using a wave approach. Numerical efficiency is again high and in contrast to the WFEM approach there is no need for specially designed elements. Simulations of input mobility showed good agreement to measurements up to

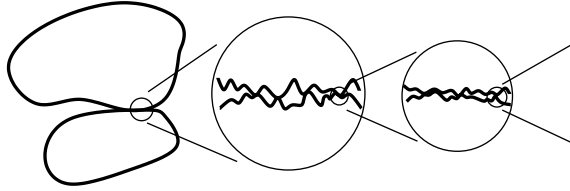


**Fig. 3.2.** The difference between *apparent* and *real area of contact*. Due to small-scale surface roughness only discrete parts of the bodies are in contact.

2 kHz. Alas, no results were shown for other quantities, e.g. transfer mobilities. The method also seems to be prone to numerical problems [81]. A variation of this approach which directly solves for the forced response has recently been presented by Duhamel et al. [82].

### 3.3.3. Contact models

In the following section only models implemented for rolling contact will be described; this leaves aside a variety of tyre/road interaction models focusing on the calculation of texture induced pressure distributions [83] or tread viscoelasticity and inertia [84, 85, 86].

Modelling the interaction between a rolling tyre and road is a complex task. One of the main challenges is the extent of relevant length scales, ranging from several meters (road waviness) down to microscopic (road asperities) or even molecular levels (adhesion effects). The size of a typical contact patch is too big to allow for a full discretisation down to the smallest relevant length scales. As a consequence, the distinction between the *apparent* and the *real area of contact* between tyre and road becomes important. At small scales, both road and tyre have a certain roughness; contact will only be made between certain parts of the asperities, see Fig. 3.2. Hence, the area which is in contact is only a fraction the size of what it appears to be at a macro-scale level. Additionally, as shown in Fig. 3.3, the contact area changes during loading and unloading. For example, at an early stage of contact only the highest peaks of the asperities are in contact, giving a very small area of contact. At a later stage, larger parts of the asperities are in contact. Thus, the real area of contact — and with it the contact stiffness — changes during the time of the contact.

On a larger length scale another aspect has to be taken into consideration: the tyre is an elastic continuum where the deformation due to a point force at location A will not be limited to just that point. A certain area of the material



**Fig. 3.3.** Change of contact area during the loading phase. At time  $t_1$  only the asperity peaks are in contact. At time  $t_2 > t_1$  the bodies are closer and the area in contact increases. This causes the contact stiffness to increase as well.

will be effected, perhaps considerably changing the conditions at another contact point B. Due to inertia, this effect does not happen instantaneously, meaning that past contact forces and deformations influence the contact conditions at the current time. This dynamic interaction can put some constraints on the achievable resolution for the contact area. Tyre models require a much lower spatial resolution to simulate the dynamic behaviour than what is needed to accurately capture the complex contact processes. Because of the computational costs and the fact that the finer resolution would only be needed in a very small part of the tyre, increasing resolution is typically not an option. Many simpler tyre models do also not explicitly include the tread, in these cases a separate contact law is required to describe the local interaction between road asperities and tread rubber.

Depending on the contact conditions, effects such as friction, adhesion and the tread rubber's viscoelasticity can also become important. Additionally, the frequency, temperature, and strain dependency of the tread's material properties might affect the contact behaviour as well.

The dynamic part of many models for rolling tyre/road contact is based on an approach which was originally used to model bow/string interaction [87]. It is a time-domain formulation in which the dynamics of the contacting bodies are described by their Green's functions. These are convolved with the contact forces to give the response at a specific time due to present and past contact forces. As the contact problem is iteratively solved for each time step, non-linear effects such as the change of contact area during contact can be included. The approach requires the bodies to be linear time-invariant systems (LTI), which puts some constraints on the tyre model. Kropp [55, 88] was the first to apply this technique to tyre/road interaction. His model was two-dimensional (i.e. based on one roughness profile line) and considered normal forces only. The tread was represented by a Winkler bedding, i.e. a set of uncoupled, massless springs with constant stiffness. Larsson et al. [89] presented a three-dimensional version of this model. The coupling of the tread displacement, which is neglected by the Winkler bedding, was accounted for by a tyre model which included a tread layer. The contact law could then be obtained from the first value of the tyre's Green's function. Wullens [56] modelled the tread as an elastic half-space. He also showed that two-dimensional roughness data is not sufficient for accurate calculation of rolling noise spectra, instead lateral

variations of tyre and road geometry have to be considered [90]. All these models neglect the microscopic change of contact area during contact. Additionally, the determination of correct stiffnesses for the Winkler bedding or the elastic-half-space is not straightforward. To account for the change in contact area, non-linear contact springs between each matching point of tyre and road were introduced by Andersson and Kropp [91]; they also described a method for obtaining stiffness functions from measured road roughness data. Sabiniaz [78] included tangential forces in the model, but used only linear contact springs. Andersson's model was also used by Boere et al. [32], who added an additional spring/damper set to each contact point to model tread blocks. Further implementations of the convolution approach were also presented by Hamet and Klein [92], Graf [93], O'Boy and Dowling [59], Liu et al. [94].

FEM approaches have also been widely used to simulate tyre/road interaction. Fadavi et al. [69] calculated the forced response of rolling tyre in contact with a flat rigid ground. Lopez Arteaga [95] did the same to obtain Green's functions for a loaded, rolling tyre. Brinkmeier et al. [72] used harmonic excitation functions based on road surface data for the contact formulation in their FEM simulations of a rolling tyre. Sound radiation could be correctly calculated for shaker excitation of the tyre, however not for real tyre/road contact [73]. This might be due to the linear nature of the contact implementation and/or a too coarse contact resolution due to FEM mesh. To overcome some of the spatial resolution limitation in FE modelling, Lopez [71] proposed an approach in which the tyre/road interaction is split up into two parts: the large scale tyre deformations are obtained from an FE model of a tyre rolling on a smooth road, while the tread/road surface interaction is calculated separately using the convolution technique. The technique seems to work quite well for the determination of rolling losses, it is however not clear if the individual calculation and subsequent superposition of large- and small-scale contact effects adequately captures the complex contact dynamics.

Finally, the modelling of tyre/road interaction under rolling conditions is not limited to sound and vibration applications. Numerous studies deal with tyre/road contact modelling as means for investigating rolling resistance, traction, contact forces under transient conditions, or vehicle dynamics simulations [39, 40, 54, 96]. However, small-scale roughness phenomena and/or tyre dynamics are often neglected in the employed Winkler-bedding type based contact models. While these simplifications are justifiable within the scope of the respective applications, the models cannot be used to accurately model tyre vibration and rolling noise.

### 3.3.4. Radiation models

The number of radiation models for tyre/road noise described in open literature is quite small. This does not come as a surprise as the calculation of sound radiation is the last step in a tyre/road noise simulation; reliable contact and tyre models

have to be established before radiation can be calculated.

One of the earliest examples of radiation calculations for vibrating tyres is the model of Keltie [97]. He modelled a truck tyre as an infinite circular cylindrical shell with a prescribed velocity field, for which sound radiation could be calculated analytically. Because of the infinite width of the tyre and the omission of the road influence, propagation effects as described in Sec. 2.2.3 could not be modelled. A model which accounts for these effects was presented by Kropp [88]. He modelled the combined contribution from the tyre and the reflection at the road surface using a two-dimensional equivalent source approach: the sound field was reconstructed using two multipoles, one for the tyre and a mirrored one for the reflections from the rigid road surface. A correction factor was derived to account for the influence of the finite tyre width. The model was used to calculate the sound radiation of a slick tyre rolling on a drum [55], and the horn effect and the radiation efficiency of different tyre modes [26]. The equivalent sources approach was extended by Bécot [98] to account for ground impedance effects.

Using a Rayleigh integral approach, three-dimensional rolling noise radiation was calculated by Graf [93] and O'Boy and Dowling [59]. The horn effect was included by means of a source specific amplification function which was obtained from separate BEM simulations.

In order to avoid the limitations analytical methods have with the modelling of the complex tyre/road geometry, numerical methods such as BEM have also been used to solve the tyre radiation problem. Ni et al. [99] modelled the noise radiation from the tyre/wheel assembly. Because of numerical constraints they did not include the road in the model and were limited to frequencies up to 350 Hz (which was sufficient for their investigations of interior noise). Due to the necessary discretisation size and the fully populated system matrices, BEM simulations are computationally costly. To reduce the numerical effort, attempts have been made to simulate the ground reflections without the need for discretising it. Brick [100] was the first to use a half-space BEM approach for tyres. This is an efficient BEM implementation which includes the ground reflections in the propagation Green's functions. In Brick's implementation arbitrary ground impedances could also be modelled. The model was used to investigate the horn effect [100], and the contribution of the individual tyre modes to the overall sound radiation of a rolling tyre [79]. Recently, Graham [101] combined the mirror source approach with BEM to investigate the horn effect.

FEM is another numerical alternative for radiation calculations. In FEM the whole domain needs to be discretised which means that discretisation costs are typically higher than for BEM, where only the surfaces of sources or other objects interacting with the wave field to be discretised. This is at least partially offset by the fact that the FEM system matrices are banded, which makes the numerical solving much more efficient. An FEM approach was used by Biermann et al. [73] to calculate the sound radiation from a tyre rolling on a drum. As traditional FEM

formulations cannot model domain boundaries with free field radiation conditions, special infinite elements were developed by Biermann et al. Alas, numerical costs were never compared to those of traditional BEM simulation, so it remains unclear which of the two methods has lower computational costs.

For sufficiently large problems, the efficiency of BEM can be improved using the fast multipole method in which a tree-like sub-structuring allows parts of the radiation problem to be solved locally [102]. Frequency- and time-domain formulations of fast multipole boundary element methods for tyre/road noise simulations are currently under development [103, 104].

For more specific radiation problems further techniques have been proposed. In order to model air-pumping effects, Wullens [56] used his elastic half-space tyre/road interaction model to calculate the air volume variation in the contact asperities. The volume flow was then assigned to monopoles situated at the leading and trailing edges of the contact patch. The validity of the approach remains unclear as no detailed results were presented. In a very simplified model for interior cabin noise calculations, Rustighi et al. [76] used radiation impedance matrices obtained from BEM to model tyre radiation. Finally, Kuo et al. [105] investigated asymptotic methods for simulating the horn effect. For low frequencies below 300 Hz a compact body scattering model was proposed. Above 3000 Hz good results were achieved using ray theory.

### **3.4. The proposed simulation tool for rolling resistance and tyre/road noise**

In Sec. 3.1 it was stated that it might be easier to enhance a tyre/road noise model to allow for calculations of rolling losses than vice-versa. The review of existing rolling loss and rolling noise models in Sections 3.2 and 3.3 has verified this. Contact and tyre dynamics implementations used in the modelling of rolling resistance are too simplified to be used for tyre/road noise calculations. In contrast, it has been shown that models capable of capturing the dynamics of a tyre rolling on a real road can be extended to give reasonable estimates of rolling losses [33, 106, 32]. In view of this, an existing, validated tyre/road noise simulation tool [79] is enhanced with a module for rolling loss calculations.

Core of the simulation package is a WFE model of the tyre [77]. Previous studies using this model have been based on a slick 205/55 R16 tyre. In this work a 175/65 R14 tyre with tread pattern is implemented instead. Tyre properties are based on detailed tyre design data provided by the manufacturer. For the estimation of the equivalent material properties needed for the model, a thorough physical condensation procedure is proposed. The previous model of the 205/55 R16 tyre does not include stiffness terms for coupling between in-plane strain and shear,

bending and twist of curvature, and coupling between normal forces and bending curvatures. This is due to lack of adequate input data. With the new condensation procedure these terms can be determined as well, meaning that the complete anisotropic behaviour of the tyre structure can be captured.

Tyre/road interaction is modelled using non-linear, convolution based algorithm. As the tread is already included in the WFE tyre model, there is no need for separate substitute structures like a Winkler-bedding or an elastic half-space. Contact springs are used to account for the small-scale contact stiffness. In contrast to the model described in [91], only linear contact springs are used because the available road roughness data is not sufficient to determine non-linear stiffnesses. Originally also included tangential contact forces (cf. [77]) have been omitted because of their minor relevance for both rolling resistance and rolling noise under steady-state rolling conditions [39, 18].

Sound radiation is calculated using the half-space boundary element method proposed by Brick [100]. Contrary to simpler analytical approaches, this model can adequately handle the complex three-dimensional geometry formed by the tyre and the road. It has been validated for both the horn effect [100], and the sound radiation of a tyre rolling on a drum [79]. The half-space approach considerably reduces the calculation effort and even though only rigid road surfaces are considered in this study, it allows ground impedance effects to be modelled in future studies.

Finally, rolling losses are calculated based on two different formulations proposed in [106]. Based on contact forces and displacements, the input power into the tyre can be calculated. For steady-state rolling this is equal to the dissipated power. Tyre road/noise is traditionally analysed as frequency spectra. Moreover the contributions of individual modes to the radiation can be analysed. Based on the waveguide properties of the tyre model, the same is now possible for the rolling losses. Frequency and/or circumferential wave order contributions can easily be identified. This way, rolling resistance and rolling noise can be analysed in the same context, which helps to identify both common and distinctive features. In the second formulation, rolling resistance is calculated by means of the internal dissipation inside the tyre. As the tyre cross-section is represented by individual elements in the WFE approach, it is possible to identify the cross-sectional distribution of losses by calculating the dissipation inside the individual elements. The ability to simultaneously extract detailed information about frequency, wave order and cross-sectional distribution of rolling losses is unique to the WFEM approach; with analytical or FE models concessions have to be made in at least one of these fields.

A more detailed description of the combined simulation tool for rolling resistance and tyre/road noise follows in Cha. 4. The necessary measures for implementing the new 175/65 R14 tyre are then presented in Cha. 5.



## 4. The tyre/road noise and rolling resistance model

In this chapter a condensed description of the simulation tool for rolling resistance and tyre/road noise which was proposed in Sec. 3.4 is given. An overview of the simulation workflow is shown in Fig. 4.1. Each of the three main modules (tyre/road interaction, tyre model, radiation) is of high complexity. Within the scope of this work it is not possible to describe each of the three in every detail. Instead, it is tried to convey those principles fundamental for the understanding of the simulation process as whole. Literature sources with more detailed information will be referenced when necessary.

Because the model of the tyre dynamics is the core part of the simulation tool, it will be described first in Sec. 4.1. This is followed by the tyre/road interaction model in Sec. 4.2, and the radiation model in Sec. 4.3. The two ways to calculate rolling losses are described in Sec. 4.4. The chapter finally concludes with Sec. 4.5, where some additional remarks on the simulation process are made.

### 4.1. The waveguide finite element tyre model

#### 4.1.1. Basic WFE formulation

The used waveguide finite element approach is identical to the one described in [77, 79]. It is a modified version of the model presented in of [35, Paper B], the main differences being the omission of the rim from the assembly and changes in the damping implementation. In the following an overview of WFEM is provided.

A waveguide is a system with constant geometrical and material properties along one (typically “long”) dimension. In this dimension, the motion can be described by a set of propagating waves fulfilling the boundary conditions imposed by the waveguide characteristics. In this sense, and with reference to Fig. 4.2, a tyre is a waveguide for which the motion along the circumferential dimension can be described by waves fulfilling a periodicity condition  $\mathbf{u}(\theta) = \mathbf{u}(\theta \pm 2\pi)$ , where  $\mathbf{u}$  is the tyre displacement and  $\theta$  the circumferential angle. Typical other waveguide examples include beams and plates [107], or rails [108, 109].

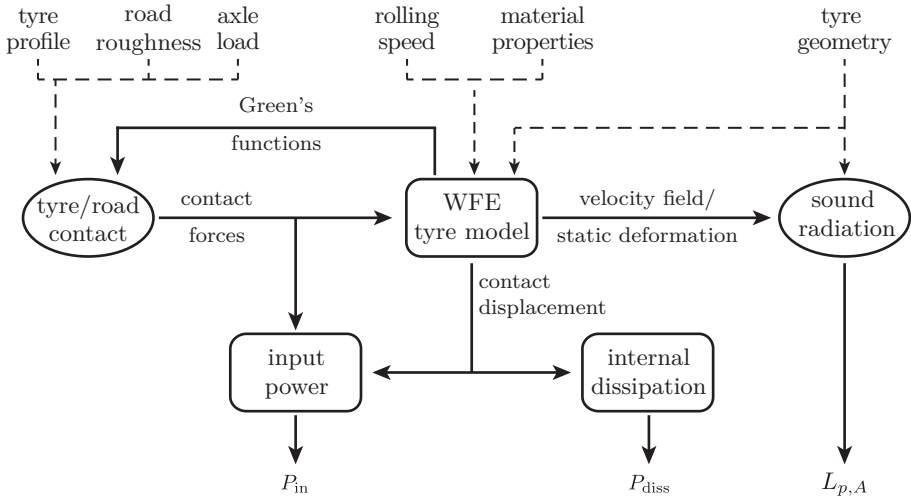


**Fig. 4.1.** Flowchart of the tyre/road noise and rolling resistance simulations. Dashed lines denote input parameters and solid lines denote calculated properties. Modules in rectangular boxes are using a Lagrangian reference frame and modules in elliptic boxes an Eulerian reference frame (cf. Appendix A.1). Output parameters are the input power  $P_{in}$ , the internally dissipated power  $P_{diss}$ , and the A-weighted sound pressure level  $L_{p,A}$ .

In WFEM, the waveguide property is used in conjunction with conventional two-dimensional finite element modelling of the waveguide cross-section, see Fig. 4.3. For a cylindrical coordinate system the components of the displacement vector  $\mathbf{u} = [u_r u_x u_\theta]^T$  at a point  $(r, x, \theta)$  are accordingly given by

$$u_i(r, x, \theta, t) = \mathbf{N}(r, x) \mathbf{v}_i(\theta, t) \quad i = r, x, \theta. \quad (4.1)$$

Herein,  $\mathbf{N}$  is a vector of cross-sectional FE shape functions while  $\mathbf{v}_i$  represents the corresponding nodal degrees of freedom vector. Thus, only the displacements' dependence on the cross-sectional coordinates is approximated using FE modelling. The nodal displacements are functions of the angular coordinate  $\theta$  and depend on the assumed wave propagation along this dimension.

The derivation of the waveguide finite element formulation of the tyre dynamic starts with Hamilton's principle. This states that of all possible paths along which a dynamic system can move from one point to another in time and space, the one chosen is always the one that minimises the time integral of the difference between the kinetic and potential energies.

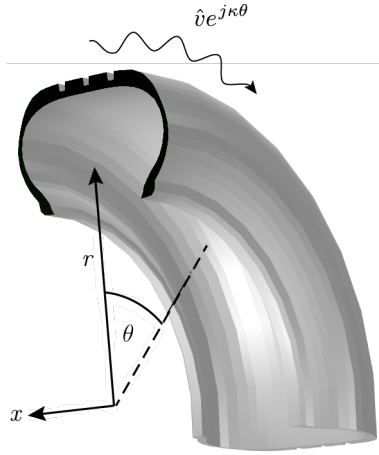


**Fig. 4.2.** The tyre as a curved waveguide: for the cross-section (marked in black) lying in the  $(x, r)$ -plane an FE approximation is used, while in circumferential direction  $\theta$  wave propagation is assumed. Waves travelling in negative  $\theta$  direction have to be considered as well, but are not shown here.

It can mathematically be expressed as [110, Cha. 11.1]

$$\delta \int_{t_1}^{t_2} (U - K + A) dt = 0. \quad (4.2)$$

The term

$$L \equiv U - K + A \quad (4.3)$$

is called the *Lagrangian function*.  $U$  and  $K$  are the strain and kinetic energies of the system, and  $A$  is the potential energy of loading.

By assuming viscoelastic material properties, harmonic motion of type  $e^{j\omega t}$  (where  $t$  is the time and  $j = \sqrt{-1}$ ), and the absence of volume forces and external

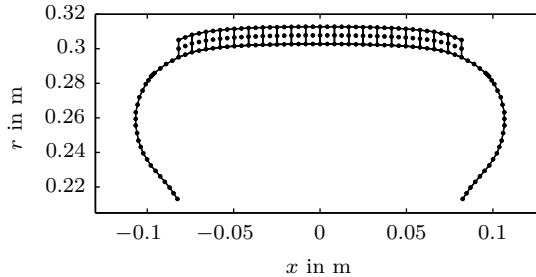


**Fig. 4.3.** WFEM mesh of a slick 205/55 R16 tyre. Each  $\bullet$  represents one node.

traction,  $U$ ,  $K$  and  $A$  can be expressed as (see [75] for detailed derivations)

$$U = \int_V \boldsymbol{\varepsilon}^{aT} \mathbf{D} \boldsymbol{\varepsilon} dV, \quad (4.4a)$$

$$K = \int_V \rho \omega^2 \mathbf{u}^{aT} \mathbf{u} dV, \quad \text{and} \quad (4.4b)$$

$$A = - \int_V (\mathbf{f}^H \mathbf{u} + \mathbf{f}^T \tilde{u}^a) dV. \quad (4.4c)$$

$\boldsymbol{\varepsilon}$  is the engineering strain vector,  $\mathbf{D}$  the complex rigidity matrix,  $\rho$  the density, and  $\mathbf{f}$  the vector of external surface forces.  $(\bullet)^T$  denotes the matrix/vector transpose, and  $(\bullet)^H = (\bullet)^{T*}$ , where  $(\bullet)^*$  is complex conjugate. Finally,  $(\bullet)^a$  indicates the complex conjugate in a mathematically adjoint system with negative damping. The latter is a conceptual trick necessary to allow the formulation of a variational principle for viscoelastic materials. For details the reader is referred to [75].

$u$  in (4.4b) and (4.4c) is replaced by the waveguide finite element displacement formulation (4.1), and  $\boldsymbol{\varepsilon}$  in (4.4a) written in bi-linear form as

$$\boldsymbol{\varepsilon}(r, x, \theta) = \mathbf{E}_0(r, x) \mathbf{v}(\theta) + \mathbf{E}_1(r, x) \frac{\partial \mathbf{v}(\theta)}{\partial \theta}, \quad (4.5)$$

where  $\mathbf{v}$  is the vector of all nodal displacements, and  $\mathbf{E}_0$  and  $\mathbf{E}_1$  are matrices depending on the element-specific strain-displacements relations and shape functions and their derivatives.

The resulting expressions for  $U$ ,  $K$  and  $A$  are inserted into the Lagrangian (4.3). Application of standard procedures for FE element formulation and system assembly gives

$$L = \int_{-\pi}^{\pi} \left( \sum_{n=0}^1 \sum_{m=0}^1 \left( \frac{\partial^n \mathbf{v}^{aT}}{\partial \theta^n} \mathbf{A}_{nm} \frac{\partial^m \mathbf{v}}{\partial \theta^m} \right) - \omega^2 \mathbf{v}^{aT} \mathbf{M} \mathbf{v} - \mathbf{v}^{aT} \mathbf{f} - \mathbf{v} \mathbf{f}^H \right) d\theta, \quad (4.6)$$

where  $\mathbf{A}_{nm}$  are generalised stiffness matrices and  $\mathbf{M}$  the mass matrix. Hamilton's principle (4.2) is applied and from the variation of the displacements in the adjoint system a set of coupled ordinary differential equations is obtained

$$\left[ -\mathbf{A}_{11} \frac{\partial^2}{\partial \theta^2} + (\mathbf{A}_{01} - \mathbf{A}_{10}) \frac{\partial}{\partial \theta} + \mathbf{A}_{00} - \omega^2 \mathbf{M} \right] \mathbf{v}(\theta, \omega) = \mathbf{f}(\theta, \omega). \quad (4.7)$$

#### 4.1.2. Free response, forced response and damping

By setting  $\mathbf{f} = 0$ , the homogeneous case is obtained for which solutions are given by exponential functions of type

$$\mathbf{v}(\theta, \omega) = \mathbf{\Psi}(\omega) e^{-j\kappa\theta}. \quad (4.8)$$

These functions can be physically interpreted as waves of cross-sectional mode shape  $\mathbf{\Psi}$  propagating along the circumferential direction with polar wave number  $\kappa$ . Inserting (4.8) into (4.7) gives

$$(-\mathbf{K}_2 \kappa^2 + \mathbf{K}_1 j\kappa + \mathbf{K}_0 - \omega^2 \mathbf{M}) \mathbf{\Psi} = \mathbf{0}, \quad (4.9a)$$

where

$$\mathbf{K}_0 = \mathbf{A}_{00}, \quad \mathbf{K}_1 = \mathbf{A}_{01} - \mathbf{A}_{10}, \quad \mathbf{K}_2 = -\mathbf{A}_{11}. \quad (4.9b)$$

This is a twin-parameter eigenvalue problem in  $\omega$  and  $\kappa$  for which two solution strategies exist. The first option is to specify the frequency  $\omega$  for which the problem should be solved. In this case a quadratic eigenvalue problem follows. The other possibility is to set  $\kappa$  to a particular wave order, which means that (4.9a) reduces to a linear eigenvalue problem, which is easier to solve than the quadratic one. It also has the advantage that the physical meaning of the fixed value and the solutions to the eigenvalue problem are straightforward to understand. Because of the periodicity condition around the tyre circumference,  $\kappa$  can only be set to an integer number  $n$ . This number represents the order, i.e. the number of full wave lengths, of the wave motion in circumferential direction. For any particular  $n$ , a set of eigenvalues  $\omega_{n,s}^2$  and eigenvectors  $\mathbf{\Psi}_{n,s}$  will be the solution to (4.9a). Herein,

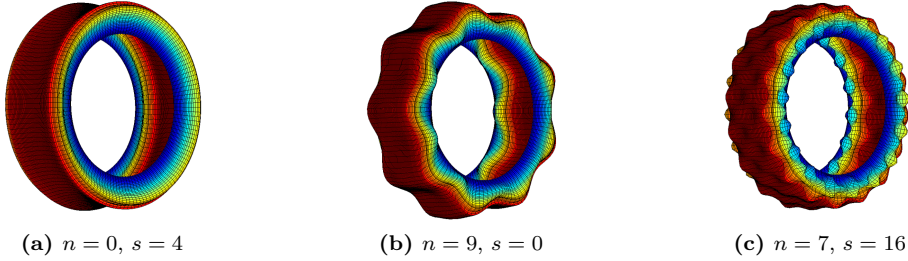


**Fig. 4.4.** Examples for three free response solutions of type  $\Psi_{n,s} e^{-jn\theta}$ . Note that due to the wave ansatz, these deformation shapes are not stationary in circumferential direction but move around the tyre. Exceptions are solutions for  $n = 0$ .

each  $s$  represents one solution over the cross-section, i.e. one cross-sectional mode shape<sup>1</sup>. Examples for three different  $\Psi_{n,s}$  are shown in Fig. 4.4.

Applying this ansatz to (4.9a) it is

$$(-\mathbf{K}_2 n^2 + \mathbf{K}_1 j n + \mathbf{K}_0 - \omega_{n,s}^2 \mathbf{M}) \Psi_{n,s} = 0. \quad (4.10)$$

If damping is disregarded, then all  $\mathbf{K}_i$ , ( $i = 0, 1, 2$ ), and the  $\mathbf{M}$  are real and symmetric or skew-symmetric. From this the following relation between waves travelling in positive ( $n > 0$ ) and negative circumferential direction ( $n < 0$ ) can be deduced:

$$\omega_{-n,s} = \omega_{n,s} \quad (4.11a)$$

$$\Psi_{-n,s} = \Psi_{n,s}^*. \quad (4.11b)$$

In [79] it is shown that for proportional damping of type  $\bar{\mathbf{K}}_i = (1 + j\eta(\omega))\mathbf{K}_i$ , (where  $i = 0, 1, 2$  and  $\eta(\omega)$  being the loss factor) the inhomogenous version of (4.9a) is given by

$$(-\bar{\mathbf{K}}_2 n^2 + \bar{\mathbf{K}}_1 j n + \bar{\mathbf{K}}_0 - \omega^2 \mathbf{M}) \Xi_n \mathbf{C}_n = \mathbf{F}_n(\omega). \quad (4.12)$$

<sup>1</sup>There is always some confusion in the use of the terms *modes* and *waves* in connection with tyres. Due to the wave ansatz and the high structural damping, it is appropriate to speak of *waves* in circumferential direction. The solutions for the cross-sectional motion are obtained as the eigenvectors for a particular  $n$ , which is similar to how mode shapes are obtained for simpler structures. Hence, the cross-sectional motion will be referred to as *modes*.

Herein,  $\Xi_n$  is a matrix collecting all free response eigenvectors  $\Psi_{n,s}$  for a specific  $n$ .  $\mathbf{C}_n$  are the amplitudes of the cross-sectional modes  $s$  contributing to circumferential order  $n$ .  $\mathbf{F}_n(\omega)$  results from the expansion of the excitation force  $\mathbf{f}(\theta, \omega)$  into circumferential orders. For a tyre circumference which is discretised into  $C$  equidistant intervals of length  $\Delta$ , and a excitation force which is piece-wise constant over the interval  $\theta \in [\theta_c - \Delta/2, \theta_c + \Delta/2]$ , this expansion gives

$$\mathbf{F}_n(\omega) = \sum_{c=1}^C \mathbf{F}_{lat}(\omega) \frac{\sin(n\Delta/2)}{n\pi\Delta} e^{jn\theta_c}, \quad (4.13)$$

where  $\mathbf{F}_{lat}$  is the lateral force distribution. By multiplying both sides of (4.12) from the left with  $\Xi_n^H$ , the orthogonality property of the cross-sectional modes can be used to derive the modal amplitudes as

$$C_{n,s}(\omega) = \frac{\Psi_{n,s}^H \mathbf{F}_n(\omega)}{[(1 + j\eta(\omega))\omega_{n,s}^2 - \omega^2]m_{n,s}}. \quad (4.14)$$

The factor  $m_{n,s}$  is the modal mass, which is given by the orthogonality relation

$$\delta_{s,t}m_{n,s} = \Psi_{n,s}^H \mathbf{M} \Psi_{n,t}, \quad (4.15)$$

where  $\delta$  is the Kronecker symbol. Similar to (4.11b) it is

$$m_{-n,s} = m_{n,s}. \quad (4.16)$$

The total displacement field on the tyre,  $\mathbf{v}(\theta, \omega)$ , can finally be obtained as a summation of the contribution of  $S$  cross-sectional modes and  $-N$  to  $N$  circumferential waves

$$\begin{aligned} \mathbf{v}(\theta, \omega) &= \sum_{n=-N}^N \sum_{s=1}^S C_{n,s} \Psi_{n,s} e^{-jn\theta} \\ &= \sum_{n=-N}^N \sum_{s=1}^S \frac{\Psi_{n,s}^H \mathbf{F}_n(\omega)}{[(1 + j\eta(\omega))\omega_{n,s}^2 - \omega^2]m_{n,s}} \Psi_{n,s} e^{-jn\theta}. \end{aligned} \quad (4.17)$$

By virtue of relations (4.11) and (4.16), this can be written as

$$\mathbf{v}(\theta, \omega) = \sum_{n=0}^N \left( \sum_{s=1}^S A_{n,s} \Psi_{n,s} e^{-jn\theta} + \sum_{s=1}^S B_{n,s} \Psi_{n,s}^* e^{jn\theta} \right). \quad (4.18)$$

For  $n > 0$  the amplitudes  $A_{n,s}$  and  $B_{n,s}$  are given as

$$A_{n,s}(\omega) = \frac{\mathbf{\Psi}_{n,s}^H \mathbf{F}_n(\omega)}{[(1 + j\eta(\omega))\omega_{n,s}^2 - \omega^2]m_{n,s}} \quad (4.19a)$$

$$B_{n,s}(\omega) = \frac{\mathbf{\Psi}_{n,s}^T \mathbf{F}_{-n}(\omega)}{[(1 + j\eta(\omega))\omega_{n,s}^2 - \omega^2]m_{n,s}}. \quad (4.19b)$$

For the special case  $n = 0$  it is

$$A_{0,s}(\omega) = \frac{\mathbf{\Psi}_{n,s}^H \mathbf{F}_{lat}(\omega)}{\pi[(1 + j\eta(\omega))\omega_{n,s}^2 - \omega^2]m_{n,s}} \quad (4.20a)$$

$$B_{0,s}(\omega) = 0. \quad (4.20b)$$

By using (4.18) instead of (4.17) the computational burden can be significantly reduced as the eigenvalue problem (4.10) only needs to be solved  $N + 1$  times instead of the original  $2N + 1$  times.

The described modal summation procedure is not the only possible way to solve the inhomogenous version of (4.7). With a direct procedure as described in [78] the total displacement field is obtained by formulating (4.7) individually for each circumferential wave order  $n$ . This equation is solved using matrix inversion. The total displacement field is finally obtained by summation of all circumferential solutions. The advantage of the direct procedure is that it allows to use a non-proportional damping approach in which different parts of the structure can be assigned different loss factors. The modal summation approach requires<sup>2</sup> a proportional damping model in which all parts of the tyre have the same (frequency dependent) damping. Considering the large variation in viscoelastic properties between the different tyre materials (e.g. steel and rubber), a non-proportional damping approach is certainly favourable. However, there are also considerable disadvantages associated with the direct procedure: the computational burden can be quite significant<sup>3</sup> as the matrix inversion has to be performed for every  $\omega$  and  $n$ . More important, in the direct procedure the displacement field can only be expanded in terms of individual circumferential wave orders, but not in terms of individual cross-sectional modes. As will be seen in Sec. 4.3.3, a cross-sectional expansion is necessary for the radiation calculations. This is the main reason why an modal summation approach is used in this study.

<sup>2</sup>It is possible to use non-proportional damping while solving (4.10) to obtain damped, i.e. complex, eigenvectors and eigenvalues. However, since the orthogonality relations no longer lead to matrix diagonalisation, the step from (4.12) to (4.14) is no longer possible.

<sup>3</sup>For the typical case considered in this study the modal summation approach is around ten times faster than the direct procedure.

### 4.1.3. Element formulation

Only the belt and the tread of the tyre are modelled. The air cavity is not explicitly modelled as the fluid/structure coupling is of minor relevance for tyre vibrations [66] unless hub forces are considered. The wheel is also not included in the model. Tyre motion is blocked at the bead.

As very detailed derivations of the shell and solid elements used in the WFE tyre model can be found in [75, 78], only a very brief overview is given in the following. Isotropic, two-dimensional solid elements of Lagrange type with nine nodes are used for the tread. Anisotropic, doubly-curved deep shell elements accounting for rotational inertia, shearing across the thickness, and pretension due to tyre inflation, are used for the sidewalls and the belt in the tyre cross-section modelling. The shape functions are quadratic. While in general linearised strain-displacement relations are used, it is necessary to retain quadratic terms for expressions involving the membrane strains due to pretension [78]. In Sec. 3.3.3 it was stated that tyre/road contact models which are based on a convolution approach can only be formulated for linear tyre models. This requirement is not violated by the non-linear pretension terms used in the shell formulation. The pretension terms merely define an initial equilibrium state for the shell elements about which small, linearised vibrational motion is executed. As the pretension does not change during a simulation, only linear effects are included in the dynamic response of the tyre. The existence of the tyre's Green's function is assured.

### 4.1.4. Advantages of WFEM

Compared to purely analytical or numerical tyre models, the presented WFEM approach has several advantages which make it particularly useful for a study as presented here. By modelling the cross-section with individual elements, WFEM can better account for the complex geometry and material properties of a tyre than can analytical models. Furthermore, by applying a wave approach in the circumferential direction, the computational burden is significantly reduced compared to FE models. The results are also more readily interpretable as the contributions of individual wave orders can easily be identified. Additionally, the geometrical accuracy in the cross section and the numerical efficiency imply that the usable frequency range is larger than when either analytical or FE modelling are used. As results can be analysed in any combination of frequency, wave-order and/or cross-sectional distribution, the data obtained is detailed enough to evaluate the interrelationship between rolling noise and rolling resistance. Moreover, the numerical effort is small enough to allow for extended parameter studies.

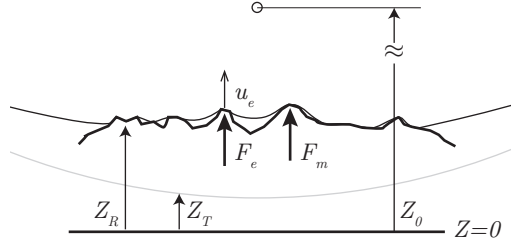


**Fig. 4.5.** Contact geometry between tyre and road. The reference surface is located at  $Z = 0$ , the rim centre at  $Z_0$ , the undeformed tyre contour (grey) is given by  $Z_T$  and the road roughness profile by  $Z_R$ .  $F_e$  and  $F_m$  are the contact forces acting at points  $e$  and  $m$ , and  $u_e$  is the dynamic response of the structure in point  $e$ .

## 4.2. The tyre/road interaction model

### 4.2.1. Basic contact formulation

The contact model is based on the convolution approach as presented by Kropp [88] and its subsequent enhancements by several authors [91, 111, 90, 78].

The time-dependent position of a point  $e$  on the tyre surface can be written as

$$Z_e(t) = Z_0(t) - Z_{T,e}(t) + u_e(t), \quad (4.21)$$

where  $Z_0(t)$  and  $Z_{T,e}(t)$  are the position of the rim centre and the tyre contour as shown in Fig. 4.5.  $u_e(t)$  is the dynamic structural response at point  $e$  which is caused by the present and past forces at all contact points  $m$ . For a linear time-invariant system it is given as

$$u_e(t) = \sum_m F_m(t) * g_{m,e}(t) \quad (4.22a)$$

$$= \sum_m \int_{-\infty}^{\infty} F_m(\tau) g_{m,e}(t - \tau) d\tau. \quad (4.22b)$$

$*$  is the convolution operator and  $g_{m,e}$  is the displacement Green's function in the Eulerian reference frame for a point  $e$  due to a force at point  $m$ . Assuming causality and that the system is at rest for times  $t < 0$ , a time discretised version

of (4.22b) for  $t_N = N\Delta t$  is obtained as

$$u(N\Delta t) = \sum_m \sum_{n=0}^N F_m g_{m,e}((N-n)\Delta t)\Delta t \quad (4.23a)$$

$$\begin{aligned} &= \sum_m F_m(t_N) g_{m,e}(0)\Delta t \\ &+ \sum_m \sum_{n=0}^{N-1} F_m g_{m,e}((N-n)\Delta t)\Delta t. \end{aligned} \quad (4.23b)$$

As the second term in (4.23b) represents past, known values of the contact forces, it can be considered a constant at each time step. As a matrix expression for all possible contact points  $m$ , (4.23b) becomes

$$\mathbf{u}(t_N) = \mathbf{G}_0 \mathbf{F}(t_N) + \mathbf{u}_{old}(t_N). \quad (4.24)$$

Here,  $\mathbf{G}_0$  is a  $m \times m$  matrix containing the values of the Green's functions for  $t = 0$ . Besides the displacements  $\mathbf{u}(t_N)$  also the contact forces  $\mathbf{F}(t_N)$  are still unknown in (4.24). By defining  $\Delta \mathbf{u}(t_N) = \mathbf{u}(t_N) - \mathbf{u}_{old}(t_N)$ , (4.24) can be rearranged to

$$\mathbf{F}(t_N) = \mathbf{G}_0^{-1} \Delta \mathbf{u}(t_N). \quad (4.25)$$

The inverse  $\mathbf{G}_0^{-1}$  is called the influence matrix. It is only defined when the first values of the Green's function are not zero.

From the boundary conditions at the tyre/road interface follows

$$\mathbf{F}(t_N) \geq \mathbf{0} \quad (4.26a)$$

$$\mathbf{d}(t_N) = Z_T(t_N) + \mathbf{u}_{old}(t_N) + \Delta \mathbf{u}(t_N) - Z_R(t_N) \geq \mathbf{0} \quad (4.26b)$$

$$\mathbf{F}(t_N)^T \mathbf{d}(t_N) = 0, \quad (4.26c)$$

where  $Z_R$  is the road roughness profile as shown in Fig. 4.5.

Under the omission of adhesion, these conditions state that for each time step  $t_N$  there are only two valid states for each contact points  $e$ : tyre and road are either in contact with  $d_m(t_N) = 0$  and a positive compression force  $F_m(t_N)$ , or they are separated by a distance  $d_m(t_N) > 0$ , in which case the contact force  $F_m(t_N) = 0$ .

A non-linear contact problem is formed by (4.25) and the contact constraints (4.26a), (4.26b) and (4.26c). This can be solved iteratively for every time step using for example the (damped) Newton-Raphson algorithm [78, 91].

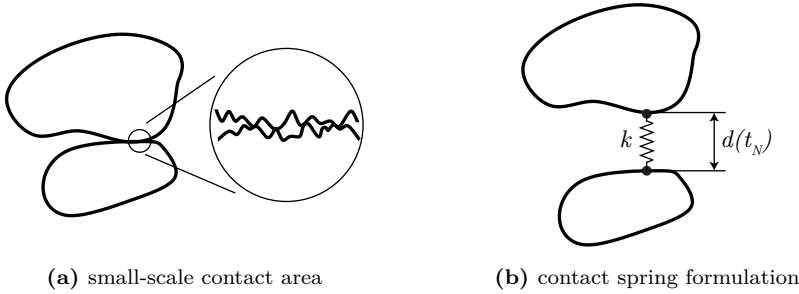


**Fig. 4.6.** (a) Due to small-scale surface roughness the real area of contact is smaller than the apparent. (b) contact springs are introduced to account for this effect.

#### 4.2.2. Contact springs

As has been pointed out in Sec. 3.3.3, small-scale roughness phenomena can have a considerable effect on the contact behaviour. The difference between the apparent and the real area of contact affects the contact stiffness (see Figures 3.2 and 4.6a). Moreover, as shown in Fig. 3.3, the real area of contact, and with it the contact stiffness, also changes during the contact duration. In order to account for both effects, Andersson and Kropp [91] suggested to introduce non-linear contact springs between the contact points as shown in Fig. 4.6b.

A similar approach is introduced here. Yet, as the determination of the non-linear contact stiffnesses is a rather advanced task, only contact springs with constant stiffness are used. This means that difference between real and apparent area of contact is included, while the change of contact area during contact is not.

The set of equations (4.26) is reformulated to read

$$F_e(t_N) = kd_e(t_N)\mathcal{H}(d_e(t_N)) \quad (4.27a)$$

$$\mathbf{d}(t_N) = Z_R(t_N) - Z_T(T_N) - \Delta\mathbf{u}(t_N) - \mathbf{u}_{old}(t_N), \quad (4.27b)$$

with the spring stiffness  $k$  and the Heaviside operator  $\mathcal{H}$ . (4.27) and (4.25) formulate a new non-linear contact problem which can be solved to obtain the time-dependent contact forces in the Eulerian reference frame. The contact forces are then rotated around the tyre and Fourier transformed to yield the frequency dependant forces in the Lagrangian coordinate system.

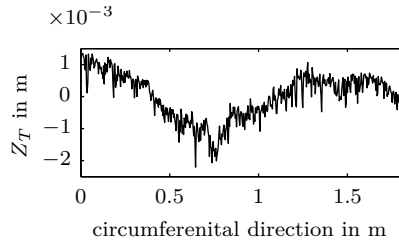


**Fig. 4.7.** Example for a road surface profile with pronounced waviness. The position where the static loading is performed influences the average contact force during rolling.

### 4.2.3. Implementation details and input parameters

The tyre/road contact modelling is divided into two phases: stationary loading and rolling. During the stationary loading phase, the tyre is slowly pressed onto a road patch until a the required axle load  $F_z$  is reached. This determines the distance between tyre hub and road, which is kept constant in the following. Now the rolling phase starts. For each time step, the used regions from the tyre and road surface profiles are shifted in accordance with the contact resolution. Using  $u_{old}$  from the previous time step, the contact force is calculated. Quasi steady state conditions are reached after two or three revolutions when low-frequency oscillations which have been induced by the start of rolling have died out.

It has to be pointed out that the procedure of keeping the tyre/road approach constant during rolling has some implications. In particular the total contact force will vary with each time step. Especially for roads with a pronounced waviness, see Fig. 4.7, these variations can be 20 % and more. Physically this is not unreasonable as it resembles the influence of the inertia of the car body and the suspension on the tyre/road contact. The effect has in any case to be taken into account when for example the rolling resistance coefficient is calculated.

Even without a non-linear formulation, it is not straightforward to determine an appropriate value for the contact spring stiffness  $k$ . Initial tries to estimate  $k$  based on comparisons of measured and simulated tyre footprints were not successful. In [78] an value for  $k$  was determined under the assumption that the real area of contact is 10 % the size of the apparent one. This led to a contact spring stiffness of  $k \approx 5 \cdot 10^4$  N/m for a slick 205/55 R16 tyre. Here, the same  $k$  is used as starting value for a small parameter study.

To obtain accurate results, three-dimensional roughness data is necessary, i.e. it is not sufficient to include only one roughness track along the circumferential direction, the roughness variation along the lateral direction must also be accounted

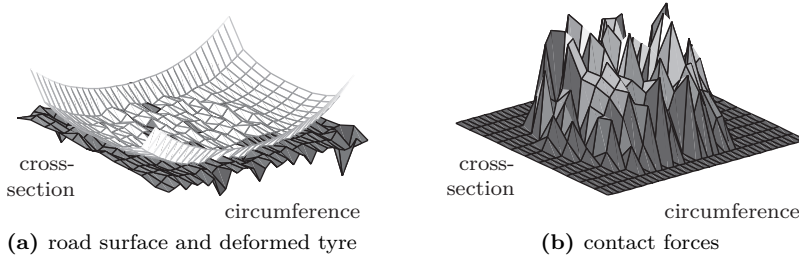


**Fig. 4.8.** Example for tyre/road interaction.

for [56, Paper C].

Road surface profiles are based on detailed laser scans of drum-mounted road patches or test fields. The spatial resolution is 0.2 mm in rolling direction and scans of at least 15 parallel lateral tracks are available. The data is resampled to match the resolution of the tyre model. In most cases the tyre is divided into 512 intervals over the circumference, giving a circumferential contact revolution of slightly less than 4 mm. In lateral direction, the contact size is associated with the size of the solids elements in the WFE model. Depending on mesh configuration, this gives 12 to 18 contact tracks, which is a sufficiently high number for rolling noise calculations [56, Paper C]. An example for a calculated tyre/road sample is given in Fig. 4.8.

## 4.3. The half-space boundary element method radiation model

### 4.3.1. Governing equations

Basis for the for radiation calculations using the half-space BEM is the Helmholtz equation for an homogenous, non-moving medium (time dependence  $e^{j\omega t}$  assumed)

$$\nabla^2 p(\vec{x}) + k_0^2 p(\vec{x}) = -\varphi(\vec{x}), \quad (4.28)$$

where  $p(\vec{x})$  is the sound pressure at at point  $\vec{x} = (X, Y, Z)$  inside the domain  $V$ .  $\nabla^2$  is the Laplace operator,  $k_0 = \omega/c_0$  the wave number and  $c_0$  the speed of sound in the acoustic domain.  $\varphi(\vec{x})$  is a spatially distributed source function representing contribution from harmonic acoustic sources within  $V$ .

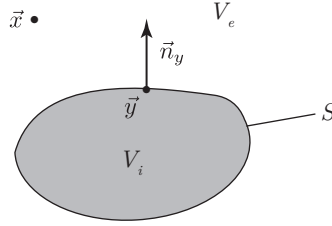


**Fig. 4.9.** Domain definition for the exterior BEM problem: the internal domain  $V_i$  is separated from the external domain  $V_e$  by the surface  $S$ . The point  $\vec{x}$  is located in  $V_e$  and  $\vec{x}$  is located on  $S$ .  $\vec{n}_y$  is the normal vector to the surface  $S$  in point  $\vec{y}$ .

A Green's function  $g(\vec{x}, \vec{y})$  is the solution for Eq. (4.28) for a point source at  $\vec{y} = (X_s, Y_s, Z_s)$

$$\nabla^2 g(\vec{x}, \vec{y}) + k_0^2 g(\vec{x}, \vec{y}) = -\delta(\vec{x}, \vec{y}), \quad (4.29)$$

with  $\delta(\vec{x}, \vec{y})$  as Dirac delta function. For an unbounded three-dimensional space  $g(\vec{x}, \vec{y})$  is

$$g(\vec{x}, \vec{y}) = \frac{e^{-jk_0 r}}{4\pi r}, \quad (4.30)$$

where  $r = \|\vec{x} - \vec{y}\| = \sqrt{(X - X_s)^2 + (Y - Y_s)^2 + (Z - Z_s)^2}$  is the distance between the points  $\vec{x}$  and  $\vec{y}$ .

Multiplication of (4.28) with  $g(\vec{x}, \vec{y})$  and (4.29) with  $p(\vec{x})$ , and subsequent subtraction of (4.28) from (4.29) combines the two equations. After integration over the domain  $V$ , indirect application of Green's second identity, and some algebra (see e.g. [100]) the Kirchhoff-Helmholtz integral equation for exterior problems as shown in Fig. 4.9 results as

$$C(\vec{x}) p(\vec{x}) = - \int_S \left( p(\vec{y}) \frac{\partial g(\vec{x}, \vec{y})}{\partial \vec{n}_y} + j\omega \rho_0 v_n(\vec{y}) g(\vec{x}, \vec{y}) \right) dS_y + p_{\text{inc}}(\vec{x}), \quad (4.31)$$

with

$$C(\vec{x}) = \begin{cases} 1 & \vec{x} \text{ in the exterior domain } V_e \\ \frac{1}{2} & \vec{x} \text{ on the surface } S \\ 0 & \vec{x} \text{ in the interior domain } V_i. \end{cases} \quad (4.32)$$

Herein,  $\vec{y}$  is taken to lie on the boundary  $S$  between the inner and exterior domains  $V_i$  and  $V_e$ .  $\vec{x}$  is located in  $V_e$  and  $\frac{\partial g(\vec{x}, \vec{y})}{\partial \vec{n}_y}$  is the directional derivative of  $p(\vec{y})$  in the direction of the normal vector  $\vec{n}_y$  at the surface interval  $dS_y$ .  $\rho_0$  is the density of the acoustic medium and  $v_n$  is the normal velocity on  $dS_y$ . The contribution of an external incident sound field  $p_{\text{inc}}(\vec{x})$  is given as

$$p_{\text{inc}}(\vec{x}) = \int_V \varphi(\vec{y}) g(\vec{x}, \vec{y}) dX_S dY_S dZ_S. \quad (4.33)$$

Physically, the right hand side of (4.31) can be interpreted as the contribution of individual volume sources (i.e. monopoles  $j\omega\rho_0 v_n(\vec{x})g(\vec{x}, \vec{y})$ ), and pressure sources (i.e. dipoles  $p(\vec{y}) \frac{\partial g(\vec{x}, \vec{y})}{\partial \vec{n}_y}$ ) located on the surface  $S$  to the sound pressure  $p(\vec{x})$ .

### 4.3.2. Numerical implementation

The surface  $S$  is discretised into  $N$  surface elements and the point  $\vec{x}_m, m = 1 \dots N$ , is subsequently placed at the centres of all elements. For each position  $m$ , the contribution from all surface intervals  $j = 1 \dots N$  is calculated. This gives  $N$  equations of form

$$\frac{1}{2}p(\vec{x}_m) = - \sum_{j=1}^N \int_{S_j} \left( p(\vec{y}) \frac{\partial g(\vec{x}_m, \vec{y})}{\partial \vec{n}_y} + j\omega\rho_0 v_n(\vec{y}) g(\vec{x}_m, \vec{y}) \right) dS_y + p_{\text{inc}}(\vec{x}_m). \quad (4.34)$$

Replacing  $S_y$  with constant planar elements and application of one-point Gauss-Legendre quadrature yields

$$\frac{1}{2}p(\vec{x}_m) = - \sum_{j=1}^N \left( p(\vec{y}_j) \frac{\partial g(\vec{x}_m, \vec{y}_j)}{\partial \vec{n}_{y_j}} + j\omega\rho_0 v_n(\vec{y}_j) g(\vec{x}_m, \vec{y}_j) \right) \Delta S_{y_j} + p_{\text{inc}}(\vec{x}_m). \quad (4.35)$$

Stepping through all points  $\vec{x}_m, m = 1 \dots N$ , on the surface, the following matrix equation is obtained

$$\mathbf{C}\mathbf{p}_S = \mathbf{H}\mathbf{p}_S + j\omega\rho_0 \mathbf{G}\mathbf{v}_S + \mathbf{p}_{\text{inc}}. \quad (4.36)$$

Here,  $\mathbf{p}$  and  $\mathbf{v}$  denote the pressure and the normal velocity at the surface elements. The kernel functions  $\frac{\partial g(\vec{x}_m, \vec{y}_j)}{\partial \vec{n}_{y_j}}$  and  $g(\vec{x}_m, \vec{y}_j)$  are included in the matrices  $\mathbf{H}$  and  $\mathbf{G}$ , and  $\mathbf{C} = \frac{1}{2}\mathbf{I}$ , with  $\mathbf{I}$  as identity matrix.

Depending on the boundary conditions,  $\mathbf{v}_S$  or  $\mathbf{p}_S$  or a combination of both are known in (4.36). Sorting the unknown and known parts into left- and right-hand side terms, a set of equations of the form

$$\mathbf{A}\mathbf{x}_S = \mathbf{b} \quad (4.37)$$

is obtained. The solution  $\mathbf{x}_S$  gives the unknown boundary values on  $S$ . Now that both  $\mathbf{v}_S$  and  $\mathbf{p}_S$  are known on  $S$ , (4.31) can be solved for an arbitrary receiver position  $\vec{x}$  in the exterior domain. The procedure involves the same discretisation steps as for Equations (4.34) and (4.34), and yields

$$p(\vec{x}) = p_{\text{inc}}(\vec{x}_m) - \sum_{m=1}^N \left( p(\vec{y}_m) \frac{\partial g(\vec{x}, \vec{y}_m)}{\partial \vec{n}_{y_m}} + j\omega\rho_0 v_n(\vec{y}_m) g(\vec{x}, \vec{y}_m) \right) \Delta S_{y_m}. \quad (4.38)$$

The numerically critical step in BEM is solving (4.37) as the matrix  $\mathbf{A}$  has some unfavourable properties. It is fully populated and, as the surface intervals  $\Delta S_{y_j}$  do not need to be of equal size, not necessarily symmetric. If, in order to avoid non-uniqueness problems, CHIEF points are added (cf. [112, Cha. 3]),  $\mathbf{A}$  is not even quadratic. As a consequence, storage and computation costs can be quite substantial in BEM.

### 4.3.3. Tyre/road noise specialities

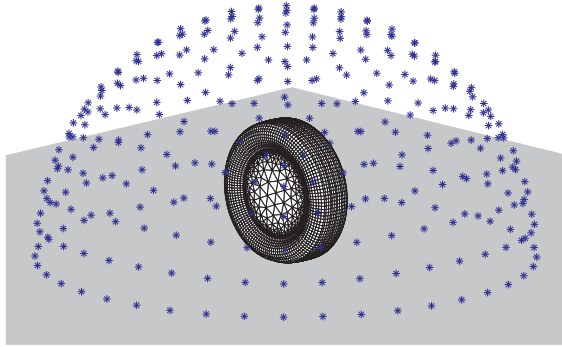


**Fig. 4.10.** The BEM tyre representation, the reflecting ground and the evaluation surface.

In the case of the tyre/road noise simulations, the domain surface  $S$  is the tyre surface and the vibrational field on the tyre gives the normal surface velocity  $\mathbf{v}$

in (4.36). Accordingly, the solution of (4.37) gives the surface pressure  $\mathbf{p}_S$  and (4.31) can be used to calculate the sound pressure at any arbitrary point around the tyre, for example on an evaluation half-sphere as shown in Fig. 4.10.

An important property which has been left out so far is the reflection at the road surface. In principal, the ground could simply be included in the BEM calculations as another discretised body. However, this raises the already high computational costs even further. It is numerically more efficient to modify the Green's function (4.30) to include the effect of the ground reflection:

$$g(\vec{x}, \vec{y}) = \frac{e^{-jk_o r_1}}{4\pi r_1} + \frac{e^{-jk_o r_2}}{4\pi r_2}. \quad (4.39)$$

Here,  $r_1 = \|\vec{y} - \vec{x}\|$  and  $r_2 = \|\vec{y} - \vec{x}'\|$ , where  $\vec{x}$  is the position of the receiver and  $\vec{x}'$  is the position of  $\vec{x}$  after having been mirrored at the ground plane. Eq. (4.39) is valid for the case of a perfectly rigid ground, i.e. the normal ground impedance is  $Z_p = \infty$ . Formulations for arbitrary ground impedances, which are for example necessary to model reflection at porous asphalt surfaces, have been shown by Brick [100]. Within this work only the rigid case is considered.

Numerically problematic is the simulation of the sound radiation out of the contact region. In area high surface velocities on the tyre coincide with very narrow gaps between tyre and road. This leads to near-singular conditions. To deal with this problem, a two step process is used. First, the tyre is lifted by 1 mm from the road surface. Secondly, a unique adaptive integration routine as proposed in [100] is used. Elements close to or in the contact region are sub-divided into intervals proportional to the relative distance between element and ground. Gauss-Legendre integration points are then assigned to these sub-elements. The Green's functions and their derivatives are finally given by the sum of the sub-interval values. Using this approach, calculation times are not significantly affected as the total number of elements does not change. The validity of this procedure has been proven by Brick [100] for calculations of the horn-effect.

The spatial resolution of the tyre's vibrational field, which serves as the input data for the BEM calculations, is given by the cross-sectional WFEM mesh and the circumferential tyre discretisation as used in the contact modelling. However, it is neither physically nor numerically useful to use the full available resolution. If a maximum frequency of interest of 3400 Hz is assumed, the smallest wave length in air is 0.1 m. Applying a six elements per wave length criterion, elements can be 1.67 cm long. The length of the bead to bead cross section perimeter of the 175/65 R14 tyre considered in this study is 0.35 m and the circumference is 1.82 m. This means that 21 boundary elements over the cross section and 109 over the circumference are sufficient to fulfil the wave length criteria for the air-borne part. The situation is more complicated for the structure-borne part, as there is no simple rule to determine the necessary the number of wave lengths which are to

be considered for a specific frequency. This is due to the complex interaction between cross-sectional and circumferential motion, the variety of different wave types, the complex dispersion relations and the large number of existing modes for higher frequencies (cf. [77]). Yet, in [79] it was shown that due to their radiation efficiency mainly low-order tyre modes are responsible for sound radiation in the frequency range up to 3400 Hz. This means that not all vibrational orders actually need to be considered for the radiation calculations. In [79] good agreement to measurements was achieved for a maximum order of 24 in circumferential direction and 20 over the cross-section. The same range of orders is used here. Under this condition the required resolution for the airborne part is also sufficient for an accurate description of the vibrational field. The final BEM mesh needs only a fourth of the circumferential resolution and roughly a half of the cross-sectional resolution of the equivalent vibrational mesh.

While describing the possible solution strategies for the inhomogenous form of (4.7) in Sec. 4.1.2, it was stated that an essential feature of the modal summation approach, and something which is not offered by the direct procedure, is the possibility to expand the vibrational field in cross-sectional modes. Without this property it would not be possible to limit the vibrational field for the BEM calculations to just the first cross-sectional modes. The BEM mesh would need to have the same resolution as required by the tyre vibrations. The number of elements in matrix  $A$  in (4.37) would increase from approximately  $(7 \cdot 10^3)^2$  to  $(2 \cdot 10^4)^2$ . Considering the implications this has on storage requirement and calculation times, it becomes clear why the direct procedure is not an option for tyre/road noise calculations.

The importance of the tyre/road geometry in the contact region for the amplification of sound by the horn effect has been discussed in Sec. 2.2.3. In view of this, the BEM mesh is not based on the original undeformed tyre shape, but on the deformed tyre shape under static loading. The difference is shown in Fig. 4.11. The BEM mesh is completed by adding rigid wheel covers on both tyre sides, see Fig. 4.10. Eleven CHIEF points are randomly distributed inside the tyre to avoid numerical irregularities.

The radiation is evaluated as mean sound pressure at 321 points on a half-sphere of radius 1 m around the contact point between tyre and road.

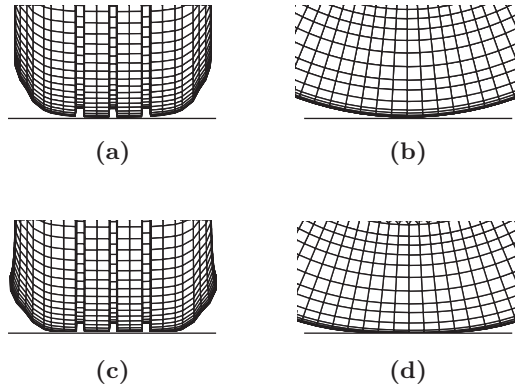


**Fig. 4.11.** The effect of static deformation on the BEM mesh. (a) front view undeformed mesh, (b) side view undeformed mesh, (c) front view deformed mesh, and (d) side view deformed mesh.

#### 4.4. Calculating rolling resistance

Due to energy conservation, rolling losses can be calculated as input power for steady-state rolling conditions. The most general expression for the time-averaged input power into the tyre is given as

$$P_{\text{in}} = \frac{1}{T} \sum_i \int_0^{2\pi} \int_0^T F_i(t, \theta) \frac{\partial v_i(t, \theta)}{\partial t} dt d\theta. \quad (4.40)$$

Herein,  $F_i$  and  $\partial v_i/\partial t$  denote the contact force respectively tyre velocity for the lateral contact track  $i$ . In [35] it is shown that for a WFE tyre model the equivalent expression in the frequency and circumferential wave order domains is given as

$$P_{\text{in}} = 2\pi \sum_{n=-N}^N \sum_{m=0}^M j\omega_m [\mathbf{F}_{-n}^H(\omega_m) \cdot \mathbf{v}_{-n}(\omega_m) - \mathbf{F}_n^T(\omega_m) \cdot \mathbf{v}_n^*(\omega_m)]. \quad (4.41)$$

The nodal forces  $\mathbf{F}_{\pm n}$  are given by (4.13) and the nodal displacements  $\mathbf{v}_{\pm n}$  can be obtained from (4.17) by calculating the individual circumferential wave order contributions separately. (4.41) conveniently allows the identification of the contribution of individual wave orders or frequencies to the rolling losses.

Using (4.7),  $\mathbf{F}_n(\omega_m)$  can be replaced by

$$[\mathbf{A}_{00} + jn\mathbf{A}_{01} - jn\mathbf{A}_{10} + n^2\mathbf{A}_{11} - \omega^2\mathbf{M}] \mathbf{v}_n(\omega_m) = \mathbf{F}_n(\omega_m), \quad (4.42)$$

giving the internally dissipated power  $P_{\text{diss}}$

$$P_{\text{diss}} = 2\pi \sum_{n=-N}^N \sum_{m=0}^M j\omega_m \cdot \left[ \mathbf{v}_{-n}^H \left( \mathbf{A}_{00}^H + jn\mathbf{A}_{01}^H - jn\mathbf{A}_{10}^H + n^2\mathbf{A}_{11}^H - \omega^2\mathbf{M}^H \right) \mathbf{v}_{-n} - \mathbf{v}_n^T \left( \mathbf{A}_{00}^T - jn\mathbf{A}_{01}^T + jn\mathbf{A}_{10}^T + n^2\mathbf{A}_{11}^T - \omega^2\mathbf{M}^T \right) \mathbf{v}_n^* \right], \quad (4.43)$$

where for the sake of readability the  $\omega_m$  dependence of  $\mathbf{v}_{\pm n}$  has been omitted. For completeness, the Hermitian of  $\mathbf{M}$  is retained in the second line even though only real mass matrices are considered here. Obviously, it is  $P_{\text{diss}} = P_{\text{in}}$ . The special property of (4.43) is, that it also holds when not the assembled stiffness and mass matrices of the global tyre structure are used, but the element-specific matrices. This way dissipation can be calculated element-wise, which allows to identify the spatial dissipation distribution over the tyre cross section.

In the following also the term  $P_{\text{loss}}$  will be used for the rolling losses if the distinction between  $P_{\text{diss}}$  or  $P_{\text{in}}$  is of no relevance.

Disregarded has been so far that part of the work which is done during contact is used to deform the contact springs. As these represented the interaction between the road asperities and the highly damped tread, it is desirable to account for these losses as well, when rolling resistance is calculated.

From the definition of the loss factor [113]

$$\eta = \frac{E_{\text{loss}}}{2\pi E_{\text{rev}}}, \quad (4.44)$$

where  $E_{\text{loss}}$  is the lost energy and  $E_{\text{rev}}$  the reversible energy, it follows that  $E_{\text{loss}} = 2\pi\eta_k F_k^2/k$ . It has been made use of  $E_{\text{rev}} = E_{\text{pot}} = F_k^2/k$ , where  $F_k$  is a spring force. Dividing by  $T$  to obtain the power and taking the time-average it is

$$P_{k,i} = \frac{1}{T^2} \int_0^T 2\pi\eta \frac{F_k^2}{k} dt \quad (4.45a)$$

$$= \frac{1}{N^2\Delta t} \sum_{n=0}^N 2\pi\eta \frac{F_k^2}{k}, \quad (4.45b)$$

in which the second line results from time discretisation  $T = N\Delta t$ . The subscript  $(\bullet)_i$  indicates that these are losses due to one contact spring  $i$ . The total losses due

to contact springs are obtained as sum of all individual springs which are deformed during contact

$$P_k = \sum_i P_{k,i}. \quad (4.46)$$

It has to be pointed out that these formulations can only give a very rough estimate of the losses due to the contact spring deformation. The contact stiffness is implemented as pure spring-system without a damper element. It is rather superficial to calculate losses for such a system. However, it is believed that in absence of a contact formulation which includes viscoelastic effects, the presented formulation is suitable to estimate at least the order of magnitude of losses due to small-scale deformations during contact. For these estimations a loss factor of  $\eta = 0.3$  was assumed.

## 4.5. Additional remarks on the simulation process

### 4.5.1. Temporal and spatial resolution

For a rolling tyre the temporal and spatial resolutions cannot be arbitrarily chosen. For a rolling speed of  $V$  and circumferential resolution of  $N$  points, the time resolution is given as

$$\Delta t = \frac{\Delta x}{V}, \quad (4.47)$$

where  $\Delta x = \frac{L_{\text{circ}}}{N}$  with  $L_{\text{circ}}$  as tyre circumference. Due to  $f_s = \frac{1}{\Delta t}$  also the sampling frequency  $f_s$  is given. The frequency resolution is determined by  $\Delta f = \frac{1}{n_r N \Delta t}$ , where  $n_r$  is the number of tyre revolutions.  $L_{\text{circ}}$  and  $V$  are determined by the tyre and the operating conditions. This makes it nearly impossible to achieve identical resolutions for two different tyres or speeds.  $N$  remains as an option to influence the time and frequency resolution. Yet, the available range for  $N$  is also limited due to resolution limitations of the WFE tyre model, resolution requirements of the contact model, and available road roughness input data. Often the only possibility is to adjust  $n_r$ .

### 4.5.2. Conversion between Euler and Lagrange reference system

At several stages during the simulation process quantities are transformed from an Euler to a Lagrange reference system<sup>4</sup> and vice versa. This is done by a spatial and temporal reorganisation of the quantity as described in [89, Paper 3]. An

<sup>4</sup>See Appendix A.2 for a description of the differences between these two.

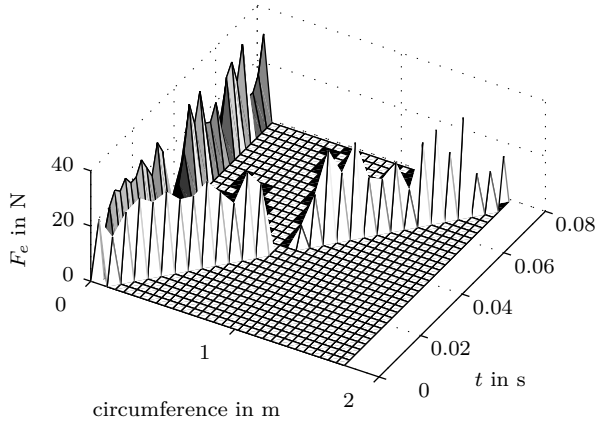


**Fig. 4.12.** Rearranging a contact force from the Euler to the Lagrange system. In the Euler system the contact force acts at a fixed position on the tyre circumference (grey). In the Lagrange system the force is reorganised to move around the circumference over time (white). Note: The actual spatial and temporal resolution in the simulation is 16 times higher than shown here.

example for such a transformation is given in Fig. 4.12 for the case of contact force. Similar transformations are performed for the tyre Green's functions during the contact modelling and the tyre vibrations which serve as input data for the radiation model.

### 4.5.3. Rotational effects

It is undisputed that rotational phenomena like the Doppler shift, centrifugal forces and the Coriolis effect have an influence on the tyre dynamics [56, 114]. This has led to the creation of several tyre models which explicitly include these effects in their system formulations [72, 95, 115]. Despite these efforts, it has not yet been shown that the rotation-induced changes of tyre dynamics actually have a significant influence on sound radiation or rolling losses.

Because of this rotational effects are included in a simplified way in this tyre model. The Doppler shift is, as is shown in [56, 111], already included in the reference system transformation scheme as described in Sec. 4.5.2. Following an approach proposed in [61], the effect of centrifugal forces is modelled as an increase in pretension, see Sec. 5.4. The influence of the Coriolis effect is not included as it is of minor importance for tyre dynamics [114, 116].

#### **4.5.4. Large-deformation non-linearity**

It is a well-known fact that under typical loading conditions tyres exhibit a non-linear behaviour due to large deformations [13]. While the implemented tyre model is capable of capturing the static deformation with the right order of magnitude, see (c) and (d) in Fig. 4.11, it does not account for the non-linearities caused by these deflections.

The most prominent effect caused by these non-linearities is a softening of the sidewall. In [54] it is shown that for a ring-based tyre model differences in sidewall stiffness between a linear and a non-linear sidewall implementation are around 10% for typical tyre loads. Because the actual sidewall geometry is much more accurately represented in the WFE model than in a ring model, it is assumed that in the case of this study these differences are smaller.

As a higher sidewall stiffness decreases rolling resistance [117], it is assumed that rolling losses might be slightly underestimated in this study due to the linear sidewall behaviour. It is not expected that rolling noise is affected much [118].

## 5. Estimation of Material Properties for the WFE tyre model

As with any other advanced simulation tool, the results obtained by WFE tyre modelling are only as good as the input data they are based on. Here, input data mainly refers to the geometry and material properties of the tyre. While the geometry is relatively straightforward to obtain and only subject to slight variations based on the inflation pressure, determination of material properties is very difficult. A tyre is a geometrically complex, inhomogeneous and highly anisotropic laminated structure (cf. Fig. 5.1<sup>1</sup>) consisting of dozens of different materials ranging from rubber to textiles and steel. Bulk material properties are subject to changes with tyre age, temperature or type, or strength and frequency of loading. Additionally, many material properties are yet again modified during the course of the manufacturing process, with the extent of changes being difficult to quantify and somewhat varying for each single tyre. Further, simulation results are likely to be affected by numerical damping, discretisation effects and similar phenomena which require modification of “real” material parameters as countermeasure.

Usually the quality of simulation results will be assessed by comparison with measurements. Leaving aside that effects of measurement uncertainties are often ignored, there are some problems regarding the tuning of simulations to measurements which are particular to tyres. While nearly no two tyres coming from the same production line have exactly the same physical properties, for new tyres this does not lead to significant differences in the dynamic behaviour [68]. Yet, because of the effects mentioned in the previous paragraph, measurements conducted under different conditions or after prolonged ageing (or even wear) might show larger deviations. This can not only be expected for different samples of the same tyre model but even for re-measurements of the same sample. Any optimisation of the material parameters used in the simulations in order to obtain a better fit with measurements is hence strictly speaking unique to the tyre sample and the point in time of the measurement. This should not be taken as an argument against the usefulness of measurements as a means to improve simulation results, it is merely a fact which needs to be taken into consideration.

---

<sup>1</sup>A detailed description of the tyre construction including the functions and properties of the different parts is outside the scope of this text. The reader is instead referred to standard tyre textbooks [13] or information available from the manufacturers [119].

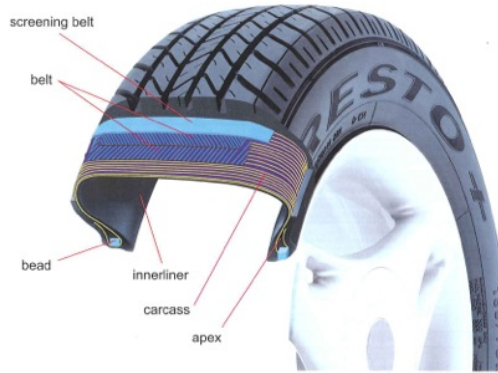


**Fig. 5.1.** Tyre cross section with some of the most important functional parts. Note that the *carcass* is referred to as *ply* in most of this text. Illustration courtesy of Continental Reifen Deutschland GmbH.

The estimation of the tyre material properties for WFE modelling is considered to be a two stage process. Initially, the properties need to be estimated as good as possible based on available data and external factors. This is followed by a further manual or automatic optimisation of properties with regards to particular measurements. Although it is assumed that this second step is always necessary, the quality of data provided after the first step is crucial; if it is good, only slight adjustments might be needed, if it is bad finding suitable values in the optimisation process might be very time-consuming or impossible.

Unfortunately, WFEM's requirements on the material input data can be considered its weak point compared to more classical analytical or FEM based tyre simulation tools. If purely geometric values are left aside, then techniques based on equivalent-structures like beams, plates, rings or shells usually do not require more than 10 to 15 different material parameters (see e.g. [52, 61, 63]). These are usually defined globally for larger portions of the tyre and have to be obtained by what could be described as a condensation process, i.e. a procedure which replaces a complex heterogenous assembly of different materials with an artificial homogeneous material having the combined material properties of the original setup. An example would be replacing a typical liner-ply-rubber tyre sidewall assembly by one artificial "sidewall" material. This process greatly reduces the amount of necessary material parameters. While determination of the condensed properties is generally not easy (as exemplified by the work of O'Boy and Dowling [120, 59], who use a 3D viscoelastic multilayer model of a tyre belt to estimate the input parameters for a bending plate tyre model), the analytical methods benefit from

the low number of needed parameters and the fact that these often can be obtained without the need for too much information about the details of the tyre design, e.g. by measurements. In contrast, fully detailed FEM models usually require tremendous amounts of input data. They often have hundreds or thousand of elements, each with its own material parameters. Yet, each element represents exactly one material with known properties, making condensation procedures unnecessary. Even though some uncertainties still remain because of the previously mentioned deviations due to temperature, load, manufacturing etc., the amount of material parameter tuning needed is manageable.

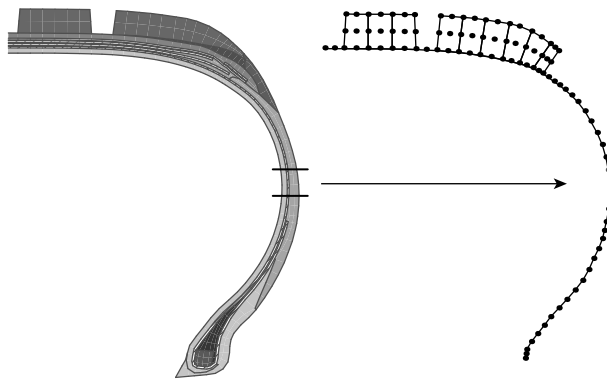


**Fig. 5.2.** Comparison of detailed tyre cross section and WFEM mesh. The marked sidewall area composed of liner, ply and sidewall material layers is represented by a single shell element in the WFEM mesh.

WFEM's property of being a hybrid technique utilising concepts both from analytical as well as FE modelling is very beneficial for both the numerical efficiency and the insight gained into the physical processes. Yet, it also means that WFEM combines the worst aspects of both techniques regarding material input data definition. Much like FEM, it is locally very detailed, i.e. it has a large number of elements, each of which needs its own unique set of input parameters. However, apart from some of the solid elements representing the tread, each element models more than one material section in the original tyre, making a condensation process necessary. A typical WFE tyre model might consist of over 50 shell elements, each representing segments of the tyre consisting of three to eleven layers of highly diverse materials, see Fig. 5.2. In total, for each of these laminar shell elements 21 different elastic stiffness matrix entries, two pretension values, a density and a thickness, and at least one loss-factor need to be determined. Accordingly, a rather advanced condensation procedure is needed to establish the large number



**Fig. 5.3.** The 175/65R 14T XL tyre modelled in this thesis.

of input parameters individually and representatively for each of the elements<sup>2</sup>.

In the following a condensation technique based on a comprehensive dynamic FE model provided by the tyre manufacturer is described. It is based on a procedure suggested by Altena [121] and includes techniques from shell theory and composite materials analysis [122, 123, 124]. The method is applicable to the parts of the tyre being represented by shell elements. The material parameter estimation for solid elements is described in Sec. 5.3.

## 5.1. Available information

The tyre under consideration in this study is a 175/65R 14T XL model with a typical car tyre tread pattern dominated by three circumferential grooves, see Fig. 5.3. The manufacturer provided information about the tyre geometry (including the material sections) and basic material properties. From this, the isotropic bulk properties (i.e. Young's modulus, Poisson's ratio and density) are known for all materials. For composite material sections like belt and ply also the average cord volume fraction and the cord angle are given. Additional information includes temperature and frequency behaviour for rubber materials, modal damping coefficients and the lateral void content ratio for the tread.

---

<sup>2</sup>The same problem arises with less detailed FE models as well.

## 5.2. Condensation of tyre material properties for shell elements

### 5.2.1. Stress-strain relations for individual layers

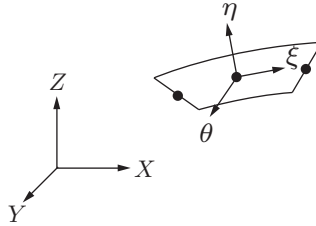


**Fig. 5.4.** Shell element with curvilinear coordinate system  $(\xi, \eta, \theta)$  and global coordinate system  $(X, Y, Z)$ . NOTE: “shell element” refers both to the condensed WFEM shell elements (for which node positions are marked by  $\bullet$ ) as well as the shell-like individual material layers.

For an anisotropic shell as depicted in Fig. 5.4 the engineering stress-strain relations according to classical Kirchhoff-Love shell theory are given as

$$\begin{bmatrix} \sigma_\xi \\ \sigma_\theta \\ \tau_{\xi\theta} \end{bmatrix} = \begin{bmatrix} Q_{11} & Q_{12} & Q_{16} \\ Q_{12} & Q_{22} & Q_{26} \\ Q_{16} & Q_{26} & Q_{66} \end{bmatrix} \begin{bmatrix} \epsilon_\xi \\ \epsilon_\theta \\ \gamma_{\xi\theta} \end{bmatrix}. \quad (5.1)$$

$\sigma_\xi$ ,  $\sigma_\theta$  and  $\epsilon_\xi$ ,  $\epsilon_\theta$  are the in-plane normal stresses and strains,  $\tau_{\xi\theta}$  and  $\gamma_{\xi\theta}$  denote the in-plane shear stress and strain and  $Q_{ij}$  are the entries of the reduced stiffness matrix connecting stresses and strains. Eq. (5.1) is also valid for any of the individual material layers constituting the tyre laminate.

The determination of the  $Q_{ij}$  values is dependent on the material characteristics for the specific layer. Large parts of the tyre, i.e. all rubber material, can be classified as homogeneous and isotropic. Yet, for example the belt and ply parts, which constitute the core of the tyre, are fibrous composites, i.e. they consist of (steel or textile) fibres (also called cords) embedded in a (rubber) matrix. Each of these composite layers is heterogeneous and, depending on the angle between the cords and the tyre coordinate system, either orthotropic or completely anisotropic. Procedures for obtaining  $Q_{ij}$  for both of the material groups are described in the following.

### Isotropic layers

For the homogenous and isotropic rubber layers in the tyre, (5.1) reduces to

$$\begin{bmatrix} \sigma_\xi \\ \sigma_\theta \\ \tau_{\xi\theta} \end{bmatrix} = \begin{bmatrix} Q_{11} & Q_{12} & 0 \\ Q_{12} & Q_{22} & 0 \\ 0 & 0 & Q_{66} \end{bmatrix} \begin{bmatrix} \epsilon_\xi \\ \epsilon_\theta \\ \gamma_{\xi\theta} \end{bmatrix}, \quad (5.2)$$

where

$$Q_{11} = Q_{22} = \frac{E}{1 - \nu^2} \quad (5.3a)$$

$$Q_{12} = \frac{\nu E}{1 - \nu^2} \quad (5.3b)$$

$$Q_{66} = \frac{E}{2(1 + \nu)}. \quad (5.3c)$$

$E$  and  $\nu$  are the material's Young's modulus and Poisson's ratio. Due to the isotropic properties, there is no coupling between in-plane strain and shear, i.e.  $Q_{16} = Q_{26} = 0$ .

### Composite layers

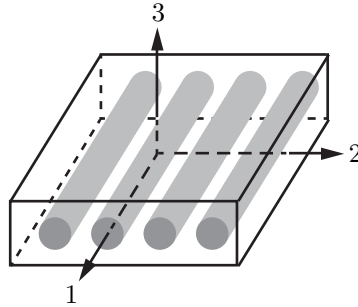


**Fig. 5.5.** A fibrous composite layer with its local (1, 2, 3)-coordinate system.

The determination of the stress-strain relations for composite layers as shown in Fig. 5.5 is a multi-step procedure. First and foremost, the relationship of the composite's "apparent" material properties to the cord and matrix properties needs to be established. The two constituting materials in a fibrous composite usually exhibit highly different properties (as exemplified by the combinations of steel or

textile cords embedded in a rubber matrix being typical for tyres). Which of them is dominating the composite's behaviour can vary with direction or type of load. A widely used procedure to determine the properties of the fibrous composite is the *mechanics of materials* approach [124, Cha. 3.2]. It assumes that the constituting materials are homogeneous and isotropic. The properties are calculated in a layer-specific, local coordinate system (cf. Fig. 5.5), where the 1-axis is along the cord direction, the 2-axis is the in-plane normal to the cord direction and the 3-axis is the out of plane direction. This establishes the composite layer as an orthotropic material with principal axes coinciding with the (123)-axes. The Young's modulus in the cord direction,  $E_1$ , and the Poisson's ratio  $\nu_{12}$  can then be directly estimated using the *rule of mixtures*:

$$E_1 = E_c V_{f,c} + E_m V_{f,m} \quad (5.4)$$

$$\nu_{12} = \nu_c V_{f,c} + \nu V_{f,m}. \quad (5.5)$$

Herein,  $E_c$  ( $\nu_c$ ) and  $E_m$  ( $\nu_m$ ) are the Young's moduli (Poisson's ratios) of the cord and the matrix material, and  $V_{f,c}$  and  $V_{f,m}$  are the volume fraction of cords respectively the rubber matrix in the composite:

$$V_{f,c} = \frac{vol_c}{vol_c + vol_m} \quad (5.6)$$

$$V_{f,m} = 1 - V_{f,c}, \quad (5.7)$$

where  $vol_c$  and  $vol_m$  are the volumes of the cords and the matrix.

Several techniques exist for the approximation of the composite's characteristics in the 2-direction. One of these techniques are the *Halpin-Tsai equations* [124], which are remarkably simple, yet have proven to be quite accurate:

$$E_2 = E_m \frac{1 + \zeta \alpha V_{f,c}}{1 - \alpha V_{f,c}} \quad (5.8)$$

$$G_{12} = G_m \frac{1 + \zeta \beta V_{f,c}}{1 - \beta V_{f,c}}, \quad (5.9)$$

where

$$\alpha = \frac{E_c/E_m - 1}{E_c/E_m + \zeta} \quad (5.10)$$

$$\beta = \frac{G_c/G_m - 1}{G_c/G_m + \zeta}. \quad (5.11)$$

$G_{12}$  is shear modulus in the 12-plane and  $G_c$  and  $G_m$  are the isotropic shear stiffnesses of the cord and matrix materials, given as

$$G_i = \frac{E_i}{2(1 + \nu_i)} \quad \text{for } i = c, m. \quad (5.12)$$

The parameter  $\zeta$  is a measure of the influence of the fibre reinforcement on the composite material and depends for example on fibre and packing geometry and boundary conditions. It can either be determined from measurements or be approximated as

$$\zeta = \begin{cases} 2 + 40 \cdot V_{f,c}^{10}, & \text{for } E_2, \\ 1 + 40 \cdot V_{f,c}^{10}, & \text{for } G_{12}. \end{cases} \quad (5.13a)$$

Finally, the still missing Poisson's ratio  $\nu_{21}$  is given by reciprocity as

$$\nu_{21} = \frac{\nu_{12} E_2}{E_1}. \quad (5.14)$$

Using Equations (5.4) to (5.14) an expression for the stress-strain relations of the orthotropic fibrous composite in the local (1, 2, 3)-coordinate system can be obtained as

$$\begin{bmatrix} \sigma_1 \\ \sigma_2 \\ \tau_{12} \end{bmatrix} = \begin{bmatrix} Q_{11} & Q_{12} & 0 \\ Q_{12} & Q_{22} & 0 \\ 0 & 0 & Q_{66} \end{bmatrix} \begin{bmatrix} \epsilon_1 \\ \epsilon_2 \\ \gamma_{12} \end{bmatrix}, \quad (5.15)$$

where

$$Q_{11} = \frac{E_1}{1 - \nu_{12}\nu_{21}} \quad (5.16a)$$

$$Q_{22} = \frac{E_2}{1 - \nu_{12}\nu_{21}} \quad (5.16b)$$

$$Q_{12} = \frac{E_2\nu_{12}}{1 - \nu_{12}\nu_{21}} = \frac{E_1\nu_{21}}{1 - \nu_{12}\nu_{21}} \quad (5.16c)$$

$$Q_{66} = G_{12}. \quad (5.16d)$$

Because the local (1, 2, 3)-coordinate system aligns with the material's principal axes of orthogonality, there is — similar to the isotropic case in (5.2) — still no coupling between in-plane strain and shear. For a fibrous composite which is rotated by an angle  $\phi$  with respect to a global coordinate system as shown in Fig. 5.6, the stress-strain relations in the global coordinate system can be obtained

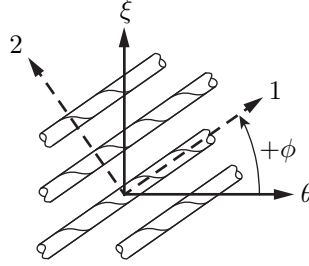


**Fig. 5.6.** Definition of rotation direction between principal material axes of the fibrous composite and the curvilinear WFEM shell coordinates.

by a coordinate transformation procedure as e.g. described in [124, Cha. 2]. The final result is

$$\begin{bmatrix} \sigma_\xi \\ \sigma_\theta \\ \tau_{\xi\theta} \end{bmatrix} = \begin{bmatrix} \bar{Q}_{11} & \bar{Q}_{12} & \bar{Q}_{16} \\ \bar{Q}_{12} & \bar{Q}_{22} & \bar{Q}_{26} \\ \bar{Q}_{16} & \bar{Q}_{26} & \bar{Q}_{66} \end{bmatrix} \begin{bmatrix} \epsilon_\xi \\ \epsilon_\theta \\ \gamma_{\xi\theta} \end{bmatrix}, \quad (5.17)$$

where

$$\bar{Q}_{11} = Q_{11} c^4 + 2(Q_{12} + 2Q_{66}) c^2 s^2 + Q_{22} s^4 \quad (5.18a)$$

$$\bar{Q}_{12} = (Q_{11} + Q_{22} - 4Q_{66}) c^2 s^2 + Q_{12}(c^4 + s^4) \quad (5.18b)$$

$$\bar{Q}_{16} = (Q_{11} - Q_{12} - 2Q_{66}) c^3 s + (Q_{12} - Q_{22} + 2Q_{66}) c s^3 \quad (5.18c)$$

$$\bar{Q}_{22} = Q_{11} s^4 + 2(Q_{12} + 2Q_{66}) c^2 s^2 + Q_{22} c^4 \quad (5.18d)$$

$$\bar{Q}_{26} = (Q_{11} - Q_{12} - 2Q_{66}) s^3 c + (Q_{12} - Q_{22} + 2Q_{66}) c^3 s \quad (5.18e)$$

$$\bar{Q}_{66} = (Q_{11} + Q_{22} - 2Q_{12} - 2Q_{66}) c^2 s^2 + Q_{66}(c^4 + s^4) \quad (5.18f)$$

and

$$c = \cos \phi \quad (5.19a)$$

$$s = \sin \phi. \quad (5.19b)$$

The terms  $\bar{Q}_{16}$  and  $\bar{Q}_{26}$  vanish for  $\phi = n\pi/2$ ,  $n = 0, 1, 2, \dots$ , implying that the composite is orthotropic with respect to the global coordinate system. For all other  $\phi$  the composite is anisotropic with coupling of in-plane stress and shear. This is for example the case for the nowadays almost exclusively used radial tyres,

where the placing of the steel cords in the belt at a certain diagonal angle to the tread centreline is a crucial design property to increase strength and stability. As a consequence, the fibrous belt composite is anisotropic with regards to the tyre coordinate system. Then again, the ply cords are laid at  $90^\circ$  to the centreline, implying that the ply composite remains orthotropic<sup>3</sup>.

### 5.2.2. Force and moment resultants for laminates

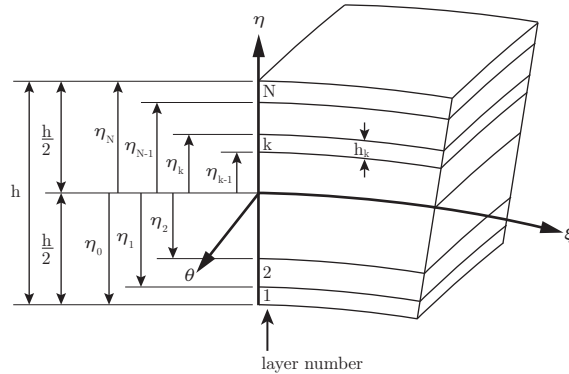


**Fig. 5.7.** Laminated shell element.

With Equations (5.2) and (5.17) the stress-strain relations for individual isotropic or composite material layers have been determined. However, most elements used in the WFE analysis are laminates consisting of multiple layers of different material groups, as is exemplified in Figures 5.2 and 5.7. The combined macromechanical behaviour of such an laminate can be expressed using *classical lamination theory*. In this theory, the complex, 3-dimensional elasticity problem involving the whole laminate domain is reduced to expressions for the resulting laminate middle-surface membrane strains and bending curvatures. Presuming that the resulting shell obeys classical Kirchhoff-Love theory, there is only a linear variation of strain across the shell thickness, i.e.

$$\begin{bmatrix} \epsilon_\xi \\ \epsilon_\theta \\ \gamma_{\xi\theta} \end{bmatrix} = \begin{bmatrix} \epsilon_\xi^0 \\ \epsilon_\theta^0 \\ \gamma_{\xi\theta}^0 \end{bmatrix} + \eta \begin{bmatrix} \kappa_\xi \\ \kappa_\theta \\ \kappa_{\xi\theta} \end{bmatrix}, \quad (5.20)$$

<sup>3</sup>It shall be added that for the less common diagonal bias and belted bias tyre types the ply cords are also laid diagonally to the centreline, giving them anisotropic material behaviour with respect to the tyre coordinate system.

where  $[\epsilon_\xi^0, \epsilon_\theta^0, \gamma_{\xi\theta}^0]^T$  denote the strains at the shell middle-surface and  $[\kappa_\xi, \kappa_\theta, \kappa_{\xi\theta}]^T$  the middle-surface curvatures. By inserting (5.20) in (5.2) or (5.17) the stresses in the  $k$ th layer can be related to the shell middle-surface strains and curvatures as

$$\begin{bmatrix} \sigma_\xi \\ \sigma_\theta \\ \tau_{\xi\theta} \end{bmatrix}_k = \begin{bmatrix} \bar{Q}_{11} & \bar{Q}_{12} & \bar{Q}_{16} \\ \bar{Q}_{12} & \bar{Q}_{22} & \bar{Q}_{26} \\ \bar{Q}_{16} & \bar{Q}_{26} & \bar{Q}_{66} \end{bmatrix}_k \cdot \left[ \begin{bmatrix} \epsilon_\xi^0 \\ \epsilon_\theta^0 \\ \gamma_{\xi\theta}^0 \end{bmatrix} + \eta \begin{bmatrix} \kappa_\xi \\ \kappa_\theta \\ \kappa_{\xi\theta} \end{bmatrix} \right]. \quad (5.21)$$

The resultant normal forces per unit width,  $N$ , and moments per unit width,  $M$ , which act on the shell middle-surface, can be obtained by summing up the integrals of the layer stresses over the layer thicknesses as follows

$$\begin{bmatrix} N_\xi \\ N_\theta \\ N_{\xi\theta} \end{bmatrix} = \int_{-h/2}^{h/2} \begin{bmatrix} \sigma_\xi \\ \sigma_\theta \\ \tau_{\xi\theta} \end{bmatrix} d\eta = \sum_{k=1}^N \int_{\eta_{k-1}}^{\eta_k} \begin{bmatrix} \sigma_\xi \\ \sigma_\theta \\ \tau_{\xi\theta} \end{bmatrix}_k d\eta \quad (5.22)$$

and

$$\begin{bmatrix} M_\xi \\ M_\theta \\ M_{\xi\theta} \end{bmatrix} = \int_{-h/2}^{h/2} \begin{bmatrix} \sigma_\xi \\ \sigma_\theta \\ \tau_{\xi\theta} \end{bmatrix} \eta d\eta = \sum_{k=1}^N \int_{\eta_{k-1}}^{\eta_k} \begin{bmatrix} \sigma_\xi \\ \sigma_\theta \\ \tau_{\xi\theta} \end{bmatrix}_k \eta d\eta. \quad (5.23)$$

Herein,  $h$  is the thickness of the laminate shell and the  $\eta_k$  denote the directed distance from the middle-surface to the top of the  $k$ th layer as shown in Fig. 5.7. For the thickness of a layer it is thus  $h_k = \eta_k - \eta_{k-1}$ . By inserting (5.21) into (5.22) and (5.23), and using the fact that the  $(\bar{Q}_{ij})_k$  are constant within a layer, the forces and moments can be written in a combined matrix form as (see [124, Cha. 4] for details)

$$\begin{bmatrix} \hat{\mathbf{N}} \\ \hat{\mathbf{M}} \end{bmatrix} = \begin{bmatrix} \mathbf{P} & \mathbf{PQ} \\ \mathbf{PQ} & \mathbf{Q} \end{bmatrix} \begin{bmatrix} \boldsymbol{\epsilon} \\ \boldsymbol{\kappa} \end{bmatrix} \quad (5.24)$$

where

$$\hat{\mathbf{N}} = [N_\xi \quad N_\theta \quad N_{\xi\theta}]^T \quad (5.25a)$$

$$\hat{\mathbf{M}} = [M_\xi \quad M_\theta \quad M_{\xi\theta}]^T \quad (5.25b)$$

$$\boldsymbol{\epsilon} = [\epsilon_\xi^0 \quad \epsilon_\theta^0 \quad \gamma_{\xi\theta}^0]^T \quad (5.25c)$$

$$\boldsymbol{\kappa} = [\kappa_\xi \quad \kappa_\theta \quad \tau_{\xi\theta}]^T \quad (5.25d)$$

and

$$\mathbf{P} = \begin{bmatrix} P_{11} & P_{12} & P_{16} \\ P_{12} & P_{22} & P_{26} \\ P_{16} & P_{26} & P_{66} \end{bmatrix} \quad (5.26a)$$

$$\mathbf{PQ} = \begin{bmatrix} PQ_{11} & PQ_{12} & PQ_{16} \\ PQ_{12} & PQ_{22} & PQ_{26} \\ PQ_{16} & PQ_{26} & PQ_{66} \end{bmatrix} \quad (5.26b)$$

$$\mathbf{Q} = \begin{bmatrix} Q_{11} & Q_{12} & Q_{16} \\ Q_{12} & Q_{22} & Q_{26} \\ Q_{16} & Q_{26} & Q_{66} \end{bmatrix} \quad (5.26c)$$

with

$$P_{ij} = \sum_{k=1}^N (\bar{Q}_{ij})_k (\eta_k - \eta_{k-1}) \quad (5.27a)$$

$$PQ_{ij} = \frac{1}{2} \sum_{k=1}^N (\bar{Q}_{ij})_k (\eta_k^2 - \eta_{k-1}^2) \quad (5.27b)$$

$$Q_{ij} = \frac{1}{3} \sum_{k=1}^N (\bar{Q}_{ij})_k (\eta_k^3 - \eta_{k-1}^3). \quad (5.27c)$$

Herein,  $\mathbf{P}$  and  $\mathbf{Q}$  are extensional and bending stiffness matrices while  $\mathbf{PQ}$  is a stiffness matrix coupling normal forces with bending curvatures (and vice-versa, bending moments with in-plane strains). For a laminate,  $\mathbf{PQ}$  vanishes only under very special conditions. For many other examples often the assumption is made that extension and bending are independent of each other. This does not hold at large in this case.

### 5.2.3. Transverse shear

No assumptions have so far been made about transverse shear across the element thickness. In a manner similar to (5.24) it can be expressed in terms of resultant middle-surface transverse forces as

$$\hat{\mathbf{T}} = \mathbf{G}\boldsymbol{\gamma} \quad (5.28)$$

where

$$\hat{\mathbf{T}} = [T_{\xi\eta} \quad T_{\theta\eta}]^T \quad (5.29a)$$

$$\boldsymbol{\gamma} = [\gamma_{\xi\eta} \quad \gamma_{\theta\eta}]^T \quad (5.29b)$$

and

$$\mathbf{G} = \begin{bmatrix} G_{11} & G_{12} \\ G_{12} & G_{22} \end{bmatrix}. \quad (5.30)$$

As a first simplification it is assumed that there is no coupling between shear in the  $\xi$  and  $\theta$  directions, i.e.  $G_{12} = 0$ . In [125, Cha. 15] a deep shell approximation for the remaining terms is given as

$$G_{11} = G_{22} = \frac{1}{6}(P_{11} + P_{22}) + \frac{1}{3}P_{33}. \quad (5.31)$$

In [126] better agreement with measurements is instead obtained by using

$$G_{11} = \frac{1}{4}(P_{11} + 2P_{33}) \quad (5.32a)$$

$$G_{22} = \frac{1}{4}(P_{22} + 2P_{33}). \quad (5.32b)$$

Pre-studies have shown that the differences between simulations using (5.31) or (5.32) are marginal, but for frequencies above 1.3 kHz slightly better match to measurements is obtained from (5.32).

#### 5.2.4. Determination of the elastic stiffness matrix for a shell element

By combining (5.24) with (5.28) all resulting forces and moments for the laminate are obtained as

$$\begin{bmatrix} \hat{\mathbf{N}} \\ \hat{\mathbf{M}} \\ \hat{\mathbf{T}} \end{bmatrix} = \begin{bmatrix} \mathbf{P} & \mathbf{PQ} & \mathbf{0} \\ \mathbf{PQ} & \mathbf{Q} & \mathbf{0} \\ \mathbf{0} & \mathbf{0} & \mathbf{G} \end{bmatrix} \begin{bmatrix} \boldsymbol{\epsilon} \\ \boldsymbol{\kappa} \\ \boldsymbol{\gamma} \end{bmatrix}, \quad (5.33)$$

where  $\mathbf{0}$  are zero matrices of appropriate size.

By comparison of (5.33) with the formulation of the WFEM shell element given in [75], the elastic stiffness matrix  $\mathbf{D}_{\text{shell}}$  of the shell element can be identified as

$$\mathbf{D}_{\text{shell}} = \begin{bmatrix} \mathbf{P} & \mathbf{PQ} & \mathbf{0} \\ \mathbf{PQ} & \mathbf{Q} & \mathbf{0} \\ \mathbf{0} & \mathbf{0} & \mathbf{G} \end{bmatrix}. \quad (5.34)$$

### 5.3. Stiffness parameters for solid elements

The tread area differs from the other sections of the tyre by two important properties. Firstly, as already pointed out in Sec. 4.1.3, it is not modelled by shell elements but by solid elements. Secondly, it solely consists of one layer of homogeneous, isotropic rubber material, which considerably simplifies the determination of the elastic stiffness matrix  $\mathbf{D}_{\text{sol}}$ . Indeed,  $\mathbf{D}_{\text{sol}}$  simply follows from the engineering stress-strain relations for isotropic solids [127, Cha. 2]

$$\boldsymbol{\sigma}_{\text{sol}} = \mathbf{D}_{\text{sol}} \boldsymbol{\epsilon}_{\text{sol}} \quad (5.35)$$

as

$$\mathbf{D}_{\text{sol}} = \frac{E}{(1+\nu)(1-2\nu)} \begin{bmatrix} 1-\nu & \nu & \nu & 0 & 0 & 0 \\ \nu & 1-\nu & \nu & 0 & 0 & 0 \\ \nu & \nu & 1-\nu & 0 & 0 & 0 \\ 0 & 0 & 0 & \frac{1-2\nu}{2} & 0 & 0 \\ 0 & 0 & 0 & 0 & \frac{1-2\nu}{2} & 0 \\ 0 & 0 & 0 & 0 & 0 & \frac{1-2\nu}{2} \end{bmatrix}, \quad (5.36)$$

where  $E$  and  $\nu$  are the material's Young's modulus and Poisson's ratio. Moreover, in (5.35) the stress and strain vector are defined as

$$\boldsymbol{\sigma}_{\text{sol}} = [\sigma_{\xi} \quad \sigma_{\eta} \quad \sigma_{\theta} \quad \tau_{\xi\eta} \quad \tau_{\xi\theta} \quad \tau_{\eta\theta}]^T \quad (5.37a)$$

$$\boldsymbol{\epsilon}_{\text{sol}} = [\epsilon_{\xi} \quad \epsilon_{\eta} \quad \epsilon_{\theta} \quad \gamma_{\xi\eta} \quad \gamma_{\xi\theta} \quad \gamma_{\eta\theta}]^T. \quad (5.37b)$$

Herein, the extensional stresses and strains are given by the  $\sigma_i$  and  $\epsilon_i$ , the  $\tau_{ij}$  and  $\gamma_{ij}$  are the shear stresses and strains and the coordinate system is defined by Fig. 5.8.

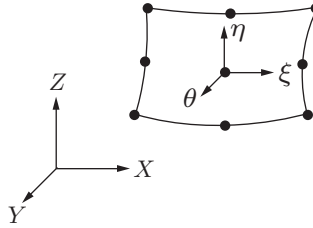


**Fig. 5.8.** Solid element with curvilinear coordinate system  $(\xi, \eta, \theta)$  and global coordinate system  $(X, Y, Z)$ . Node positions marked by  $\bullet$ .

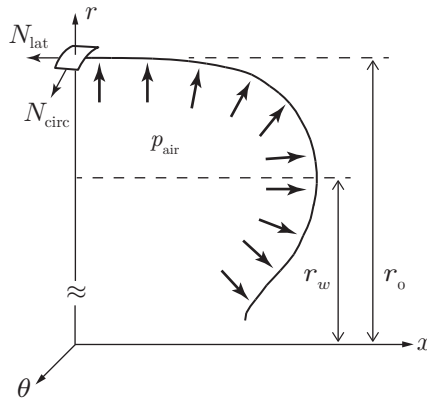


**Fig. 5.9.** Tyre cross section geometry for pretension calculations.

## 5.4. Pretension

The pretension of the ply and belt cords caused by the manufacturing process and the inflation pressure considerably influences the dynamic behaviour of the tyre. As it is extremely difficult to measure pretension in the cured tyre, no useful pretension data could be provided by the tyre manufacturer. Even so, estimations of the pretension in lateral and circumferential direction are possible by treating the tyre as a doubly curved membrane surface as shown in Fig. 5.9. Force equilibrium considerations [13, Cha. 6]<sup>4</sup> then give the lateral and circumferential pretensions for the tread centreline as

<sup>4</sup>Note the typo in the original formulation of (5.39) in [13].

$$N_{\text{lat}} = \frac{p_{\text{air}}}{2r_0} (r_0^2 - r_w^2) \quad (5.38)$$

$$N_{\text{circ}} = R_\theta \left( p_{\text{air}} - \frac{N_{\text{lat}}}{R_\xi} \right). \quad (5.39)$$

$p_{\text{air}}$  is the air pressure in the tyre cavity,  $r_0$  the radius at the tyre centreline and  $r_w$  the radius at the widest point of the tyre cross section. The radii of curvature in lateral and circumferential direction,  $R_\xi$  and  $R_\theta$ , are given as

$$R_\xi = \left| r \frac{(1 + x'^2)^{\frac{1}{2}}}{x'} \right| \quad (5.40a)$$

$$R_\theta = \left| \frac{(1 + x'^2)^{\frac{3}{2}}}{x''} \right|, \quad (5.40b)$$

with

$$x' = \frac{dx}{dr}, \quad x'' = \frac{d^2x}{dr^2}. \quad (5.41)$$

As the ply cords run perpendicular to the tread centreline they cannot support circumferential pretension. Hence,  $R_\theta$  is only non-zero for the shoulder and crown areas of the tyre containing belt cords. It seems reasonable to estimate the variation in  $N_{\text{circ}}$  for these areas by varying  $x, r$  in (5.40). The determination of values for  $N_{\text{lat}}$  outside the tread centreline is not as straightforward, especially for the sidewall areas of the tyre [13]. In [35, Paper B] an estimation of the lateral pretension at a point  $(x, r)$  on the tyre cross section is given as

$$N_{\text{lat}}(x, r) = N_{\text{lat}} \frac{r_0}{r}. \quad (5.42)$$

Owing to the lack of better alternatives, this is taken as a basis for estimation of the lateral pretension distribution.

Equations (5.38) and (5.39) are based on static equilibrium considerations, for a rotating tyre there is an additional contribution from the centrifugal force to the circumferential pretension which is given as [61]

$$N_{\text{circ}, \Omega} = \mu \Omega^2 r_0^2. \quad (5.43)$$

Herein,  $\Omega$  is the angular velocity of the tyre and  $\mu$  is the belt's mass per unit area. The effective circumferential pretension is finally given by the sum of  $N_{\text{circ}}$  and  $N_{\text{circ}, \Omega}$ .

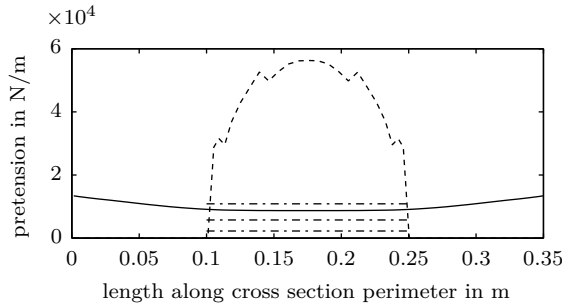


**Fig. 5.10.** Lateral (—) and circumferential (---) pretension along the tyre cross section. (---) is the additional centrifugal component for the circumferential pretension for 50 km/h (bottom), 80 km/h (middle), and 110 km/h (top).

The pretension estimations resulting from Equations (5.39), (5.42), and (5.43) are shown in Fig. 5.10. Even for 110 km/h the contribution from the centrifugal force is less than 20% of the circumferential pretension due to the tyre inflation.

## 5.5. Damping properties

The frequency- and temperature-dependent viscoelastic properties of the different material sections have been provided by the manufacturer. However, damping properties are based on measurements instead. There are two reasons for this: firstly, it was not possible to develop a scheme which condensed the loss factor data in a similar way as it is done for stiffness in Sec. 5.2. Secondly, even after successful condensation, the estimated loss factors would give non-proportional damping. This is, as was pointed out in Sec. 4.1.2, incompatible with the modal summation approach used for obtaining the forced response of the tyre.

Instead, frequency-dependent proportional damping based on measurement data is implemented. From half-power bandwidth evaluations of the first five resonance peaks in the measured input mobility (see Appendix C) the loss factor for low frequencies is initially estimated as 0.055. Additionally modal damping data is available for the frequency range up to 500 Hz. Following the procedure outlined in [77], the loss factor for higher frequencies, where the deformation of the highly damped tread material becomes more significant, is set to 0.15. After a further adjustment to give better match between measured and simulated mobilities, the loss factor is obtained as

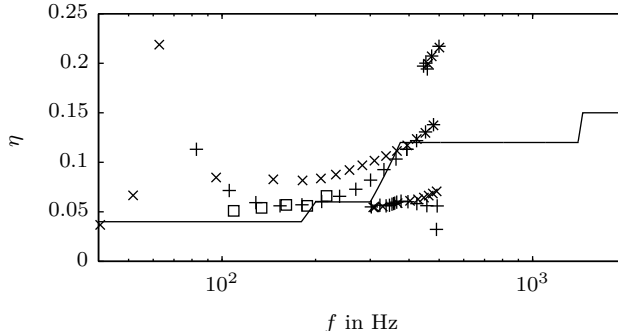


**Fig. 5.11.** Loss factor data as obtained from the half-power bandwidth method ( $\square$ ), as obtained as modal damping for modes with  $m = \{2, 4, 6\}$  ( $\times$ ), or  $m = \{3, 5\}$  ( $+$ ) half wave lengths over the cross-section, and as used in WFEM ( $-$ ).

$$\eta(f) = \begin{cases} 0.04, & 0 \text{ Hz} < f \leq 180 \text{ Hz} \\ 0.06, & 200 \text{ Hz} \leq f \leq 300 \text{ Hz} \\ 0.12, & 375 \text{ Hz} \leq f \leq 1400 \text{ Hz} \\ 0.15, & 1450 \text{ Hz} \leq f, \end{cases} \quad (5.44)$$

where frequency gaps are linearly filled as shown in Fig. 5.11.

## 5.6. Additional implementation considerations

The WFEM mesh is directly based on the tyre geometry as provided by the manufacturer. The shell elements are as far as reasonable placed in accordance with the neutral layer of the laminate they correspond to. According to [121] and with reference to Fig. 5.7 the position of the neutral layer of a laminate is given as

$$\eta_{nl} = - \frac{\sum_{k=1}^N (\bar{Q}_{ii})_k h_k \cdot \left( \sum_{l=0}^{k-1} h_l + \frac{h_k}{2} \right)}{\sum_{k=1}^N (\bar{Q}_{ii})_k h_k}. \quad (5.45)$$

Herein,  $h_0 = 0$  and  $i = 1, 2$ , i.e. the position of the neutral layer might be different in the  $\xi$ - and  $\theta$ -directions. In this case the average of both is used. As expected, most shell elements align with the ply or belt layers dominating the elasticity of the tyre. For the determination of the force and moment resultants in Sec. 5.2.2,

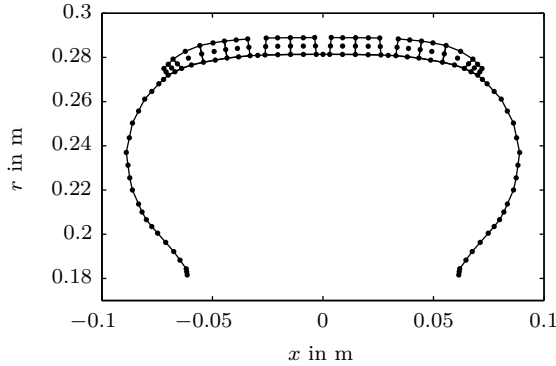


**Fig. 5.12.** WFEM mesh of the tyre cross section. Nodes marked by ●.

$\eta_{ml}$  is not relevant as the used *classical lamination theory* is based on the laminate mid-surface and not the neutral layer.

Because the shell elements have no geometric extension in the  $\eta$ -direction (the thickness is a material property for shells), the geometry of the solid elements modelling the tread layer has to be adjusted to keep shell and solid elements connected in the WFE model. In order to change to size of the solid elements as little as possible, the tread layer is moved down half the shell element thickness. Circumferential grooves are modelled by removal of solid elements from the tread layer. The resulting mesh is shown in Fig. 5.12.

The lateral tread voids cannot be included geometrically in the WFE model. However, for each solid the average lateral void volume over the circumference is known. The density and Young's modulus of the solid elements are adjusted in proportion to the fraction of remaining rubber.

Dynamic Young's moduli are given by the manufacturer for 20°C and 55°C, which are typical temperatures for mobility measurements and real rolling conditions. As no mobility measurements are available for the 55°C case, it is not possible to validate the condensation results or the obtain loss factor data. Due to this, material values for 20°C are taken as basis also for rolling simulations. Some calculations for 55°C are presented in Sec. 6.3.1, though. The frequency dependence of the dynamic properties is ignored, instead the values at 200 Hz are taken for all frequencies.

The material data derived by the condensation procedure gives good initial match between simulated and measured mobilities as shown in Appendix C.2. Even better match is achieved by further adjustment of the material parameters. This is done by a combination of an optimisation procedure based on a genetic

algorithm, see Appendix B, and some further manual adjustments. As a result, shell stiffness terms and the circular pretension are reduced by about 20%. Based on the provided density data, the tyre model was also too heavy compared to the tyre sample used for the measurements. The density of all elements was reduced by 6% to account for this.

## 5.7. Validation

In Appendix C measured and calculated mobilities are compared for 25 different positions on the tyre. The mobilities obtained for optimised material values show in general good agreement with the measurements. Problematic is the region of the cut-on of first and second cross-sectional modes around 300 Hz to 600 Hz in the input mobility, Fig. C.4c, where the peak is broader than in the measurements. Some deviations in this frequency region are also visible in the transfer mobilities for positions A to E and angles greater than 0°. Positions B and E also show some underestimation of mobilities above approximately 700 Hz for 135° and 180°. In spite of this, the dynamic response seems to be modelled quite accurately for points on the tread.

Results above 500 Hz show no good agreement with measurements for position A at all angles. This might indicate some problems with the modelling of the sidewall behaviour and/or lateral wave motion on the tyre. The second assumption is consolidated by the behaviour of points B and E for 0°, Figures C.4b and C.4e. These points show more pronounced high frequency deviations than the same cross-sectional positions at other angles. For 0° the high frequency response at these points is purely determined by lateral wave propagation. For all other angles, in contrast, circumferential wave propagation is dominant, which seems to be better captured by the model than lateral wave propagation.

# 6. Simulation results

In the following the results for rolling noise and rolling resistance simulations are presented. In Sec. 6.1 this is first done for an initial tyre configuration which is based on material data which was derived using the procedure described in Cha. 5. The influence of operating conditions, tyre properties and modelling parameters on the simulations are evaluated in Sections 6.2 to 6.4.

It has to be stressed that the initial configuration shall in no way be seen as the correct model of the tyre. It is merely a representation of one possible outcome of the condensation procedure and the following optimisation. Its only merit is that it happens to give more or less good match between simulated and measured mobilities for a limited selection of points on the tyre.

## 6.1. Initial tyre configuration

### 6.1.1. Setup

Initial rolling loss and rolling noise simulations for the 175/65 R14 tyre are based on the WFEM mesh and tyre material parameters as described in Sec. 5.6. In circumferential direction the tyre is discretised into 512 equidistant segments. The forced response is calculated using  $\pm 250$  wave orders in circumferential direction and the first 100 cross-sectional modes. For the BEM calculations these numbers reduce to  $\pm 24$  and 20, which is sufficient for the intended frequency range as could be shown in a pre-study. The additional pretension component due to rotational stiffening,  $N_{\text{circ},\Omega}$ , is taken into account. Tyre material values are based on manufacturer data for 20°C.

The inflation pressure is 200 kPa and tyre load is set to 2820 N; a value derived from a typical car weight for this tyre size. The rolling speed is 80 km/h.

Rolling is simulated over the length of at least seven revolutions, the first two of which are used to load the tyre in accordance with the static load. The following two revolutions are needed for the decay of loading-induced vibrations. Revolutions five and six are finally used for the simulations. The road surface is based on a scan of a drum-mounted ISO replica road surface [128]. The length of the scan corresponds to nine full tyre revolutions. The segment for revolution one is shown in Fig. 6.1. In [78] a contact stiffness of  $5 \cdot 10^4$  N/m was estimated for this road profile. The same value is used here.

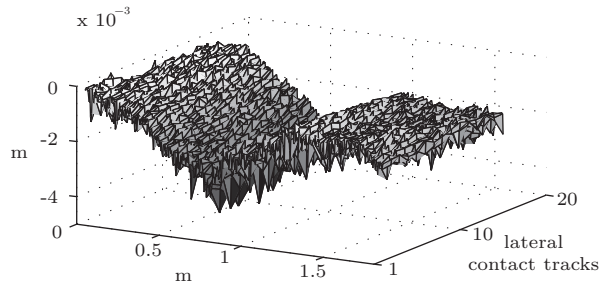


**Fig. 6.1.** The first segment of the ISO road profile. Note the differences in axis scaling.

Pre-studies showed that it is not necessary to include the lateral voids in the tyre geometry during tyre/road contact simulations<sup>1</sup>. In the circumferential voids no contact is possible, hence twelve lateral contact tracks corresponding to the twelve solid elements of the WFE model are used.

BEM calculations are based on a deformed mesh including the circumferential voids as shown in Figures 4.10 and 4.11. The mesh is lifted by 1 mm to avoid numerical problems in the contact zone. The radiation is evaluated as mean sound pressure at 321 points on a half-sphere of radius 1 m around the contact point between tyre and road. A total A-rated sound pressure level is calculated for third-octave bands from 100 Hz to 2500 Hz.

Based on the circumferential tyre resolution, the number of evaluated revolutions and the rolling speed a frequency resolution of 6 Hz is obtained (cf. Sec. 4.5.1).

### 6.1.2. Rolling noise

A simulated third-octave band rolling noise spectrum is shown in Fig. 6.2. The total A-rated sound pressure level  $L_{p,A,tot}$  is 91.1 dB. Validation of the results is difficult as no sound pressure measurements exist for the simulated tyre. For comparison reasons sound pressure levels from a measurement of 205/55 R16 tyre with circumferential grooves (“airplane tyre”) are also shown in Fig. 6.2. The tyre was rolling on a test drum with exactly the same surface roughness as is used in the simulations. Static loading was 3000 N. The measured sound pressure level is the mean value over three microphone positions. All three positions are 0.35 m above ground and 1 m from the tyre centre. Two positions are in the plane of the tyre at the leading and trailing edge, one position is perpendicular to the tyre

<sup>1</sup>This cannot be generalised: for tyres with other tread patterns or for other road surfaces the lateral voids might need to be included in the contact simulation.

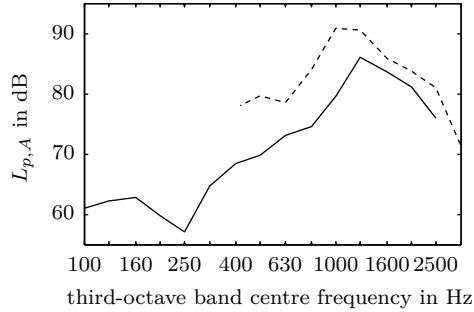


**Fig. 6.2.** Simulated (—) sound pressure levels for the initial configuration. Also shown are measurement results (---) for a similar, but not identical tyre (see the comments in the text).

plane. Results below 400 Hz cannot be used because of background noise. For the simulated sound pressure levels only points above a height of 0.35 m are evaluated.

The simulation underestimates the measured third-octave band spectra by up to 10 dB for lower frequencies and around 2 dB in the upper frequency region. At the peak value of the simulated spectra, i.e. at 1250 Hz, the difference to the measured value is 4 dB. It is difficult to assess if these differences are relevant or not because of the different tyres used in simulation and measurement. Differences in measured sound pressure levels of several decibels for different tyres under otherwise identical operation condition are not uncommon [30]. A variation in width can already account for 1 dB to 2 dB difference. The shape of the simulated spectra is in general as expected. The peak lies at 1.25 kHz which is within the typically expected region as described in Sec. 2.2. Comparing Fig. 6.2 to Fig. 2.2 or Fig. 7.37 in reference [18], the slope from 100 Hz to 600 Hz should possibly be not as steep as it is. A definite assessment of this is, however, not possible without actual measurements of the simulated tyre.

The directivity of the radiated sound pressure for four third-octave bands is shown in Fig. 6.3. Results show good agreement with directivity patterns based sound intensity measurements which are shown in [18, Sec. 7.2.2].

The comparison between measurement and calculations, as well as the directivity for different frequencies, demonstrates that the initial model at least gives reasonable results, even though it might not perfectly predict radiated sound pressure spectra. For the purpose of studying the influence of modelling parameters on the simulation outcome it is considered to be sufficiently accurate.

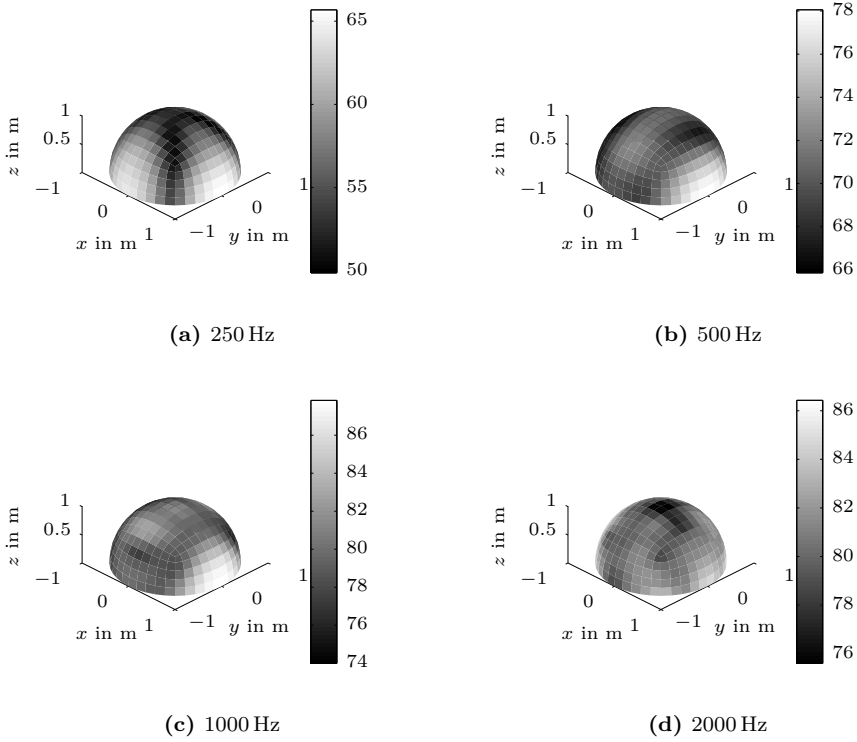


**Fig. 6.3.** The directivity of the radiated sound pressure for four different third-octave bands. The tyre is rolling in positive x-direction.

**Tab. 6.1.** Simulation results for the initial configuration.  $\bar{F}_Z$  is the average static load during the evaluated revolutions.

$L_{p,A,tot}$ in dB	$P_{loss}$ in W	$P_k$ in W	$\bar{F}_Z$ in N	$C_r$ in %
91.1	287.3	11.9	2431	0.55

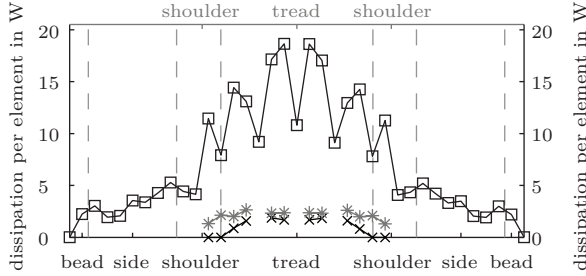


**Fig. 6.4.** Distribution of dissipation over the tyre cross section. ( $\square$ ) shell elements, ( $*$ ) solid elements, ( $\times$ ) contact springs. (—) marks the different tyre regions.

### 6.1.3. Rolling resistance

The rolling resistance, in terms of rolling loss  $P_{loss}$  and the rolling resistance coefficient  $C_r$ , is given in Tab. 6.1.

Validation of simulated rolling resistance is even more difficult than it was for sound radiation as there are no measurements available for the simulated tyre. In addition, a comparison with results reported in literature is insofar difficult as the measurement technique has a large impact on measured rolling resistance values. Under identical operating conditions variations of up to 20% between results obtain with different measurement devices have been observed [129, 130]. In [35, Paper C] a dissipated power of 467.5 W is calculated for a 205/55 ZR16 tyre with airplane profile which is rolling at 80 km/h on an ISO replica surface. With an axle load of 2773 N this gives a  $C_r$  of 0.76%. The smallest measured rolling resistance coefficients typically reported in literature for tyres of size 175 are also in the range of 0.7% to 0.8% [4, 30, 32, 130]. Even under the assumption that the implemented tyre was specifically optimised for a low rolling resistance, the simulations seem to underestimate the rolling losses by around 50%.

A possible explanation for this behaviour is given by the cross-sectional distribution of losses,  $P_{diss}$ , which is shown in Fig. 6.4. Roughly 70% of the dissipation happens in the shoulder and tread region, which is in very good agreement with res-

ults found in literature [16, 14, 42, 131]. A problem is the very small contribution of the solid elements to the dissipation. These elements model the highly damped rubber of the tread. High damping does not per se lead to high dissipation, as losses are given by the product of the loss factor and the stored potential energy (cf. (4.44)). Indeed, both Rao et al. [42] and Hall and Moreland [14] have come to the conclusion that the majority of energy dissipation occurs in the lower layers of the shoulder and tread areas (i.e. in the vicinity of the belts) and not in the solid rubber on top. In spite of this, the contribution from the solid elements still seems to be too small. One possible explanation is that the deformation of the elements and with it the potential energy, is underestimated in the model. The most likely cause for this would be wrong set of material input data for the simulations.

Additionally, a problem with the proportional damping implementation seems likely. The loss factor ranges from 0.04 at low frequencies to a maximum of 0.15 at high frequencies. Tyre models based on non-proportional damping typically assume values between 0.2 and 0.3 for the loss factor of the tread rubber [21, 35, 59]. This indicates that even though the current damping implementation gives an accurate description of losses for tyre response calculations, see Appendix C.2, the contribution from the solid elements is underestimated. While this certainly has an impact on the quantitative assessment of rolling resistance, it is an acceptable uncertainty for the qualitative evaluation of rolling resistance.

The losses attributed to the contact springs are also shown in Fig. 6.4. In total 11.9 W are dissipated. This is a somewhat fictive value, as was pointed out in Sec. 4.4. Nevertheless, the order of magnitude should be accurate enough to state that contact springs do not significantly contribute to overall rolling resistance for the initial configuration.

A combined frequency-wave order evaluation of the input power  $P_{in}$  is shown in Fig. 6.5. All of the relevant dissipation occurs below 200 Hz, with a wide maximum around 36 Hz. In the wave order domain, dissipation is concentrated at wave orders two to four. Wave orders 20 and higher only contribute to a very small extent to the dissipation. The combined greyscale plot shows that the dissipation occurs exclusively for frequency and wave order combinations which form a straight line running from the coordinate origin to around wave order 20 and 233 Hz. Based on the tyre circumference and the rolling speed, the fundamental excitation frequency is 6 Hz. Together with the higher harmonics this results in the characteristic straight line.

The distribution of dissipation along this line seems to be mainly governed by the size of the contact patch. A typical contact patch length of around 10 cm corresponds to roughly an eighth to a quarter of the wave lengths of the dominating wave orders 2 to 4. Hence, strong excitation can be assumed. Contrary, for wave orders 10 and higher the wave length becomes equal to or smaller than the contact length which means that the contribution of these orders to the global deformation of the tyre structure in the contact area is rapidly decreasing.

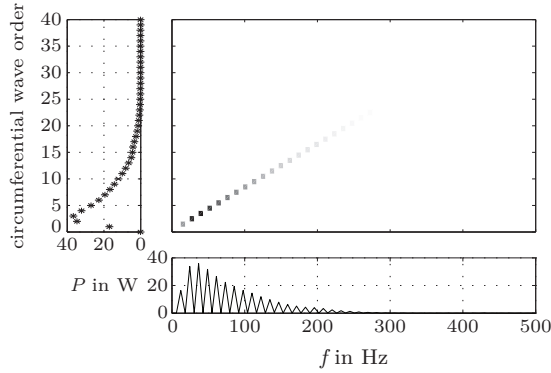


**Fig. 6.5.** Rolling losses for the initial configuration as a function of frequency (bottom, losses on the  $y$ -axis) and circumferential wave order (left, losses on the  $x$ -axis) and as a combined greyscale plot. Shades of grey re. maximum of plot with pure black being 100 % and pure white 0 %.

The fact that the frequency-wave order distribution of the rolling losses is exclusively governed by excitation properties can be explained by the dispersion plot in Fig. 6.6. It shows the relation between frequency and circumferential wave order for the eigenvectors  $\Psi_{n,s}$ , which are the solution to the undamped free response problem (4.10). Also shown is the frequency-wave order dependency of the excitation. No excitation occurs in the vicinity of any of the free solutions. Due to this there is no excitation of freely propagating waves which could consume more energy<sup>2</sup>.

With this the discussion of the results for the initial configuration is finished. In the following sections it will be evaluated how different operating conditions, tyre properties and modelling parameters affect the results. Note that for each of these studies detailed plots will only be shown if there are differences to the initial configuration which are worth reporting.

<sup>2</sup>This mismatch between excitation and free wave propagation is an important design criteria for tyres; freely propagating waves do not only increase rolling losses, but can also lead to overheating and the possible destruction of the tyre, see [13, Cha. 10].

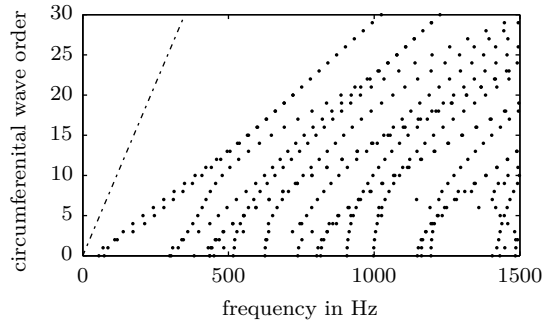


**Fig. 6.6.** Dispersion relations. Each dot represents a free response solution for the undamped tyre. (---) is the frequency-wave order relation for the forced excitation of the tyre at 80 km/h.

## 6.2. Operating conditions

### 6.2.1. Rolling speed

The time and frequency resolution of the simulation depends on the driving speed, see Sec. 4.5.1. This has to be considered when the speed dependency of rolling resistance and rolling noise are calculated. In Tab. 6.2 the time and frequency resolution for eight different driving speeds from 40 km/h to 110 km/h are given. For driving speeds below 70 km/h rolling noise cannot be completely calculated up to the requested 2.5 kHz third-octave band. At very low speeds the time steps  $\Delta t$  become rather long. This is a problem for the simulations of tyre/road interaction. For 40 km/h the number of sampling intervals over the tyre circumference has to be increased to 1024 to get numerically stable contact simulations. Still, implementation problems with higher circumferential resolution in the BEM code prevent rolling noise calculations for this speed. For 30 km/h even the increased resolution does not give a stable contact. Higher rolling speeds, in contrast, suffer from a decrease in frequency resolution which can be a problem when small-band rolling noise or mobility spectra are to be analysed.

The results for the different driving speeds are shown in Fig. 6.7. The rolling resistance stays nearly constant at 0.53% from 40 km/h to 70 km/h. It then increases slightly to 0.62% at 110 km/h. This agrees very well with observations reported in [13, 132].

The total A-weighted sound pressure levels range from 86.1 dB at 50 km/h to 95.3 dB at 110 km/h. The speed dependency of rolling noise is typically assumed to

**Tab. 6.2.** Time and frequency resolutions for different rolling speeds. \*: 40 km/h values are based on 1024 sampling intervals over the circumference.

speed in km/h	40*	50	60	70	80	90	100	110
$\Delta t$ in ms	0.16	0.26	0.21	0.18	0.16	0.14	0.13	0.12
$\Delta f$ in Hz	3.1	3.8	4.6	5.4	6.1	6.9	7.6	8.4
$f_{max}$ in Hz	3133	1958	2128	2741	3133	3524	3916	4308

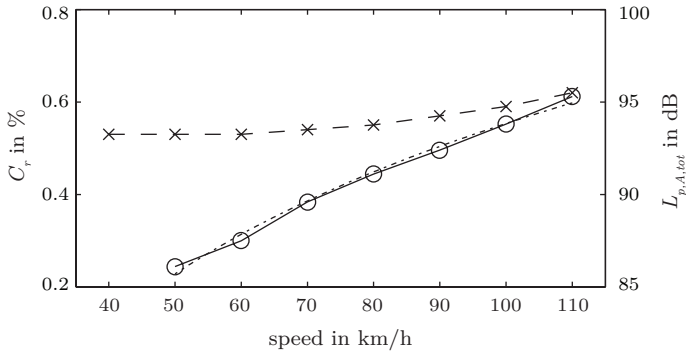


**Fig. 6.7.** Dependency of rolling resistance ( $-x-$ ) (left  $y$ -axis) and rolling noise ( $-o-$ ) (right  $y$ -axis) on the rolling speed. No rolling noise available for 40 km/h. Also shown is the fit  $L = A + B \log_{10}(V_{\text{km/h}})$  ( $\cdots$ ), with  $A = 11.7$  dB and  $B = 39.8$  dB.  $R = 0.997$ .

be of the form  $L = A + B \log_{10}(V_{\text{km/h}})$ , where  $A$  and  $B$  are constants and  $V_{\text{km/h}}$  is the speed in km/h [18]. Excellent agreement between the calculated sound pressure levels and this equation is achieved for  $A = 11.7$  dB and  $B = 39.8$  dB, see Fig. 6.7. These values for  $A$  and  $B$  are within the range of typically encountered values as reported in [18].

The limitations in maximum frequency for 50 km/h and 60 km/h do not notably affect the calculated  $L_{p,A,tot}$ . Two third-octave bands are missing for 50 km/h and one for 40 km/h. However, the sound pressure levels in each of these bands can be expected to be more than 10 dB below the maximum level of the whole third-octave band spectrum; in this case their contribution to the overall sound pressure level is irrelevant.

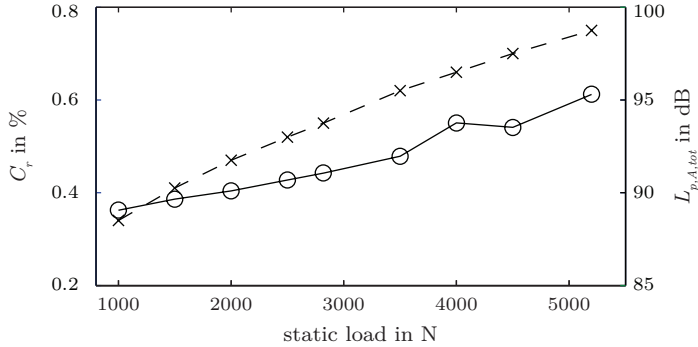


**Fig. 6.8.** Dependency of rolling resistance ( $-x-$ ) (left  $y$ -axis) and rolling noise ( $-o-$ ) (right  $y$ -axis) on the static load.

### 6.2.2. Static load

Rolling resistance coefficients and total A-weighted sound pressure levels for nine different static loads ranging from 1000 N to 5200 N are shown in Fig. 6.8. For the rolling noise there is an increase of 6 dB from the lowest load to the maximum load. This is within the range of results reported in [18, Sec. 9.3]. In the third-octave band spectra shown in Fig. 6.9 changes are mostly visible for lower and higher frequencies, while the region between 400 Hz and 1 kHz remains mostly unchanged. It is interesting that for lower frequencies the lower load causes higher sound radiation. This effect has also been reported in [18]. The region of the maximum in the third-octave band spectrum for 5200 N is in similar order of magnitude as the measured results. However, it is located between 1.25 kHz and 1.6 kHz, which is unusually high for rolling noise spectra.

Rather unexpected is the change of rolling resistance coefficient with static load, see Fig. 6.8. This behaviour contradicts the main idea behind the introduction of  $C_r$ , namely the observed linear dependency between rolling resistance (in terms of drag force or losses) and axle load. Noteworthy is that for higher loads the  $C_r$  lies in the range of 0.7% to 0.75%. These are values which are in agreement with what has been reported in literature (cf. Sec. 6.1.3).

### 6.2.3. Inflation pressure

The results for five different inflation pressures from 150 kPa to 350 kPa are listed in Tab. 6.3. Slightly varying results for the influence of the inflation pressure on the sound radiation have been reported in the literature [18, 133]. For summer

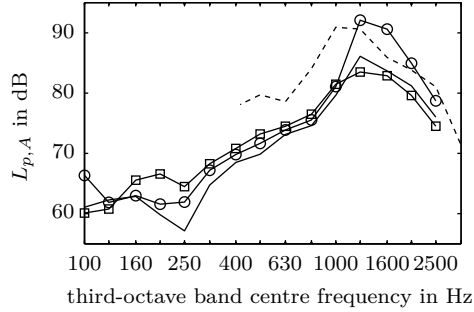


**Fig. 6.9.** Third-octave band sound pressure levels for static loads of 1000 N ( $-\square-$ ), 5200 N ( $-\circ-$ ) and the initial configuration ( $-$ ) (2820 N). Also shown are measurement results ( $---$ ) for a similar, but not identical tyre.

**Tab. 6.3.** Dependency of rolling resistance and rolling noise on the inflation pressure.

inflation pressure in kPa	150	200	250	300	350
$L_{p,A,tot}$ in dB	90.6	91.1	91.6	91.4	91.3
$C_r$ in %	0.61	0.55	0.54	0.50	0.47

tyres on smooth surfaces the reported effects range from no influence to +1 dB per 50 kPa increase in inflation pressure. For rougher surface even a decrease in sound radiation for increasing inflation pressure has been reported. In view of the variation of 1 dB in the simulated  $L_{p,A,tot}$  seems to be realistic.

The  $C_r$  decreases nearly linearly from 0.61 % at 150 kPa to 0.47 kPa at 350 kPa, which is reduction of 23 %. This agrees with the results presented in [16]. The average change of rolling resistance per 50 kPa increase of inflation pressure is 7 %. This is slightly lower than the average value of 10 % increase per 50 kPa which has been reported by several authors [13, 42, 133]. In conclusion, the model seems to be able to capture the effects of changing tyre inflation.

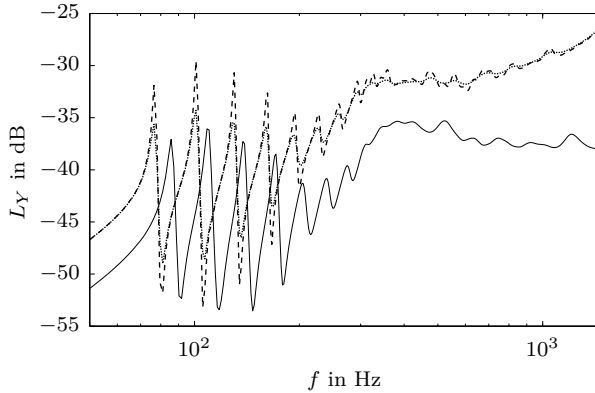


**Fig. 6.10.** Input mobilities on tread centre line different tyre configurations based on material data for 55°C: normal loss factors ( $\cdots$ ), halved loss factors ( $-\cdot-$ ). Also shown are results for 22°C ( $-$ ).  $L_Y = 20 \log_{10}(|Y/Y_0|)$ ,  $Y_0 = 1 \text{ N/(ms)}$ .

## 6.3. Tyre properties

### 6.3.1. Temperature effects

Due to dissipation processes the temperature of the tyre increases during rolling. Because the viscoelastic properties of rubber materials are highly temperature dependent, this change of temperature will also influence the dynamic properties of the tyre. While the initial tyre configuration used in this study is based on bulk material data for 20°C, bulk stiffnesses and loss factors are also known for 55°C. Bulk material loss factor data cannot be directly used as input into the model, see Sec. 5.5. For 20°C loss factors are instead obtained from measurement data. This is not possible for 55°C. In order to at least allow a coarse assessment of the change of dynamic properties due to the rise in temperature, two different simulations are performed for 55°C: in the first exactly the same frequency dependent loss factor as for 20°C is used. In the second, the loss factor is halved. This is based on the behaviour of the bulk material loss factor data for the sidewall and tread regions, which show roughly the same tendency. The changes in bulk stiffness considerably soften the tread and the sidewalls. This leads to pronounced changes in the dynamic tyre behaviour as is exemplified by the input mobility in Fig. 6.10<sup>3</sup>. The frequencies of the resonances below 300 Hz are shifted down by approximately

<sup>3</sup>The excitation area for all mobilities shown in this chapter is smaller than the one used in Appendix C.1. Because of this, mobilities are not directly comparable between these two chapters.

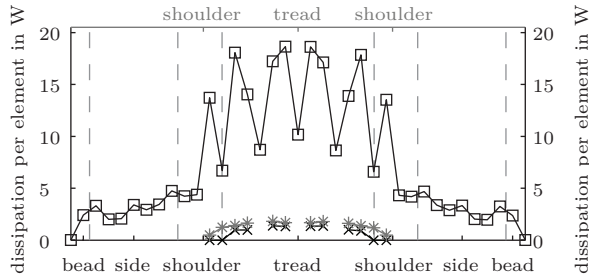


**Fig. 6.11.** Distribution of dissipation over the tyre cross section for 55°C and loss factor data for 20°C. (□) shell elements, (\*) solid elements, (×) contact springs. (--) marks the different tyre regions.

10%. For the very first peaks the response increases by roughly 2 dB for the case with unchanged loss factors and by approximately 6 dB for lower loss factors. Between 200 Hz and 600 Hz the amplitude difference due the temperature rise is roughly 4 dB regardless of loss factor. Above 600 Hz the effect of the softer tread compound becomes visible. Due to the local stiffness effects the mobility for 55°C starts to rise.

Because of the approximative nature of the loss factor data it is not particular useful to make a detailed analysis of the rolling resistance. The influence of the loss factor on the rolling losses is evident, in the case of the halved loss factor losses are also down by nearly exactly 50%. A comparison of the data for 20°C and 55°C for identical loss factors reveals the influence of stiffness change on rolling losses. The  $C_r$  rises from 0.55% for 20°C to 0.61% for 55°C. A comparison of the distribution of losses over the cross-section for both temperatures, see Figures 6.4 and 6.11, reveals that this is mostly due to an increased contribution of the outer parts of the tread area to the dissipation.

It has to be added that the observed 10% increase in  $C_r$  due the heating-up of the tyre is not observed in reality. In contrast, rolling losses usually go down for rising temperatures conditions [13]. This is partly caused by an increase in internal air pressure and partly by the decrease in loss factor which cannot be modelled with the necessary accuracy here.

The change of radiation for increasing temperature is shown in Fig. 6.12. For both 55°C loss factor configurations there is no significant change of the sound pressure level in the 1.25 kHz band which dominates radiation for the 20°C material data. However, for the 1000 Hz band rather drastic changes can be observed. Compared to the initial configuration the levels increase by 5 dB for unchanged loss factors and 8.2 dB for reduced loss factors. For frequencies above 1.25 kHz

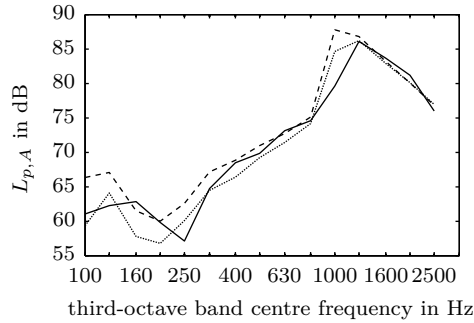


**Fig. 6.12.** Third-octave band sound pressure levels for different tyre configurations based on material data for 55°C: normal loss factors ( $\cdots$ ), halved loss factors ( $-\cdot-$ ). Also shown are results for 22°C ( $-$ ).

radiation is generally weaker for the higher temperature. The same can be observed for the 250 Hz to 800 Hz region for 55°C and normal loss factor data. This results in the overall A-weighted sound pressure level for 55°C and normal loss factor data being 0.5 dB lower than for the initial 20°C configuration; this is despite the dramatic increase in the 1 kHz band. For the case of halved loss factors overall sound radiation increases by 0.8 dB instead.

A summary of empirical and simulation results in [18] suggests that tyres with a softer tread compound should be quieter than tyres with a harder compound. However, the biggest reduction of 3 dB is obtained for “aggressive” tread designs, for “smoother” designs as the one of the implemented tyre lower reductions can be expected. Data on the influence of the sidewall stiffness, which is also considerably changed by temperature, on rolling noise could not be found in the literature. Yet, it seems reasonable to assume that the influence is less than that of the tread compound.

As a final note it shall be added that broader peak in the rolling noise spectrum which is obtained for the 55°C configurations seems to be more realistic than the single maxima at 1.25 kHz which is observed for 20°C, see e.g. the measurement data in Fig. 6.2 or Fig. 2.2.

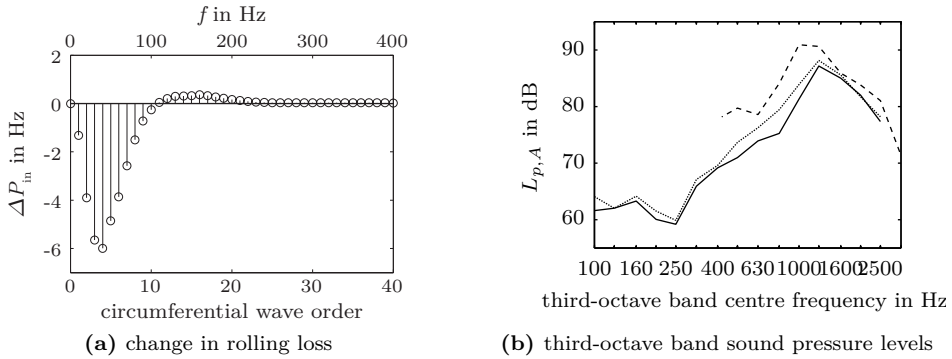


**Fig. 6.13.** Results for material parameters before optimisation. (a) Change in dissipated power over circumferential wave order/frequency compared to initial configuration with optimised material values. Negative values denote reduction. Note: Double x-axis due to fixed relation between wave order and frequency for forced excitation. (b) Third-octave band sound pressure levels for optimised (—) and non-optimised (···) material values. Also shown are measurement results (—) for a similar, but not identical tyre.

### 6.3.2. Material parameters without optimisation

In Appendix C the mobilities for WFE tyre models based on material values before and after the optimisation process are compared with measurement results. In general there is already good agreement between measured mobilities and simulated mobilities based on the material parameters directly after condensation. Yet, there also clear differences between the mobilities before and after the optimisation. Whether these differences are also noticeable in rolling noise and rolling resistance is evaluated here.

The  $C_r$  value for non-optimised material data is 0.51%. This is approximately 9% lower than for the optimised material values. In Fig. 6.13a it is shown that the change predominantly happens for wave orders and frequencies below order 10 and 100 Hz, respectively. Between orders 10 to 20, i.e. 100 Hz to 200 Hz, there is a slight increase in rolling losses for the non-optimised material values.

Rolling noise increases from 91.1 dB for optimised values to 92.2 dB for non-optimised values. The rolling noise spectrum is shown in Fig. 6.13b. The curve for the non-optimised material values is on average 1 dB higher for all third-octave bands apart from 125 Hz and 2 kHz.

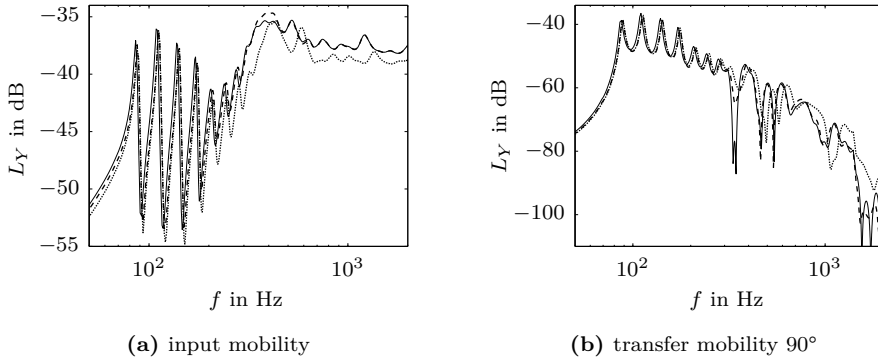


**Fig. 6.14.** (a) Input and (b) transfer mobilities on tread centre line for tyre models with all coupling terms (—), no PQ terms ( $\cdots$ ), and no  $P_{i3}/Q_{i3}$  terms (—). Transfer mobility at  $180^\circ$  on the circumference.  $L_Y = 20 \log_{10}(|Y/Y_0|)$ ,  $Y_0 = 1 \text{ N}/(\text{ms})$ .

### 6.3.3. Coupling-terms in the shell element rigidity matrix

Some of the shell elements in the WFE tyre model have stiffness terms  $P_{i3}$  (where  $i = 1, 2$ )<sup>4</sup> which couple in-plane strain and shear, and stiffness terms  $P_{i3}$  which couple bending and twist of curvature. This is due to the angle at which the belt layers are oriented with respect to the tyre coordinate system and the derivation of the moment resultants, see Sections 5.2.1 and 5.2.2. The asymmetry of the laminate with respect to the middle surface also leads to coupling between extensional and bending motion. This is expressed by the **PQ** submatrix in the rigidity matrix (5.34).

For two particular reasons it is worthwhile to investigate the influence these coupling terms have on rolling resistance and rolling noise. First of all, the values which are obtained for the individual coupling terms are very sensitive to the thickness of the individual layers, see (5.27). The handling of the belt layers can be problematic, because these combine the by far highest extensional stiffnesses with a very small thickness. Minor errors in thickness can lead to considerable differences in the calculated stiffness of the shell elements. Secondly, a previous WFE tyre model which has been successfully used for simulations such as the calculation of rolling losses and sound radiation [118, 79], did not include the mentioned coupling terms. This was because the necessary input data for these terms was not available.

Examples for input and transfer mobilities obtained without coupling terms are

<sup>4</sup>In the following  $i = 1, 2$  will not be explicitly written out any more.



**Fig. 6.15.** Upper part of the WFEM tyre mesh. Shell elements with  $P_{i3}/Q_{i3}$  coupling terms marked.

shown in Fig. 6.14. The omission of the  $P_{i3}/Q_{i3}$  coupling terms has nearly no influence on the mobilities at all. The biggest difference compared to the configuration with all coupling terms is an increase of roughly 0.7 dB for the peak of the first belt bending order around 390 Hz. Some smaller differences can also be observed for the transfer mobility for frequencies above 1.5 kHz. The influence of the coupling between extensional and bending motion which is expressed by the **PQ** terms is considerably higher. In the input mobility all peaks are shifted to higher frequencies while amplitudes are lower than for the initial configuration. The frequency trend is also observable in the transfer mobility, however, amplitudes are generally higher than for the other configurations.

The variations in observable effects caused by the omission of the different coupling terms can be explained by the number of elements which are affected. All of the shell elements in the tyre model originally contain at least some non-zero entries in the **PQ** submatrix. Hence, by setting **PQ** to zero the tyre is affected globally. The  $P_{i3}/Q_{i3}$  terms are only relevant for elements with belt layers; the ply has its principal axis of orthotropy aligned with the tyre coordinate system meaning there is no in-plane strain and shear or bending and twist of curvature coupling. Moreover, due to the antisymmetry of the belt angles all  $P_{i3}/Q_{i3}$  terms also vanish for elements with two belt layers. In the end only one element in the shoulder area on each side of the tyre has non-zero  $P_{i3}/Q_{i3}$  terms, see Fig. 6.15.

The influence of the coupling terms on rolling resistance is only marginal. The  $C_r$  reduces to 0.53 % for no **PQ** terms and 0.54 % for no  $P_{i3}/Q_{i3}$  terms. A surprising result is obtained for the third-octave band rolling noise spectra, see Fig. 6.16. While the omission of the coupling between in-plane and bending motion has a limited effect, rather drastic changes can be observed when the  $P_{i3}/Q_{i3}$  terms are ignored. The A-weighted sound pressure levels in the 800 Hz and 1 kHz third-octave bands increase by more than 11 dB. In all other bands increases of 2 dB to 3 dB can be observed. Results also match reasonably well with the measurements for the 205/55 R16 tyre. It is astonishing that by setting two stiffness terms in two elements to zero such an extreme change is obtained. An investigation of calculated transfer mobilities to 20 further points on the tyre and contact force spectra (for both of which results are not shown here), does not provide an explanation.

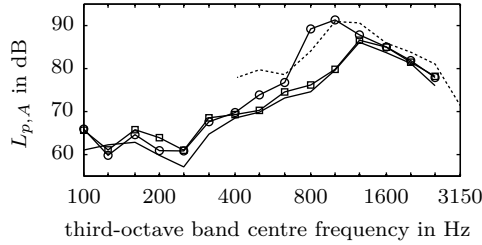


**Fig. 6.16.** Third-octave band sound pressure levels for tyre models with all coupling terms (—), no PQ terms ( $\square$ ), and no  $P_{i3}/Q_{i3}$  terms ( $\circ$ ). Also shown are measurement results (---) for a similar, but not identical tyre.

This might instead be given in [79], where it has been shown that wave components of low order in cross-sectional and/or circumferential direction are the dominating vibrational sources for sound radiation over the complete frequency region. This is because even though these modes are excited far above their own resonance frequencies, they are very efficient radiators at higher frequencies. The slightly increased response around 390 Hz in the input mobility for the tyre without  $P_{i3}/Q_{i3}$  terms, see Fig. 6.14, might indicate an increased response from one or more of these dominating modes. However, further investigations are necessary to prove this, until then this is pure speculation.

## 6.4. Modelling parameters

### 6.4.1. Centrifugal effects

It is a generally accepted fact that rotational effects influence the dynamic properties of rotating tyres. It is, however, unknown whether sound radiation and rolling resistance are as well influenced by these effects. As the Doppler shift is inherently included in the necessary transformation procedures between Euler and Lagrange reference system, only the effect of the centrifugal force can be investigated. In the simulation the centrifugal force is modelled as an additional pretension term  $N_{\text{circ},\Omega}$ , see (5.43). For speeds of 50 km/h, 80 km/h, and 110 km/h simulations are performed where the centrifugal stiffening term is set to zero.

The influence of the centrifugal forces on the tyre dynamics is clearly visible in Fig. 6.17. In this figure an input and a transfer mobility for a tyre with a centrifugal stiffening term  $N_{\text{circ},\Omega}$  corresponding to 110 km/h are shown. Magnitudes do not change much, but there is clear shift in resonance frequencies below 1 kHz. This is especially evident for the transfer mobility.

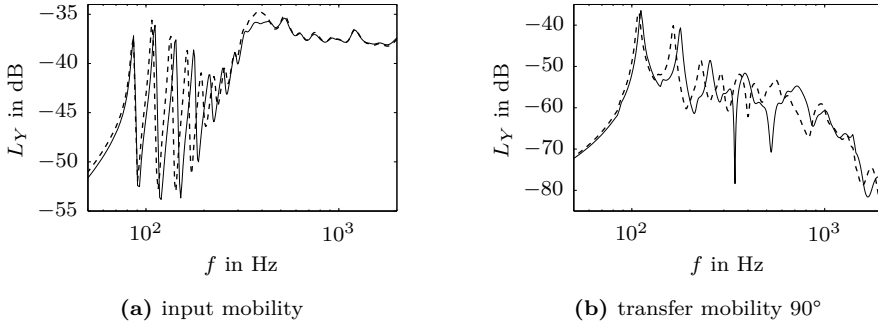


**Fig. 6.17.** (a) Input and (b) transfer mobilities on tread centre line with (—) and without (---) centrifugal stiffening for 110 km/h. Transfer mobility at 90° on the circumference.  $L_Y = 20 \log_{10}(|Y/Y_0|)$ ,  $Y_0 = 1 \text{ N}/(\text{ms})$ .

**Tab. 6.4.** Dependency of rolling resistance on centrifugal stiffening.

speed in kmh/h	50	80	110
$C_{r,with}$ in %	0.53	0.55	0.62
$C_{r,without}$ in %	0.54	0.58	0.67

In Fig. 6.18 the A-weighted third-octave band rolling noise spectra for speeds of 50 km/h, 80 km/h, and 110 km/h can be seen. For each case results with and without centrifugal stiffening are shown. The influence of the centrifugal term is absolutely negligible for all three speeds.

As shown in Tab. 6.4, rotational stiffening is no longer insignificant when rolling resistance is calculated for higher speeds. At 80 km/h there is already a 5% difference when  $N_{\text{circ},\Omega}$  is set to zero. Due to the  $\Omega^2$  proportionality of  $N_{\text{circ},\Omega}$ , the centrifugal pretension has increased by 30% at this speed. This is similar to the step from 150 kPa to 200 kPa in Sec. 6.2.3, where the resulting difference in  $C_r$  is 9%. An increase of inflation pressure also increases the lateral pretension, which is not the case for the centrifugal stiffening due to rotation. This could indicate that for the case of changing inflation pressure, the change of lateral pretension has a smaller impact on the changes in rolling resistance than the change of circumferential pretension. This is supported by the fact that in the lower frequency regions which exclusively determine rolling losses, see Fig. 6.5, the dynamic behaviour of the tyre is very well approximated by an elastically supported ring under circumferential pretension (cf. Sec. 2.2.1).

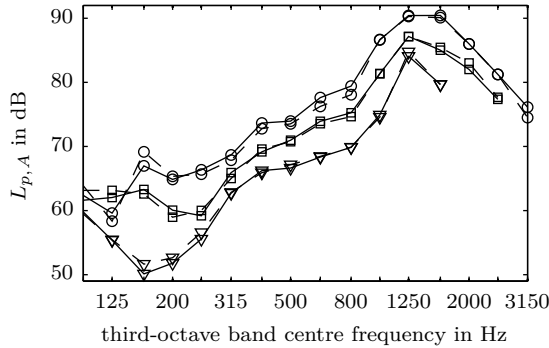


**Fig. 6.18.** Third-octave band sound pressure levels with (—) and without (---) centrifugal stiffening for speeds of 50 km/h ( $\nabla$ ), 80 km/h ( $\square$ ), and 110 km/h ( $\circ$ ). Non-identical frequency ranges due to dependency of sampling frequency on rolling speed.

**Tab. 6.5.** Dependency of rolling resistance and rolling noise on the stiffness of the contact springs.

contact spring stiffness in N/m	$1 \cdot 10^4$	$2 \cdot 10^4$	$3 \cdot 10^4$	$4 \cdot 10^4$	$5 \cdot 10^4$	$6 \cdot 10^4$
$L_{p,A,tot}$ in dB	82.4	86.3	88.2	89.6	91.1	92.7
$C_r$ in %	0.53	0.54	0.54	0.55	0.55	0.56
$\bar{F}_Z$ in N	2480	2450	2444	2443	2431	2444

## 6.4.2. Contact model

### Contact springs

A critical parameter in the modelling of the tyre/road interaction is the contact spring stiffness  $k$ . Results for values of  $k$  in the range of  $1 \cdot 10^4$  N/m to  $6 \cdot 10^4$  N/m are shown in Tab. 6.5. The influence on the rolling resistance coefficient  $C_r$  is very limited. However, the sound radiation is strongly effected by the stiffness of the contact spring. Fig. 6.19 shows that the position and amplitude of the maximum in third-octave band spectrum is highly dependent on the contact spring stiffness. From the lowest to the highest stiffness the peak amplitude increases by more than 15 dB. At the same time the position of the maximum shifts from the 1 kHz third-octave band to the 1.25 kHz band. For the highest frequency bands the amplitude differences are around 6 dB. Below 800 kHz the changes are comparably small with

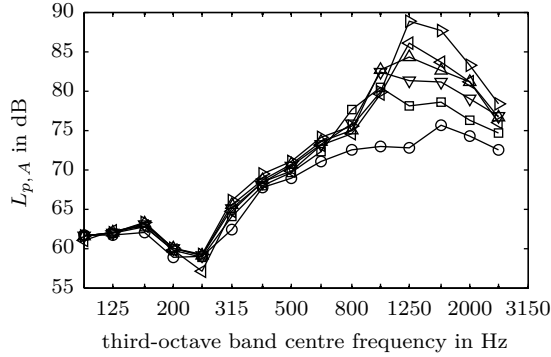


**Fig. 6.19.** Third-octave band sound pressure levels for contact stiffnesses of  $1 \cdot 10^4$  N/m ( $\circ$ ),  $2 \cdot 10^4$  N/m ( $\square$ ),  $3 \cdot 10^4$  N/m ( $\nabla$ ),  $4 \cdot 10^4$  N/m ( $\triangle$ ),  $5 \cdot 10^4$  N/m ( $\triangleleft$ ), and  $6 \cdot 10^4$  N/m ( $\triangleright$ ).

around 3 dB.

It is difficult to assess what the cause for these rather dramatic changes is. The stiffness of the contact springs certainly affects the tyre deformation during contact. Tyre and contact springs act as a set of two springs in series. The overall stiffness at a contact point  $e$  is given as

$$k_{tot} = \left( \frac{1}{g_{e,e}(0)} + \frac{1}{k} \right)^{-1}. \quad (6.1)$$

Depending on the actual values of  $g_{e,e}(0)$  and  $k$ , both the tyre and the spring will show a certain deformation due to the contact force. This is exemplified for two different contact stiffnesses in Fig. 6.20. The combined deformation of tyre and spring can still not penetrate into the road. This condition is fulfilled with both contact stiffness, see Figures 6.20a and 6.20c. In Figures 6.20b and 6.20d only the tyre deformation is plotted without the contribution from the spring is plotted. For the lower contact stiffness of  $3 \cdot 10^4$  N/m the deformation of tyre structure is clearly lower than for spring with  $5 \cdot 10^4$  N/m stiffness. This is because for the softer spring a larger part of the total deformation is allocated to the spring.

This difference affects the excitation of the tyre structure, even though it is not the contact displacement but the contact force which is the input variable into the WFE tyre model. Evidently, the magnitude of the contact force is not affected by how the displacement is shared between tyre structure and spring. This can be seen in Tab. 6.5 where the average contact force over the evaluation period,  $\bar{F}_Z$

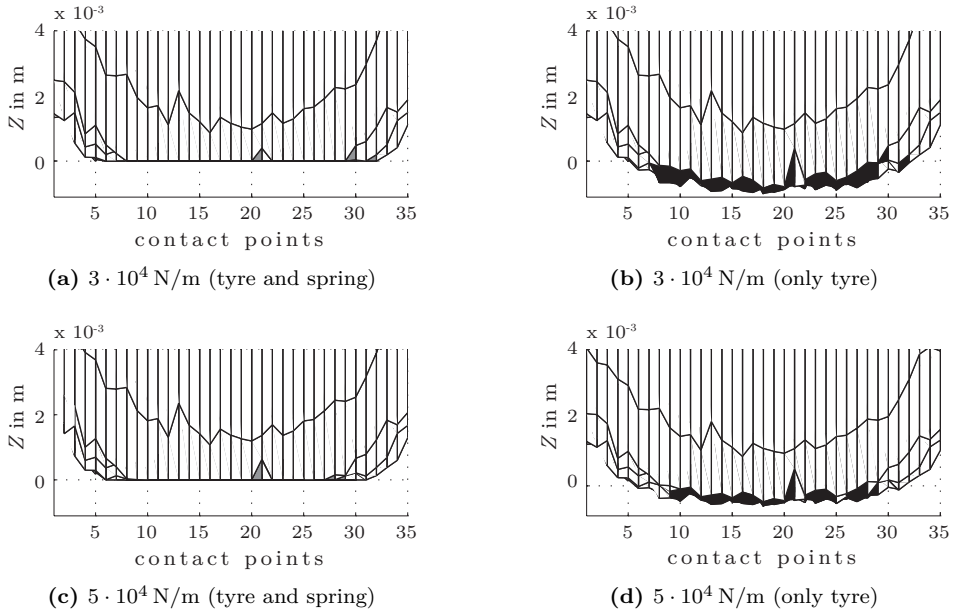


**Fig. 6.20.** Side view of tyre deformation due to static loading for two different contact stiffnesses. For each stiffness the total deformation due to tyre and spring deformation ((a) and (c)), and only the tyre deformation ((c) and (d)) are shown. The road is located a  $Z = 0$ . One contact interval is 3.5 mm long.

is nearly identical for all contact spring stiffnesses. However, the local behaviour of the contact force is dependent on the contact stiffness. The distribution of contact forces over the contact region or the force spectrum are influenced by  $k$ . Examples are given in Fig. 6.21, where the average contact force power spectra over two revolutions for two different positions on the tread are shown. Again contact stiffnesses of  $3 \cdot 10^4$  N/m and  $5 \cdot 10^4$  N/m are considered. For the position at the tread centre, see Fig. 6.21a, the contact force is always larger for the higher contact stiffness. The differences between the contact force spectra are 0 dB at 100 Hz, 1.6 dB at the peak in the 420 Hz region and 1.1 dB for the peak in the 960 Hz region. For the peak around 1170 Hz the difference increases to 4.3 dB.

For the position at the tread side, Fig. 6.21b, the softer spring results in a contact force which is 0.7 dB higher at 100 Hz than the force for stiffer spring. This decreases to 0.2 dB for the peak around 600 Hz. For higher frequencies it is again the stiffer spring which results in the higher amplitudes. The difference is

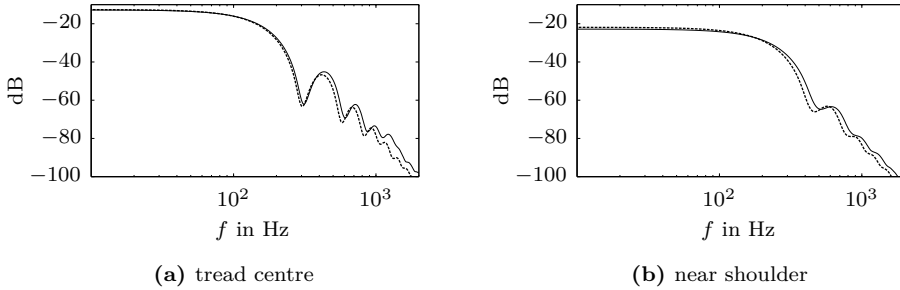


**Fig. 6.21.** Average contact force power spectra over two tyre revolutions for contact stiffnesses of  $3 \cdot 10^4$  N/m (---) and  $5 \cdot 10^4$  N/m (—). The forces are for contact near the tread centre line (a) or near the shoulder region (b).

around 3.0 dB in this frequency region.

Tab. 6.5 gives the difference in  $L_{p,A,tot}$  between stiffnesses of  $3 \cdot 10^4$  N/m and  $5 \cdot 10^4$  N/m as 2.9 dB. The third-octave band maxima are 82.7 dB at 1 kHz for the lower stiffness and 86.1 dB at 1.25 kHz for the higher stiffness. For the latter the peak also seems to be more pronounced. These tendencies (lower frequencies and amplitudes for the lower stiffness, higher amplitudes and frequencies for the higher stiffness) correlate quite well with the observed differences in force spectra. Also the shift of the third-octave band maxima from 1 kHz (soft spring) to 1.25 kHz (stiff spring) could be explained by the sudden increase in difference between the contact forces from 1 kHz to 1.25 kHz.

### Drum curvature

The measured third-octave band rolling noise spectrum which is used for comparison is based on a tyre rolling on a drum and not a real road. The drum curvature leads to differences in the tyre deflection in the contact zone. In order to investigate whether this has any consequence on rolling noise and/or rolling resistance, the road surface profile is modified to resemble the curvature of a drum with a radius of 1.54 m, see Fig. 6.23a.

The third-octave band rolling noise spectra for rolling on a flat surface and a drum are shown in Fig. 6.22. Above 160 Hz the curve for the drum is always higher than the one for the normal road surface. The maximum level difference is 5.5 dB for the 1.25 kHz third-octave band. For the 1.25 kHz, 1.6 kHz and 2 kHz bands the difference to the measured third-octave bands is less than 2 dB.

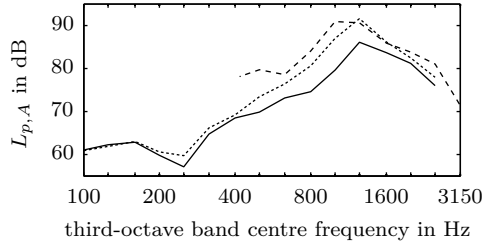


**Fig. 6.22.** Third-octave band sound pressure levels for a tyre rolling on a drum ( $\cdots$ ) and a tyre rolling on a flat road surface ( $—$ ). Also shown are measurement results ( $---$ ) for a similar, but not identical tyre which is rolling on a drum.

In Fig. 6.23b the average contact force power spectra for an excitation position close to the tread centre are shown. The peaks are shifted to slightly higher frequencies for the drum case. This is caused by the slightly smaller contact patch on the drum. The force spectra do not reveal significant differences in level which could explain the rather high difference in sound radiation in the 500 Hz to 1.25 kHz region. It is possible that the change of contact patch due to drum curvature affects the static deflection of the tyre in such a way that the amplification due to the horn effect is increased. Regarding the radiation calculations it has to be added that the drum curvature could not be taken into account there.

In [13] the relation between rolling losses on a drum and on a flat surface is given as  $C_{r,d} = C_{r,f} \sqrt{1 + \frac{r_0}{r_d}}$ , with the subscripts  $d$  and  $f$  denoting drum and flat surface, and  $r_0$  and  $r_d$  being the tyre and drum radius. According to this formula the rolling resistance should be 9.0% higher for the simulated case (where  $r_0 = 0.29$  m and  $r_d = 1.54$  m). In the actual simulations the rolling resistance increases from 0.55% for a flat road to 0.60% for the drum, which corresponds to 9.1%.

### 6.4.3. Radiation model

#### Height of tyre above road surface

Due to numerical reasons, see Sec. 4.3.3, the tyre is slightly lifted above the road surface for the BEM calculations. As the horn effect is very sensitive to any geometry modification [26], this lift can have a substantial influence on sound radiation. In [100] it is shown that for a 205/55 R16 tyre a lift of 1 mm allows accurate modelling of the horn effect below 3 kHz. The same value is used for

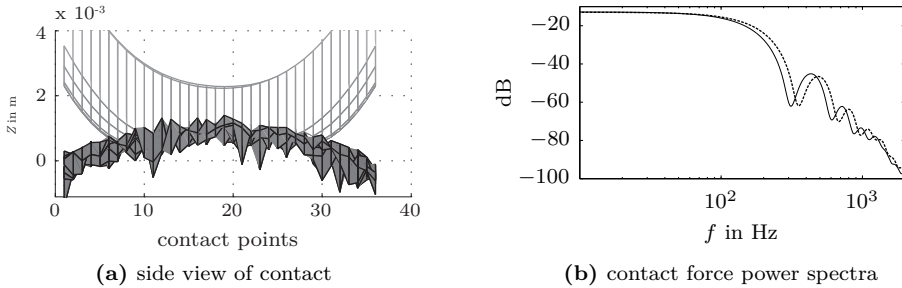


**Fig. 6.23.** (a) Side view of tyre deformation due to static loading on drum. One contact interval is 3.5 mm long. (b) Average contact force power spectra over two tyre revolutions for a flat road surface (—) and a drum (---). Contact is near the tread centre line.

the initial configuration here. However, in contrast to the tyre investigated in this study, the tyre considered in [100] does not have a profile. It is possible that the rather pronounced circumferential voids in the current tyre lead to a different sensitivity with regard to the height of the tyre above the rigid plane. In order to investigate this, sound radiation is calculated for lifts from 0.5 mm to 1.5 mm.

For lifts of 0.5 mm and 0.75 mm the calculated sound pressure levels are higher than those for the standard of 1 mm for frequencies up to 400 Hz and between 800 Hz and 1.6 kHz. In the important 1.25 kHz third-octave band the sound radiation for 0.5 mm is 3.5 dB higher than for 1 mm lift. The value for 0.75 mm is nearly identical to the one for 1 mm. For 2 kHz and 2.5 kHz 1 mm gives roughly 2 dB higher sound radiation. It is noteworthy that the spectra for 0.5 mm and 0.75 mm lift are almost identical except for the frequency range of 800 Hz to 1.25 Hz. Between 1 kHz and 1.6 kHz the curves for 0.75 mm and 1 mm are very close.

The tendency that a higher lift above the road surface reduces the sound pressure levels for the majority of third-octave bands does not continue for a lift of 1.25 mm. Instead the spectrum is almost identical to the one for a lift of 0.75 mm lift. Finally, rather drastic differences are obtained for a raise of 1.5 mm. A distinct peak develops at 630 Hz which is 15 dB higher than levels obtained with the lower lifts. The levels in the surrounding third-octave band are also significantly higher than before. The cause for this peak cannot be clearly identified. It is possible that the region between the road and the lifted tyre forms a duct-like structure which has its resonance frequency around 630 Hz. Regardless of what physical effect leads to this peak, it is certain that a lift of 1.5 mm does not anymore accurately model the sound radiation from a tyre in contact with the ground.

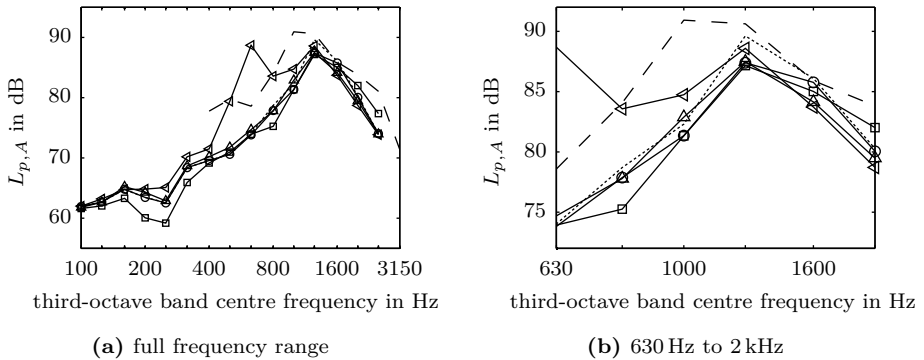


**Fig. 6.24.** Third-octave band sound pressure levels for different heights of the tyre above the road surface: 0.5 mm ( $\nabla$ ), 0.75 mm ( $\circ$ ), 1 mm ( $\square$ ), 1.25 mm ( $\triangle$ ), 1.5 mm ( $\triangleleft$ ). Also shown are measurement results (—) for a similar, but not identical tyre.

In Sec. 6.1.2 it was concluded that the initial configuration possibly underestimates rolling noise. There is the possibility that this is partly due to the 1 mm lift above the road surface which is used for the BEM calculations. With lifts of 0.5 mm or 0.75 mm not only the peak amplitude at 1.25 kHz is closer to measured values; also low frequency radiation seems to be more realistic. Numerical instabilities or an increase in calculation time were not observed with the reduced heights.

### Tyre deformation

In Fig. 4.11 the differences between a BEM mesh with and without the effects of static tyre deformation are shown. The differences in geometry surely affect the amplification due to the horn effect. The extent of this influence is shown in Fig. 6.25. Although the accuracy of the solution for the mesh including the deformation remains unclear, it is safe to assume that third-octave band spectra obtained with a completely round tyre mesh are not closer to reality. The round tyre does not only model the horn geometry incorrectly, it also places the sources on the tyre at the wrong location.

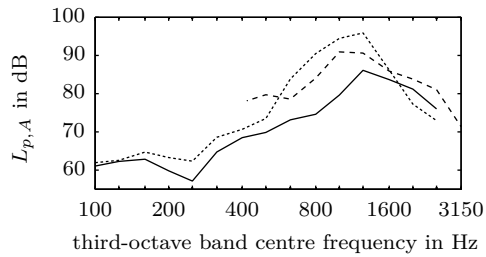


**Fig. 6.25.** Third-octave band sound pressure levels for BEM mesh of a completely round tyre ( $\cdots$ ) and a tyre with static deformation ( $-$ ). Also shown are measurement results ( $-$ ) for a similar, but not identical tyre.



## 7. Conclusions and future work

A tool for the simulation of car tyre rolling losses and rolling noise was presented. It consists of a non-linear tyre/road contact module which is formulated in the time-domain, a waveguide finite element tyre model and a boundary element method radiation module. Rolling resistance is calculated based on the input power for steady-state rolling. Furthermore, a method for the reduction of tyre design data into equivalent material properties for shell and solid elements was presented. Using this method, a complete anisotropic tyre model for a 175/65 R14 tyre was implemented. Material parameters were further optimised using a genetic algorithm. Mobilities, rolling resistance and rolling noise were calculated for different scenarios in which individual parameters in the simulation process were changed. In Sec. 7.1 some of the main findings of this study will be discussed briefly. This is followed by some suggestions for future work in Sec. 7.2.

### 7.1. Conclusions

#### 7.1.1. Condensation of material properties

The proposed procedure seems to work adequately well with respect to the simulation of the tyre dynamics. Initial material values give acceptable match to measured mobilities. Good agreement is achieved after further optimisation of the material data. The exception are transfer mobilities in the lateral belt direction and to sidewall positions for mid to high frequency regions. This might indicate problems with the lateral bending stiffness.

A challenge is the high complexity of the model which makes a manual optimisation based on physical reasoning very difficult. The proposed automatic optimisation procedure is not without flaws either. There is the risk that it produces unphysical combinations of material properties which still give good match with measured mobilities.

A further uncertainty is attached to the choice of validation towards measured mobilities. As just one or two points on the tyre are investigated at a given time, only very limited insight into the dynamic behaviour is obtained. There is in particular no guarantee that a validation towards any given selection of mobilities, however large that group might be, is sufficient to assure that tyre dynamics are really captured adequately enough for contact and/or radiation calculations. This

is exemplified by the simulations for the tyre without coupling terms for in-plane strain/shear and bending/twist of curvature coupling. The obtained mobilities are almost exactly identical to those for the normal tyre configuration. Yet, the third-octave band rolling noise spectrum changes dramatically. In contrast, if the coupling of extension and bending is ignored, mobilities change notably, but sound radiation stays nearly unchanged. In general, it does not seem possible to conclude that two tyres with similar mobilities will also have similar rolling resistance and rolling noise.

In this thesis it has also been implicitly assumed that the measured mobilities are correct. Though there are no indications of measurement problems, this is evidently a problematic assumption.

### 7.1.2. Initial simulation results

The lack of measurement data for the actual tyre makes a judgement of the model quality difficult. Quantitatively, the initial configuration seems to underestimate both rolling resistance and rolling noise. General qualitative effects are captured accurately, though. This can be seen as indication that the tyre input parameters are not yet correctly determined. For the rolling resistance simulation the underestimation of typical  $C_r$  values found in literature can also partly be explained by the shortcomings of the proportional damping approach used in this work. It can be expected that with a more realistic distribution of damping between shell and solid elements higher rolling losses are obtained. The influences of driving speed and inflation pressure on both rolling resistance and rolling noise seem to be captured quite well by the simulations. The same is true for the influence of static load on the sound radiation. Not realistic is the significant increase of  $C_r$  with the static load. Interestingly,  $C_r$  values which are in the right order of magnitude compared to values given in literature are obtained for very high loads. This change of  $C_r$  with static load might be caused by the stiffnesses of the contact springs. As these are assumed to be constant, they are only correct for one particular ratio of *apparent* and *real area of contact*. This ratio is affected by the static load. Accordingly it seems necessary to adjust the spring stiffness as well with changing load.

### 7.1.3. Tyre temperature

The simulations for a tyre at operating temperature suffer from an inability to capture the temperature-dependent damping variations accurately. Nevertheless, it can be shown that the sound radiation is affected by the softer rubber material at higher temperatures. In the simulations rolling resistance raises with temperature. This contradicts what is suggested in literature. Yet, it is again difficult to make a clear judgement due to lack of adequate validation data.

#### **7.1.4. Influence of material parameter optimisation on rolling noise and rolling resistance calculations**

Variations between non-optimised and optimised material values can be observed in the rolling resistance and rolling noise simulations. With less than 10 % difference for the rolling resistance and a 1.1 dB difference in the overall sound pressure level it is questionable if a time consuming optimisation of material parameters is necessary for all applications. For relative comparisons between different tyres it might be sufficient to directly use the material values obtained in the condensation process.

#### **7.1.5. Coupling terms in the rigidity matrix**

From a physical point of view it is quite interesting which changes on a global scale are caused by a slight modification of two elements in the tyre structure. It was proposed that this might be due to the differences in excitation of individual low order modes which are significant radiators. The available data needs to be further analysed to see if any proof for this theory can be found.

#### **7.1.6. Centrifugal effects**

The simulations suggest that centrifugal stiffening is not of relevance for the calculation of rolling noise for speeds up to 110 km/h and higher. Some effects are seen for the rolling resistance, which decreases when centrifugal forces are taken into consideration for higher speeds. Because of this, it might be useful to account for centrifugal forces during simulations.

#### **7.1.7. Contact parameters**

The contact springs are a critical parameter for rolling noise simulations. The chosen spring stiffness has a large influence on the contact force spectra in the frequency regions relevant for rolling noise. It is not clear how the correct spring stiffness can be determined. Andersson and Kropp [91] describe a procedure for non-linear contact springs but this requires very detailed road surface data. Stiffness values are furthermore only valid for a particular road surface and a given static load.

Rolling resistance is in major parts a low frequency phenomena. As long the contact spring stiffness is within reasonable bounds, no major changes for  $C_r$  are observed. This indicates that for example for the comparison of rolling resistance for different road surfaces, no re-adjustment of the stiffnesses is necessary if the road surfaces do not change too much. As was pointed out in Sec. 7.1.2, this might no longer be true if the tyre load changes.

In the simulations the drum curvature has a quite high influence on sound radiation which could not be explained by the force spectra. It is possible that change of contact deflection leads to variation in horn geometry which causes amplification changes. The results for the sound radiation are, nevertheless, not completely accurate because the boundary element model was still based on a flat ground surface. For the radiation calculations the drum, its curvature, and possible open areas around it are not considered.

### **7.1.8. Radiation parameters**

It is obvious that the tyre geometry in and around the contact zone greatly influences the sound radiation. Based on physical reasoning it is clear to see why the tyre deformation has to be taken into account for the BEM mesh. The slight lift of the tyre above the road surface is more difficult to assess. In its character it is very similar to the contact springs: both parameters have a huge impact on the calculated third-octave band rolling noise spectra, yet it is difficult to decide what the correct value for the stiffness or the lift should be. It could be reasonable to assume that the lowest value which does not give numerical problems should be the right one. The risk with this approach is that it might be difficult to judge when exactly numerical errors start to occur. Furthermore, Brick [100] showed that for horn effect simulations there is tradeoff between amplitude and frequency accuracy which is determined by the amount of lift of the tyre above the road surface.

It is possible that for some of the previously mentioned variations of tyre or contact parameters the observed changes in tyre/road noise are not so much due to changes of the vibrational field on the tyre. Instead variations in the static deflection, which is the basis for the deformed BEM mesh, can simply lead to a change of radiation conditions. This is possibly the case for changes in tyre load, the contact stiffnesses, or when the drum curvature is taken into account.

## **7.2. Future work**

The most important next steps could be summarised as follows:

### **Validation**

This work has shown that it is not possible to assess the validity of rolling resistance and/or rolling noise simulations without measurement data which can be used for validation. Most important are certainly sound pressure level measurements for the tyre. More data which can be used for the validation of the individual simulation steps is also worthwhile to have. Examples are tangential input and transfer

mobilities and mode shape and resonance frequency data for the tyre dynamics, accelerometer measurements for a tyre rolling on a drum for the contact module, or horn-effect measurements for the radiation part.

### **Material parameter estimation**

While the condensation procedure seems to sufficiently accurate, a better procedure for the subsequent fine tuning of material data is needed. Ideally, as many parameters as possible should be obtained by physical reasoning; only the remaining would need to be determined by an automatic procedure such as the genetic algorithm. If the genetic algorithm stays as a part of the optimisation procedure it should be investigated whether better results are obtained by varying the bulk material parameters before the condensation instead of varying the shell stiffnesses after the condensation. Optimisation should also be done independently for crown and sidewall regions.

### **Tyre model**

It is a necessity to introduce non-proportional damping for the rolling resistance simulations. This is not straightforward because of the modal summation procedure which cannot be abandoned. A possible way to solve this problem could be to determine the complex eigenvalues and eigenvectors for the non-proportionally damped system. This allows estimation of the modal damping factors. Using a modal assurance criterion it might be possible to match the complex modes with their respective counterparts in an initially undamped system in which modal summation is possible. During the modal summation the modal damping obtained in the non-proportionally damped system can then be assigned to each mode.

The model is mainly based on shell elements due to computational limitations which existed at the time it was implemented. These limitations are considerably less severe nowadays. For the typical case simulated in this study, the simulation of the tyre response takes less than 1% of the total calculation time. In view of this it is justifiable to base the complete model on solid elements instead. Even if the increased number of degrees-of-freedom doubles or triples the numerical costs, overall computation times would not be affected much. The main benefit with such an approach stems from being able to include the element thickness as an actual geometric property in the mesh. Coupling between elements for the tread and belt can be done without any geometry modification. The error-prone calculation of force and moment resultants during the layer condensation would also no longer be necessary. The only major step which is necessary to implement such a model is to extend the existing solid elements to include pretension effects.

**Contact model**

A short-term requirement is a reliable way to determine the stiffness of the contact springs; preferably without the need for extremely detailed road surface data. Also the relation between contact spring stiffness and static load needs to be better understood. In the long-term damping effects should be included in the springs as well. This would allow for a better estimation of rolling losses due to small-scale tyre/road interaction. So far only normal contact is considered. A logical step is to extend the complete contact formulation to include tangential contact forces as well. This has been partly done in [78], however, without including tangential contact springs.

**Radiation model**

The radiation model does not seem to need further method development. Instead the focus could be put on simulations of absorbing road surfaces and the influence of the circumferential voids on the horn effect.

**Application of the simulation tool**

One of the original goals of this study was to investigate the relation between car tyre rolling losses and rolling noise. This study has shown that it is generally possible to calculate both rolling resistance and tyre/road noise based on the same dynamic tyre model. Problems with the validation of results and uncertainties about the input parameters prevented further detailed analysis of rolling resistance and rolling noise, instead the focus was laid on the influence of modelling parameters on the simulations. The original goal will be pursued further as soon as the model is validated sufficiently.

# A. Reference frames and coordinate systems

## A.1. Reference frames

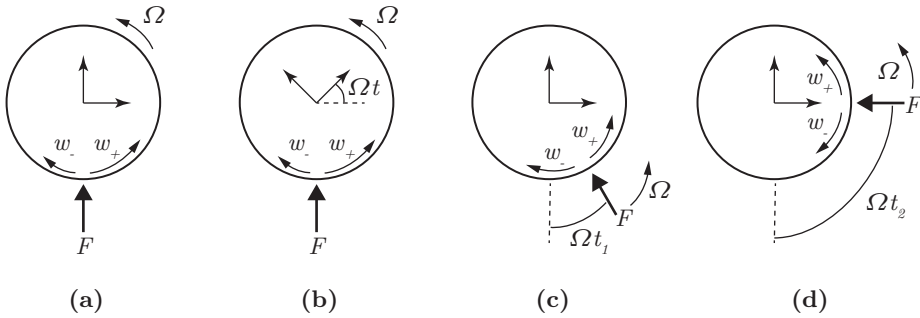


**Fig. A.1.** The Euler and Lagrange reference systems for a tyre rotating at an angular speed  $\Omega$ . (a) Euler reference system, (b) Lagrange reference system as seen by external observer, (c) and (d) Lagrange reference system at two different times  $t_1$  and  $t_2$  as seen by an internal observer.

For all questions relating to the kinematics of bodies, it is essential in which way the reference system is defined in which the physical processes are observed. Generally, there are two options: the first one is the Euler reference system, in which the position of an external observer is assumed who observes the body moving through space. The second alternative is the Lagrange reference system, in which the observer is moving with the body and in which all exterior objects and events are observed as moving relative to the body.

In Fig. A.1 the difference between the two systems is exemplified for the case of a tyre rotating at an angular speed  $\Omega$ . It is assumed that the tyre is in contact with the ground; the resulting force  $F$  excites waves  $w_+$  propagating in the direction of rotation, and waves  $w_-$  propagating against the direction of rotation. In the Euler reference system, case (a) in Fig. A.1, the force is observed as stationary and

the tyre is rotating. This rotation leads to the Doppler effect: the wave lengths of waves travelling in (against) the direction of rotation get longer (shorter). In case (b), the Lagrangian reference system is depicted as it is seen by an outside observer. The coordinate system rotates with the tyre, so that at a time  $t$ , it is rotated by  $\Omega t$  from the initial position. Because this is just an outside view of the Lagrangian system, the Doppler effect is still observed. In (c) and (d) the position of an observer inside the Lagrangian reference system at two different time  $t_1$  and  $t_2$  is taken. In this system the tyre does not rotate, instead the force  $F$  moves around the tyre. At every different time instant the waves  $w_+$  and  $w_-$  are excited at a different position along the tyre circumference. Because the tyre is at rest, the medium of wave propagation also does not move anymore. There is no Doppler effect.

## A.2. Coordinate systems

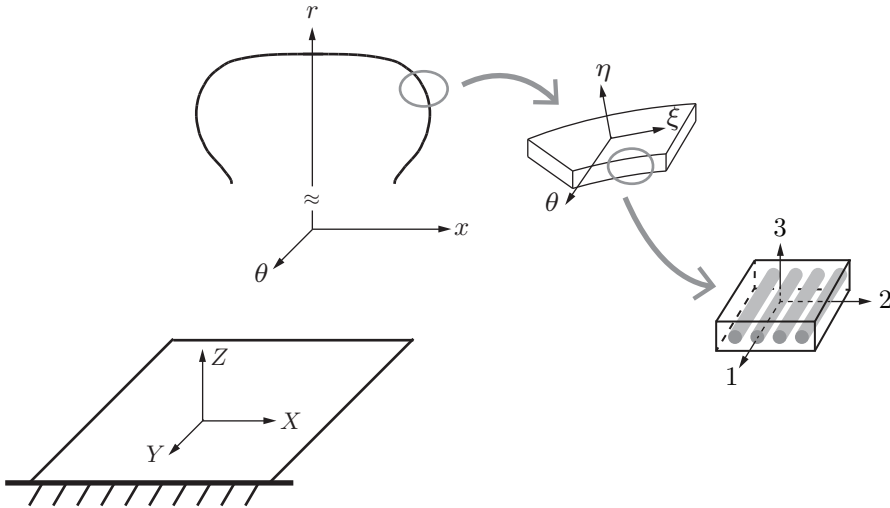


**Fig. A.2.** Overview of the different coordinate systems.

Throughout the different stages of the tyre simulations several coordinate systems are used. As each of them is introduced one at a time in separate parts of this report, it seems useful to present all of them in a condensed form in a common context to avoid confusion. All used coordinate systems are shown in Fig. A.2 and can be described as follows:

**( $X, Y, Z$ )** This is the global cartesian coordinate system in an Eulerian reference frame, i.e. the ground is fixed and the tyre rotates in space. It is used in the modelling of the tyre/road interaction and the radiation.

**( $x, r, \theta$ )** This is a cartesian coordinate system affixed to the tyre. Its origin is placed in the wheel centre and it rotates with the tyre, i.e. it lies in a Lagrangian reference frame. All WFE modelling is performed in this coordinate system. The relation between the  $(x, r, \theta)$  system and an  $(X, Y, Z)$  Eulerian system with origin at the wheel centre is

$$\begin{bmatrix} x \\ r \\ \theta \end{bmatrix} = \begin{bmatrix} 1 & 0 & 0 \\ 0 & \cos \Omega t & \sin \Omega t \\ 0 & -\sin \Omega t & \cos \Omega t \end{bmatrix} \begin{bmatrix} X \\ Y \\ Z \end{bmatrix}. \quad (\text{A.1})$$

Here,  $\Omega$  is the rotational speed of the tyre and  $t$  the time.

**( $\xi, \eta, \theta$ )** The curvilinear coordinate system of an individual condensed waveguide finite element or shell-like individual material layer in the laminate. It is used during the WFE modelling and the derivation of the tyre's material properties. Transformations between this coordinate system and the  $(x, r, \theta)$  system are a fundamental part of the WFEM formulations [75].

**( $1, 2, 3$ )** Material coordinate system for a fibrous composite (i.e. belt or ply layer) which aligns with the composite's principal axes of orthogonality. More specifically, the 1-axis is along the cord direction, the 2-axis is the in-plane normal to the cord direction and the 3-axis is the out of plane direction. It is used during the estimation of the material properties to derive the stress-strain relations in the principal material axes of a fibrous composite layer. The stress-strain relationship in  $(\xi, \eta, \theta)$  coordinates then follows from (5.17).



## B. Genetic algorithm

A genetic algorithm (GA) is a heuristic method for solving multivariable optimisation problems. It mimics the natural selection principal of biological evolution and is based on the concept of *populations* of individual solutions. The optimisation variables are seen as *genes*. Each *individual* of a population represents a certain combination of genes. The solution to the optimisation problem which is given by this gene set is the individual's *fitness*. An initial population is stochastically determined; the following populations are based on repeated modification of the members of the previous population. These modifications are based on a combination of *mutations* and a *survival of the fittest*. The best solutions in each population, i.e. those with the highest *fitness*, are acting a parents for the next generation. Their children are determined by a random mixture of the parents genes. The remaining part of the new population is determined by a stochastically variation of the genes of randomly chosen individuals of the previous population. Over successive generations the population evolves towards an optimal solution. Because of the parent-child concept, the GA is more goal-oriented than a purely stochastic approach. The mutation concept lowers the risk of converging to a local optimum.

A GA is used to optimise the material parameters of the WFEM model after the initial condensation process as described in Cha. 5. This is done using MATLAB's `ga()` command from the *Global Optimization Toolbox* [134]. Variation parameters are all 21 entries of the shell's rigidity matrix, the tread's Young's modulus and the two pretensions. For each variable upper and lower bounds are defined based on physical considerations; in general no variable is allowed to vary by more than a factor of two from the input values. Optimisation is not performed on a per-element basis but rather for the whole structure at once. Several different GA setups were tried; best results were achieved using the residual sum of squares between measured and calculated mobilities as fitness functions

$$SSR = \sum_{\omega_i} (Y_{\text{meas}}(\omega_i) - Y_{\text{GA}}(\omega_i))^2, \quad (\text{B.1})$$

and populations which had 20% crossover children from parents in the previous generation and 70% individuals obtained by random mutation. The remaining 10% are surviving individuals from the previous generation with the highest fitness.



# C. Measurement of tyre mobilities

## C.1. Setup

Input and transfer mobilities were determined for tyre which was freely suspended at the rim as shown in Fig. C.2a. The tyre was inflated to 200 kPa and measurements were done at room temperature. Five different measurement positions over the cross section, see Fig. C.1 were evaluated at circumferential angles of  $0^\circ$  to  $180^\circ$  in  $45^\circ$  steps. At each position one measurement up to 5 kHz with 8192 blocks and one up to 2 kHz with 16384 blocks were done. The used equipment is listed in Tab. C.1.

For the shaker excitation a  $16\text{ mm} \times 16\text{ mm}$  aluminium plate was glued to the tyre, see Fig. C.2b. The force transducer was glued to this plate and connected to the shaker with a stinger. For input mobility measurements the three accelerometers were mounted on three corners of the aluminium plate to account for possible moment excitation. For all other measurements the transducers were directly glued to the tyre as shown in Fig. C.2c.

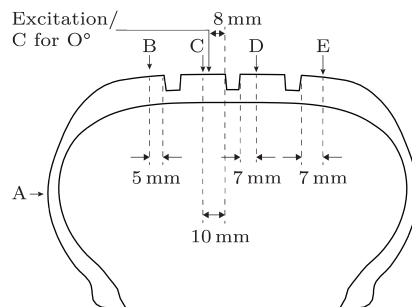


**Fig. C.1.** Position of measurement positions A to E and excitation point on tyre cross section. Position A is located 120 mm from the beginning of the centre void.

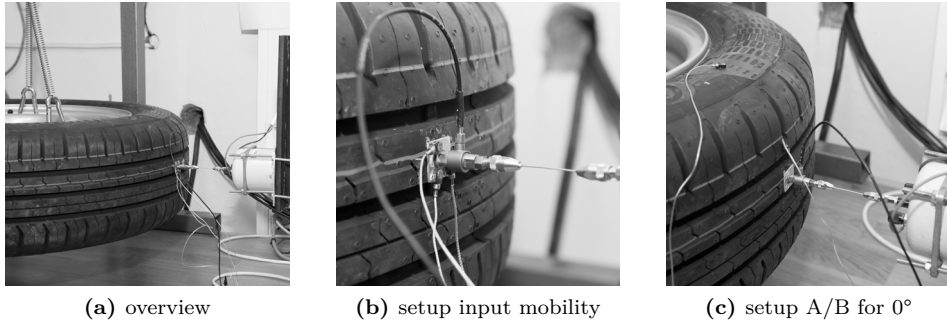


**Fig. C.2.** Pictures of measurement setup.

**Tab. C.1.** Measurement equipment. The accelerometer marked with \* had a constant offset of 2 dB which was corrected in post-processing.

item	type (serial #)	item	type (serial #)
force transd.	B&K 8203 (2173101)	shaker	LDS V102 (5181910)
accelerometer	Endevco 25B (ED24)	charge ampl.	B&K 2635 (872470)
accelerometer	Endevco 25B (ED27)	amplifier	NAD 3020 (A3268993)
accelerometer	Endevco 25B* (ED28)	acquis. system	VXI E84084

## C.2. Measurement results

Coherences and mobilities are shown in Figs. C.4 to C.8 together with simulated mobilities. These were obtained using the standard tyre configuration with original material values (i.e. directly from condensation) and with optimised material values. In the simulations the rim is not freely suspended, but fixed. Due to this all simulated mobilities apart from those for  $90^\circ$  have an additional peak at 86 Hz. This peak is caused by a semi-rigid body mode shown in Fig. C.3. Coherences are above 0.9 from 90 Hz to 1.6 kHz (55 Hz to 2 kHz for  $0^\circ$ ).

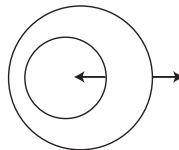


**Fig. C.3.** Translational semi-rigid body mode.

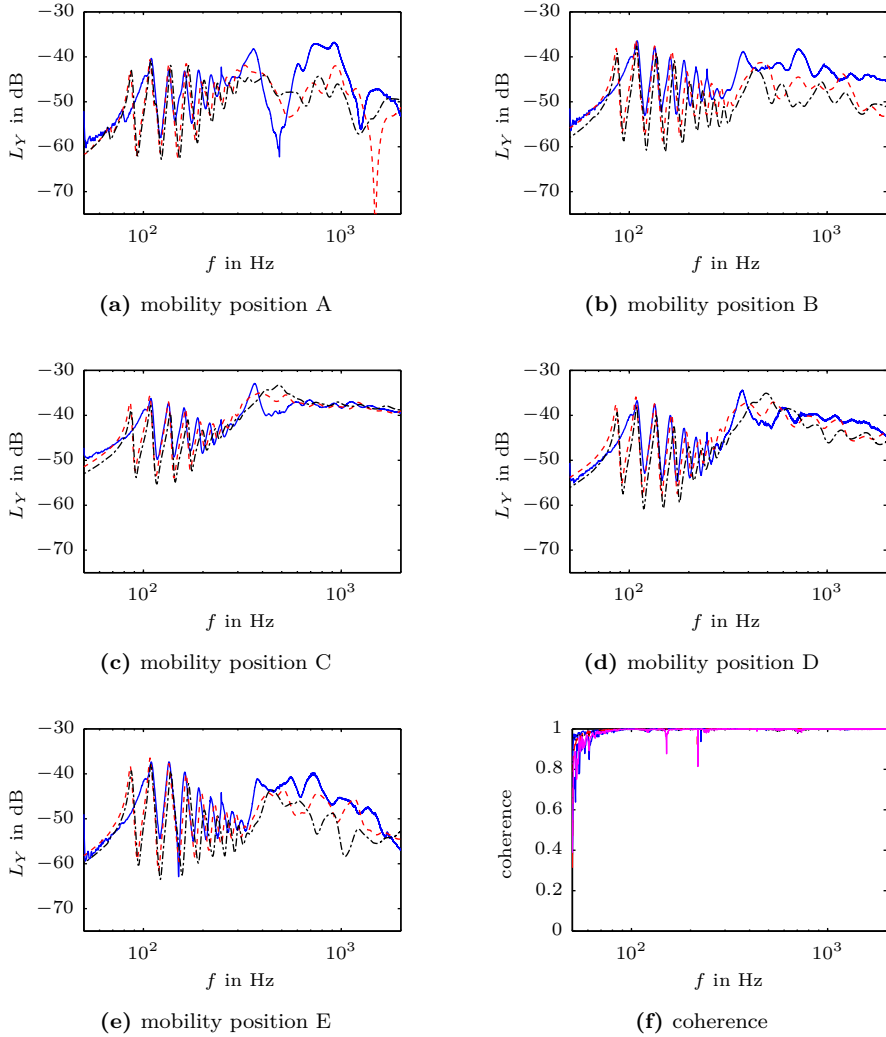


**Fig. C.4.** (a) to (e): Comparison of mobilities from measurement (—), WFEM original (---) and WFEM optimised material parameters (— · —) for lateral positions A to E and a circumferential angle of  $0^\circ$ , with  $L_Y = 20 \log_{10}(|Y/Y_0|)$ ,  $Y_0 = 1 \text{ N}/(\text{ms})$ . (f): Measured coherences positions A (—), B (— · —), C (— · · —), D (····) and E (— · —).

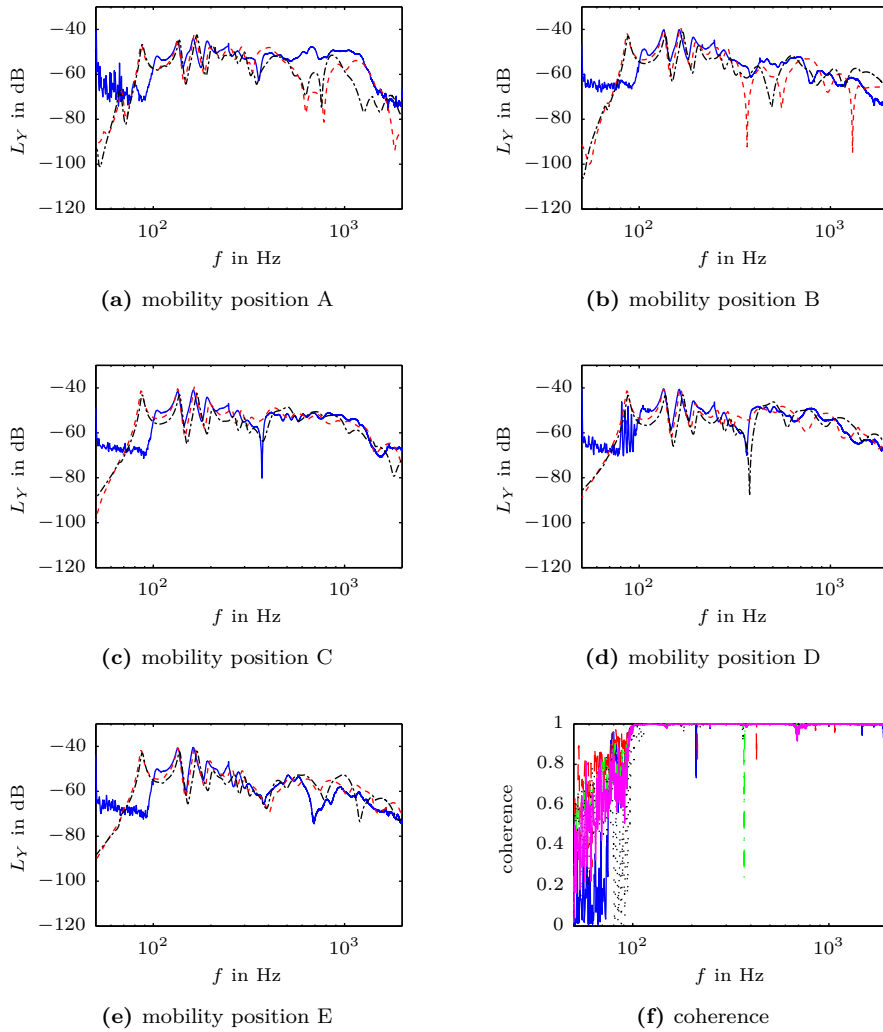


**Fig. C.5.** (a) to (e): Comparison of mobilities from measurement (—), WFEM original (---) and WFEM optimised material parameters (— · —) for lateral positions A to E and a circumferential angle of  $45^\circ$ , with  $L_Y = 20 \log_{10}(|Y/Y_0|)$ ,  $Y_0 = 1 \text{ N}/(\text{ms})$ . (f): Measured coherences positions A (—), B (— · —), C (---), D (····) and E (— · —).

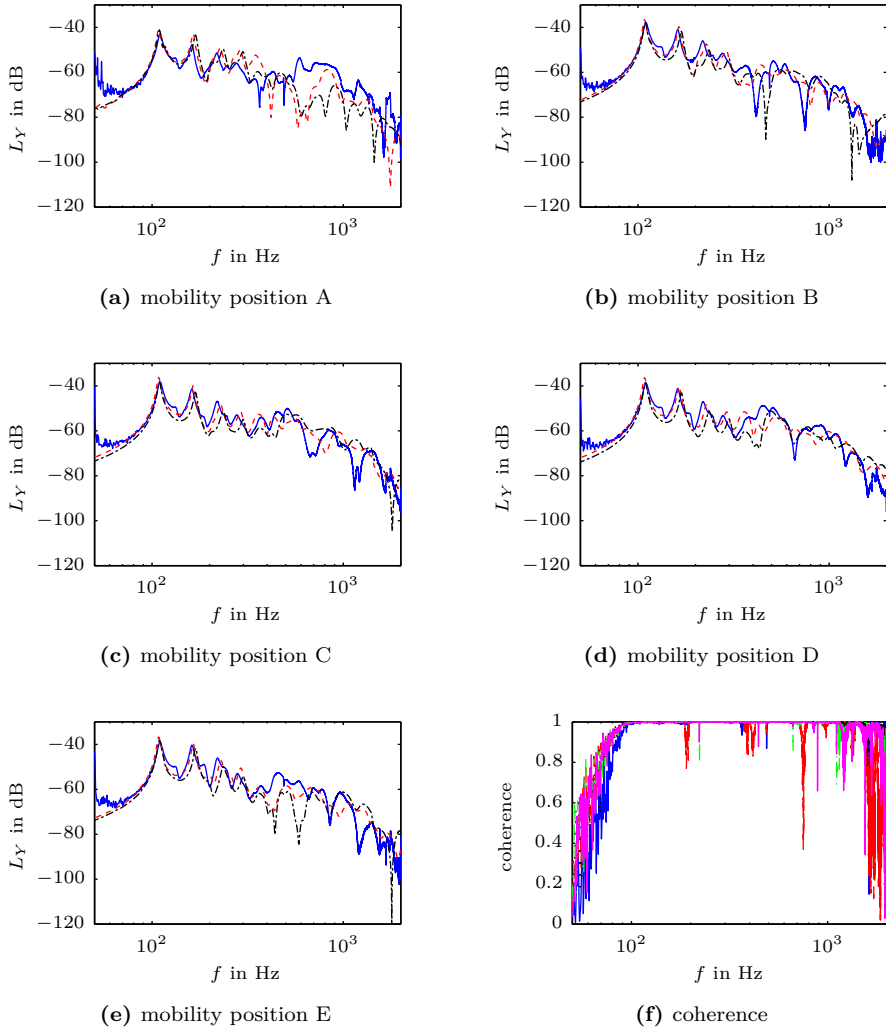


**Fig. C.6.** (a) to (e): Comparison of mobilities from measurement (—), WFEM original (---) and WFEM optimised material parameters (— · —) for lateral positions A to E and a circumferential angle of  $90^\circ$ , with  $L_Y = 20 \log_{10}(|Y/Y_0|)$ ,  $Y_0 = 1 \text{ N/(ms)}$ . (f): Measured coherences positions A (—), B (— · —), C (— · · —), D (····) and E (— · —).

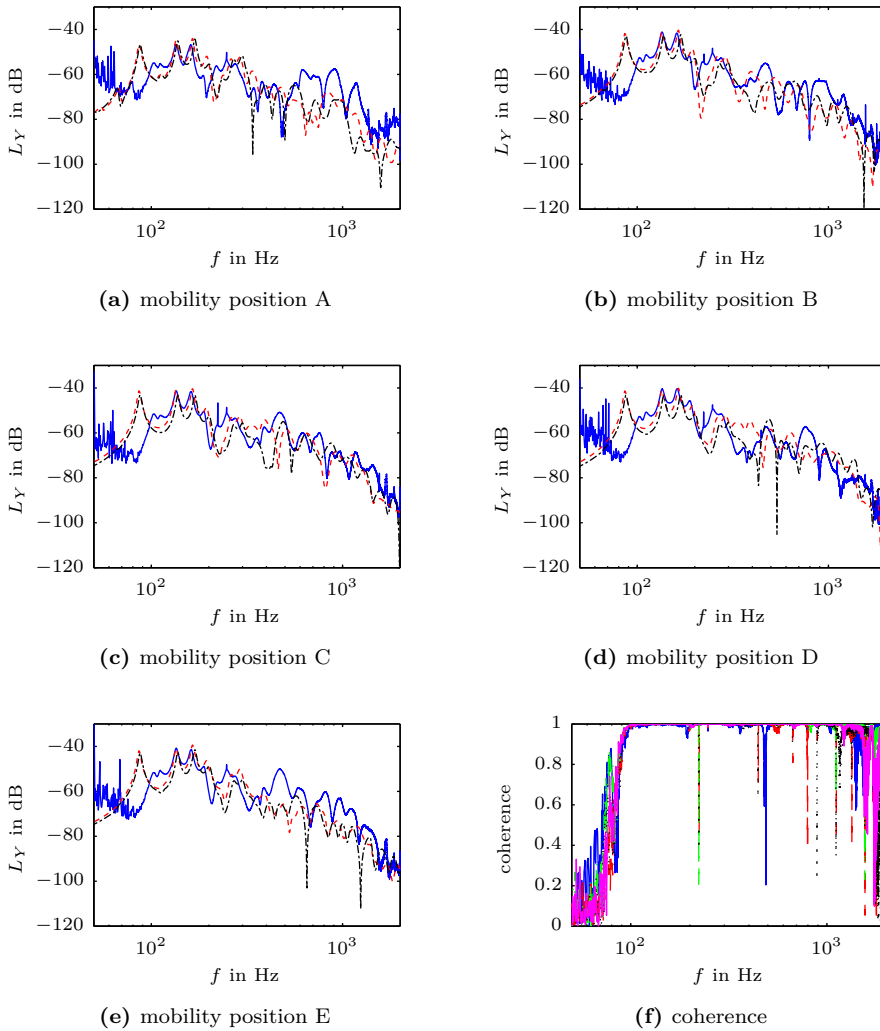


**Fig. C.7.** (a) to (e): Comparison of mobilities from measurement (—), WFEM original (---) and WFEM optimised material parameters (— · —) for lateral positions A to E and a circumferential angle of  $135^\circ$ , with  $L_Y = 20 \log_{10}(|Y/Y_0|)$ ,  $Y_0 = 1 \text{ N}/(\text{ms})$ . (f): Measured coherences positions A (—), B (— · —), C (— · · —), D (····) and E (— · —).

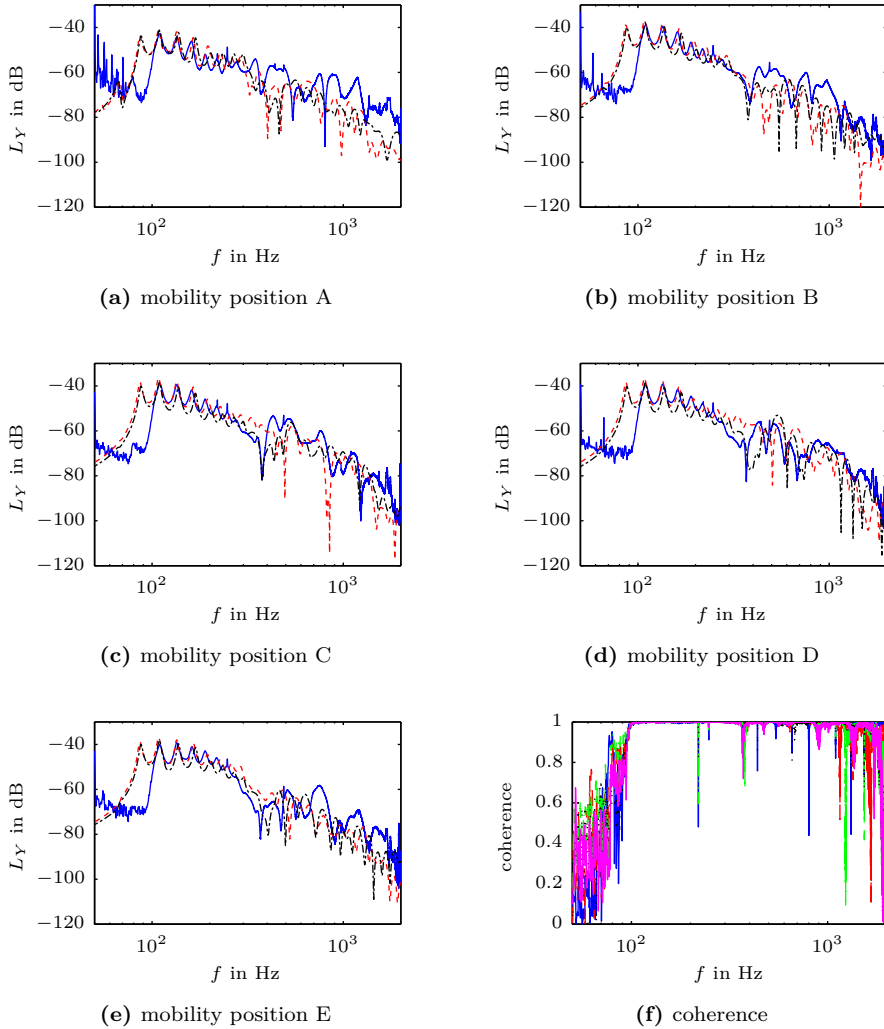


**Fig. C.8.** (a) to (e): Comparison of mobilities from measurement (—), WFEM original (---) and WFEM optimised material parameters (— · —) for lateral positions A to E and a circumferential angle of  $180^\circ$ , with  $L_Y = 20 \log_{10}(|Y/Y_0|)$ ,  $Y_0 = 1 \text{ N}/(\text{ms})$ . (f): Measured coherences positions A (—), B (---), C (— · —), D (·· ·) and E (— · —).



# References

- [1] Annual European Community greenhouse gas inventory 1990–2006 and inventory report 2008, Technical Report No 6/2008, European Commission, DG Environment; European Environment Agency, 2008.
- [2] Inventory of U.S. greenhouse gas emissions and sinks: 1990 – 2008, Technical Report EPA 430-R-10-006, U.S. Environmental Protection Agency, 2010.
- [3] J. Barrand, J. Bokar, Reducing tire rolling resistance to save fuel and lower emissions, *SAE International Journal of Passenger Cars - Mechanical Systems* 1 (2009) 9–17.
- [4] Tires and Passenger Vehicle Fuel Economy: Informing Consumers, Improving Performance, Technical Report 286, Committee for the National Tire Efficiency Study, Transportation Research Board, Board on Energy and Environmental Systems, 2006.
- [5] G. Fontaras, Z. Samaras, On the way to 130 g CO<sub>2</sub>/km — estimating the future characteristics of the average european passenger car, *Energy Policy* 38 (2010) 1826–1833. *Energy Security - Concepts and Indicators with regular papers*.
- [6] N. Demirdöven, J. Deutch, Hybrid cars now, fuel cell cars later, *Science* 305 (2004) 974–976.
- [7] Burden of disease from environmental noise - Quantification of healthy life years lost in Europe, Technical Report, WHO, 2011.
- [8] L. den Boer, A. Schrotten, Traffic noise reduction in Europe, Technical Report 07.4451.27, CE Delft, 2007.
- [9] W. van Keulen, M. Duškov, Inventory study of basic knowledge on tyre/road noise, Project report DWW-2005-022, IPG, 2005.
- [10] Regulation (EC) No 1222/2009 of the European Parliament and of the Council of 25 November 2009 on the labelling of tyres with respect to fuel efficiency and other essential parameters, *Official Journal L* 342, 22/12/2009.
- [11] [http://ec.europa.eu/energy/efficiency/tyres/labelling\\_en.htm](http://ec.europa.eu/energy/efficiency/tyres/labelling_en.htm), accessed 23 August 2012.

- 
- [12] International Organization for Standardization ISO 18164:2005 passenger car, truck, bus and motorcycle tyres — methods of measuring rolling resistance, 2005.
- [13] A. Gent, J. Walter (Eds.), *The pneumatic tire*, U.S. Department of Transportation, National Highway Traffic Safety Administration, 2006.
- [14] D. Hall, J. Moreland, Fundamentals of rolling resistance, *Rubber Chemistry and Technology* 74 (2001) 525–539.
- [15] A. Nashif, D. Jones, J. Henderson, *Vibration damping*, Wiley-Interscience, 1985.
- [16] S. Bandyopadhyay, A. Chandra, R. Mukhopadhyay, An overview of tyre rolling loss, *Progress in rubber and plastics technology* 10 (1994) 20–53.
- [17] *The International System of Units (SI)*, 2006.
- [18] U. Sandberg, J. Ejsmont, *Tyre/road noise reference book*, Informex, Kisa, Sweden, 2002.
- [19] M. Heckl, Tyre noise generation, *Wear* 113 (1986) 157–170.
- [20] R. Pinnington, A. Briscoe, A wave model for a pneumatic tyre belt, *Journal of Sound and Vibration* 253 (2002) 941–959.
- [21] K. Larsson, W. Kropp, A high-frequency three-dimensional tyre model based on two coupled elastic layers, *Journal of Sound and Vibration* 253 (2002) 889–908.
- [22] P. Andersson, K. Larsson, F. Wullens, W. Kropp, High frequency dynamic behaviour of smooth and patterned passenger car tyres, *Acta Acustica united with Acustica* 90 (2004) 445–456.
- [23] T. Sakata, H. Morimura, H. Ide, Effects of tire cavity resonance on vehicle road noise, *Tire Science and Technology* 18 (1990) 68–79.
- [24] D. Ronneberger, Experimentelle und theoretische Untersuchung spezieller Mechanismen der Rollgeräuschestehung und -abstrahlung, *Mitteilung* 57, Institut für Straßen-, Eisenbahn- und Felsbau der E.T.H. Zürich, 1984. Pp. 79–116.
- [25] N. Nilsson, O. Bennerhult, S. Söderqvist, Air-resonant radiation - a possible mechanism for high frequency noise from cross-bar tires, IFM Research Report 6.084.02, IFM Akustikbyrån AB, 1979.

- 
- [26] W. Kropp, F.-X. Becot, S. Barrelet, On the sound radiation from tyres, *Acta Acustica united with Acustica* 86 (2000) 769–779.
- [27] R. Graf, C.-Y. Kuo, A. Dowling, W. Graham, On the horn effect of a tyre/road interface, part I: Experiment and computation, *Journal of Sound and Vibration* 256 (2002) 417–431.
- [28] E.-U. Saemann, H. Schmidt, Schallmessungen bei der Entwicklung von Reifen mit geringem Vorbeifahrtpegel, *Zeitschrift für Lärmbekämpfung* 49 (2002) 59–62.
- [29] J. Ejsmont, Tire/road noise and rolling resistance - Is there a trade-off?, in: U. Sandberg (Ed.), *International Tire/Road Noise Conference 1990 (INTROC 90)*, 8-10 August 1990, Gothenburg, Sweden, volume 1, pp. 439–452.
- [30] U. Sandberg, J. Ejsmont, Noise emission, friction and rolling resistance of car tires - Summary of an experimental study, in: *Proceedings of the 2000 National Conference on Noise Control Engineering (NOISE-CON 2000)* 2000 Dec. 3-5, Newport Beach, California, USA.
- [31] R. Stenschke, P. Vietzke, Noise and use characteristics of modern car tyres (state of the art), in: *Seventh International Congress on Sound and Vibration*, 4-7 July 2000, Garmisch-Partenkirchen, Germany, pp. 2781–2788.
- [32] S. Boere, I. Lopez, A. Kuijpers, H. Nijmeijer, Prediction of road texture influence on rolling resistance and tyre/road noise, in: *Proceedings of Euronoise 2009*, Edinburgh, United Kingdom, 2009 October 26-28.
- [33] O. Bschorr, A. Wolf, Reifenschwingungen als Ursache von Lärm und Rollwiderstand, *Automobil-Industrie* 27 (1982) 451–458.
- [34] A. J. P. Mieke, A. A. Popov, The rolling resistance of truck tyres under a dynamic vertical load, *Vehicle System Dynamics: International Journal of Vehicle Mechanics and Mobility* 43 (2005) 135–144.
- [35] M. Fraggstedt, *Vibrations, damping and power dissipation in car tyres*, Phd thesis, KTH Royal Institute of Sciences, Stockholm, 2008.
- [36] P. Pillai, Total tire energy loss comparison by the whole tire hysteresis and the rolling resistance methods, *Tire Science and Technology* 23 (1995) 256–265.
- [37] L. Yam, J. Shang, D. Guan, A. Zhang, Study on tyre rolling resistance using experimental modal analysis, *International Journal of Vehicle Design* 30 (2002) 251–262.

- 
- [38] D. Stutts, W. Soedel, A simplified dynamic model of the effect of internal damping on the rolling resistance in pneumatic tires, *Journal of Sound and Vibration* 155 (1992) 153 – 164.
- [39] S. Kim, A. Savkoor, The contact problem of in-plane rolling of tires on a flat road, *Vehicle System Dynamics* 27 (1997) 189–206.
- [40] A. J. P. Miège, A. A. Popov, Truck tyre modelling for rolling resistance calculations under a dynamic vertical load., *Proceedings of the Institution of Mechanical Engineers – Part D – Journal of Automobile Engineering* 219 (2005) 441–456.
- [41] H. Park, S.-K. Youn, T. Song, N.-J. Kim, Analysis of temperature distribution in a rolling tire due to strain energy dissipation, *Tire Science and Technology* 25 (1997) 214–228.
- [42] K. V. N. Rao, R. K. Kumar, P. C. Bohara, A sensitivity analysis of design attributes and operating conditions on tyre operating temperatures and rolling resistance using finite element analysis., *Proceedings of the Institution of Mechanical Engineers – Part D – Journal of Automobile Engineering* 220 (2006) 501 – 517.
- [43] Y.-J. Lin, S.-J. Hwang, Temperature prediction of rolling tires by computer simulation, *Mathematics and Computers in Simulation* 67 (2004) 235–249.
- [44] P. Ghosh, A. Saha, R. Mukhopadhyay, Prediction of tyre rolling resistance using fea, in: J. Busfield, A. Muhr (Eds.), *Constitutive Models for Rubber III*.
- [45] J. Luchini, J. Peters, R. Arthur, Tire rolling loss computation with the finite element method, *Tire Science and Technology* 22 (1994) 206–222.
- [46] G. Descornet, U. Sandberg, Road surface influence on tire/road noise - Part II, in: *Proceedings Internoise 80*, Miami, Florida, USA, 8-10 December, 1980, pp. 267–272.
- [47] U. Sandberg, G. Descornet, Road surface influence on tire/road noise - Part I, in: *Proceedings Internoise 80*, Miami, Florida, USA, 8-10 December, 1980, pp. 259–266.
- [48] T. Beckenbauer, A. Kuijpers, Prediction of pass-by levels depending on road surface parameters by means of a hybrid model, in: [135], pp. 2611–2616.
- [49] A. Kuijpers, G. van Blokland, Tyre/road noise models in the last two decades: a critical evaluation, in: *The 2001 International Congress and Exhibition on Noise Control Engineering* The Hague, The Netherlands, 2001 August 27-30.

- 
- [50] F. Böhm, Mechanik des Gürtelreifens, *Archive of Applied Mechanics* 35 (1966) 82–101.
- [51] L. Kung, W. Soedel, T. Yang, Free vibration of a pneumatic tire-wheel unit using a ring on an elastic foundation and a finite element model, *Journal of Sound and Vibration* 107 (1986) 181–194.
- [52] W. Kropp, Structure-borne sound on a smooth tyre, *Applied Acoustics* 26 (1989) 181–192.
- [53] P. Kindt, P. Sas, W. Desmet, Development and validation of a three-dimensional ring-based structural tyre model, *Journal of Sound and Vibration* 326 (2009) 852 – 869.
- [54] A. Tsotras, On the interaction between modal behaviour and contact force development of a pneumatic tyre, Phd thesis, Loughborough University, 2010.
- [55] W. Kropp, A mathematical model of tyre noise generation, *International Journal of Vehicle Design* 6 (1999) 310–329.
- [56] F. Wullens, Excitation of tyre vibrations due to tyre/road interaction, Ph.D. thesis, Chalmers University of Technology, Gothenburg, 2004.
- [57] Y. Kim, J. Bolton, Modelling tyre treadband vibration, in: [135].
- [58] J. M. Muggleton, B. R. Mace, M. J. Brennan, Vibrational response prediction of a pneumatic tyre using an orthotropic two-plate wave model, *Journal of Sound and Vibration* 264 (2003) 929–950.
- [59] D. O’Boy, A. Dowling, Tyre/road interaction noise—numerical noise prediction of a patterned tyre on a rough road surface, *Journal of Sound and Vibration* 323 (2009) 270 – 291.
- [60] R. J. Pinnington, Radial force transmission to the hub from an unloaded stationary tyre, *Journal of Sound and Vibration* 253 (2002) 961–983.
- [61] R. Pinnington, A wave model of a circular tyre. Part 1: belt modelling, *Journal of Sound and Vibration* 290 (2006) 101–132.
- [62] R. Pinnington, A wave model of a circular tyre. Part 2: side-wall and force transmission modelling, *Journal of Sound and Vibration* 290 (2006) 133–168.
- [63] C. Lecomte, W. Graham, M. Dale, A shell model for tyre belt vibrations, *Journal of Sound and Vibration* 329 (2010) 1717–1742.

- 
- [64] Y. B. Chang, T. Y. Yang, W. Soedel, Dynamic analysis of a radial tire by finite elements and modal expansion, *Journal of Sound and Vibration* 96 (1984) 1–11.
- [65] S. Saigal, T. Y. Yang, H. W. Kim, W. Soedel, Free vibrations of a tire as a toroidal membrane, *Journal of Sound and Vibration* 107 (1986) 71–82.
- [66] T. Richards, Finite element analysis of structural-acoustic coupling in tyres, *Journal of Sound and Vibration* 149 (1991) 235–243.
- [67] M. Brinkmeier, U. Nackenhorst, H. Volk, A finite element approach to the transient dynamics of rolling tires with emphasis on rolling noise simulation, *Tire Science and Technology* 35 (2007) 165–182.
- [68] A. Pietrzyk, Prediction of the dynamic response of a tyre, in: [135].
- [69] A. Fadavi, D. Duhamel, H. Yin, Tyre/road noise: Finite element modelling of tyre vibrations, in: [135].
- [70] I. Lopez, R. Blom, N. Roozen, H. Nijmeijer, Modelling vibrations on deformed rolling tyres—a modal approach, *Journal of Sound and Vibration* 307 (2007) 481–494.
- [71] I. Lopez, Influence of material damping on the prediction of road texture and tread pattern related rolling resistance, in: P. Sas, B. Bergen (Eds.), *Proceedings of the International Conference on Noise and Vibration Engineering ISMA 2010*, Katholieke Universiteit Leuven, Leuven, Belgium, pp. 4039–4052.
- [72] M. Brinkmeier, U. Nackenhorst, S. Petersen, O. von Estorff, A finite element approach for the simulation of tire rolling noise, *Journal of Sound and Vibration* 309 (2008) 20–39.
- [73] J. Biermann, O. von Estorff, S. Petersen, H. Schmidt, Computational model to investigate the sound radiation from rolling tires, *Tire Science and Technology* 35 (2007) 209–225.
- [74] C.-M. Nilsson, Waveguide finite elements applied on a car tyre, Ph.D. thesis, KTH Royal Institute of Sciences, Stockholm, 2004.
- [75] S. Finnveden, M. Fraggstedt, Waveguide finite elements for curved structures, *Journal of Sound and Vibration* 312 (2008) 644–671.
- [76] E. Rustighi, S. Elliott, S. Finnveden, K. Gulyás, T. Mócsai, M. Danti, Linear stochastic evaluation of tyre vibration due to tyre/road excitation, *Journal of Sound and Vibration* 310 (2008) 1112–1127.

- 
- [77] P. Sabiniarz, W. Kropp, A waveguide finite element aided analysis of the wave field on a stationary tyre, not in contact with the ground, *Journal of Sound and Vibration* 329 (2010) 3041–3064.
- [78] P. Sabiniarz, Modelling the vibrations on a rolling tyre and their relation to exterior and interior noise, Ph.D. thesis, Chalmers University of Technology, Gothenburg, 2011.
- [79] W. Kropp, P. Sabiniarz, H. Brick, T. Beckenbauer, On the sound radiation of a rolling tyre, *Journal of Sound and Vibration* 331 (2012) 1789–1805.
- [80] Y. Waki, B. Mace, M. Brennan, Free and forced vibrations of a tyre using a wave/finite element approach, *Journal of Sound and Vibration* 323 (2009) 737–756.
- [81] Y. Waki, B. Mace, M. Brennan, Numerical issues concerning the wave and finite element method for free and forced vibrations of waveguides, *Journal of Sound and Vibration* 327 (2009) 92 – 108.
- [82] D. Duhamel, S. Erlicher, H. Nguyen, A recursive finite element method for computing tyre vibrations, *European Journal of Computational Mechanics* 20 (2011) 9–27.
- [83] T. Clapp, A. Eberhardt, C. Kelley, Development and validation of a method for approximating road surface textureinduced contact pressure in tirepavement interaction, *Tire Science and Technology* 16 (1988) 2–17.
- [84] G. Dubois, J. Cesbron, H. Yin, F. Anfosso-Lédée, Macro-scale approach for rough frictionless multi-indentation on a viscoelastic half-space, *Wear* 272 (2011) 69–78.
- [85] J. Winroth, P. Andersson, Influence of tread inertia during deformation using a detailed numerical tyre/road contact model, in: [136], pp. 2431–2436.
- [86] H.-P. Yin, G. Dubois, J. Cesbron, F. Anfosso-Lédée, Q.-H. Bui, D. Duhamel, A numerical macro-scale approach for the tire/road viscoelastic contact for the noise prediction, in: [137].
- [87] M. McIntyre, J. Woodhouse, On the fundamentals of bowed string dynamics, *Acustica* 43 (1979) 93–108.
- [88] W. Kropp, Ein Modell zur Beschreibung des Rollgeräusches eines unprofilierten Gürtelreifens auf rauher Straßenoberfläche, number 166 in *Fortschrittberichte VDI, Reihe 11: Schwingungstechnik*, VDI Verlag, 1992.

- [89] K. Larsson, S. Barrelet, W. Kropp, The modelling of the dynamic behaviour of tyre tread blocks, *Applied Acoustics* 63 (2002) 659–677.
- [90] F. Wullens, W. Kropp, A three-dimensional contact model for tyre/road interaction in rolling conditions, *Acta Acustica united with Acustica* 90 (2004) 702–711.
- [91] P. Andersson, W. Kropp, Time domain contact model for tyre/road interaction including nonlinear contact stiffness due to small-scale roughness, *Journal of Sound and Vibration* 318 (2008) 296–312.
- [92] J.-F. Hamet, P. Klein, Road texture and tire noise, in: *Proceedings Inter-noise 2000*, 27-30 August 2000, Nice, France, pp. 178–183.
- [93] R. Graf, Tyre-road interaction noise, Ph.D. thesis, University of Cambridge, 2002.
- [94] F. Liu, M. Sutcliffe, W. Graham, Prediction of tread block forces for a free-rolling tyre in contact with a smooth road, *Wear* 269 (2010) 672–683.
- [95] I. Lopez Arteaga, Green’s functions for a loaded rolling tyre, *International Journal of Solids and Structures* 48 (2011) 3462–3470.
- [96] S. Kim, P. Nikraves, G. Gim, A two-dimensional tire model on uneven roads for vehicle dynamic simulation, *Vehicle System Dynamics* 46 (2008) 913–930.
- [97] R. F. Keltie, Analytical model of the truck tire vibration sound mechanism, *The Journal of the Acoustical Society of America* 71 (1982) 359–367.
- [98] F.-X. Bécot, Tyre noise over impedance surfaces - Efficient application of the equivalent sources method, Ph.D. thesis, Chalmers University of Technology, INSA Lyon, 2003.
- [99] E.-J. Ni, D. S. Snyder, G. F. Walton, N. E. Mallard, G. E. Barron, J. T. Browell, B. N. Aljundi, Radiated noise from tire/wheel vibration, *Tire Science and Technology* 25 (1997) 29–42.
- [100] H. Brick, Application of the Boundary Element Method to combustion noise and half-space problems, Ph.D. thesis, Chalmers University of Technology, 2009.
- [101] W. Graham, Influence of tire geometry on the horn effect, in: [137].
- [102] D. Brunner, Fast Boundary Element Methods for Large-Scale Simulations of the Vibro-Acoustic Behavior of Ship-Like Structures, Ph.D. thesis, Universität Stuttgart, 2009.

- 
- [103] S. Keuchel, M. Gehlken, O. von Estorff, Analyse zweier Halbraum-Formulierungen zur Lösung der Helmholtz-Gleichung mittels der Fast-Multipole-Boundary-Elemente-Methode, in: [138], pp. 183–184.
- [104] C. Bückers, U. Stöckert, Quiet Road Traffic 3 - An interdisciplinary approach to reduce the noise emission at the source, in: [139].
- [105] C.-Y. Kuo, R. Graf, A. Dowling, W. Graham, On the horn effect of a tyre/road interface, part ii: Asymptotic theories, *Journal of Sound and Vibration* 256 (2002) 433–445.
- [106] M. Fraggstedt, Power dissipation in car tyres, Licentiate thesis, KTH Royal Institute of Sciences Stockholm, 2006.
- [107] D. Duhamel, B. Mace, M. Brennan, Finite element analysis of the vibrations of waveguides and periodic structures, *Journal of Sound and Vibration* 294 (2006) 205–220.
- [108] L. Gavric, Computation of propagative waves in free rail using a finite element technique, *Journal of Sound and Vibration* 185 (1995) 531–543.
- [109] A. Pieringer, Time-domain modelling of high-frequency wheel/rail interaction, Ph.D. thesis, Chalmers University of Technology, Gothenburg, 2011.
- [110] Y. Fung, P. Tong, Classical and computational solid mechanics, World Scientific, 2001.
- [111] K. Larsson, Modelling of dynamic contact - Exemplified on the tyre/road interaction, Ph.D. thesis, Chalmers University of Technology, 2002.
- [112] R. Ciskowski, C. Brebbia (Eds.), *Boundary Element Methods in Acoustics, Computational Mechanics Publications*, Co-published with Elsevier Applied Science, Southampton, Boston, London, New York, 1991.
- [113] L. Cremer, M. Heckl, B. Petersson, *Structure-Borne-Sound*, Springer-Verlag, 3rd edition, 2005.
- [114] Y. J. Kim, J. S. Bolton, Effects of rotation on the dynamics of a circular cylindrical shell with application to tire vibration, *Journal of Sound and Vibration* 275 (2004) 605 – 621.
- [115] C. González Díaz, P. Kindt, S. Vercammen, J. Middelberg, C. Thiry, J. Leysens, Effects of rotation on the tyre dynamic behaviour under different operating conditions, in: [139], pp. 920–925.

- 
- [116] S. Vercammen, C. González Díaz, P. Kindt, C. Thiry, J. Middelberg, J. Leysens, Dynamic behavior of rolling tires under different operating conditions, in: [137].
- [117] C. Hoever, P. Sabiniarz, W. Kropp, Waveguide-finite-element based parameter study of car tyre rolling losses, in: [136], pp. 789–794.
- [118] C. Hoever, W. Kropp, A simulation-based parameter study of car tyre rolling losses and sound generation, in: [139], pp. 926–931.
- [119] Tyre Basics Passenger Car Tyres, Technical Report 0130 1607, Continental Reifen Deutschland, 2012.
- [120] D. O’Boy, A. Dowling, Tyre/road interaction noise—A 3D viscoelastic multilayer model of a tyre belt, *Journal of Sound and Vibration* 322 (2009) 829–850.
- [121] K. Altena, WFEM applied to a car tyre, Master’s thesis, TU Delft, 2007.
- [122] W. Soedel, *Vibrations of Shells and Plates*, Marcel Dekker, New York, 3rd edition, 2004.
- [123] J. Halpin, *Primer on composite materials analysis*, Technomic Publishing Company, Lancaster, Basel, 2nd edition, 1992.
- [124] R. Jones, *Mechanics of composite materials*, Taylor & Francis, Philadelphia, 2nd edition, 1999.
- [125] ABAQUS/Standard User’s Manual Version 5.8, Hibbitt, Karlsson & Sorensen, Pawtucket, USA, 1998.
- [126] S. Finnveden, C.-M. Nilsson, Waveguide Finite Elements for Analysis of Car Tyre Vibrations, Technical Report RATIN Deliverable D1.2.3, 2003.
- [127] M. Petyt, *Introduction to finite element vibration analysis*, Cambridge University Press, Cambridge, 1990.
- [128] International Organization for Standardization ISO 10844:2011 acoustics – specification of test tracks for measuring noise emitted by road vehicles and their tyres, 2011.
- [129] D. Schuring, The rolling loss of pneumatic tires, *Rubber Chemistry and Technology* 53 (1980) 600–727.
- [130] M. Roovers, D. de Graff, R. van Moppes, Round Robin Test Rolling Resistance / Energy Consumption, Technical Report DWW-2005-046, IPG, 2005.

- 
- [131] D. Schuring, J. Clark, Load, speed, and pressure effects on passenger car tire rolling-loss distribution, *Rubber Chemistry and Technology* 61 (1988) 669–687.
- [132] J. Wong, *Theory of Ground Vehicles*, John Wiley & Sons, 3rd edition, 2012.
- [133] E.-U. Saemann, Innovative Reifen für grüne Stadtautos, in: [138], pp. 959–960.
- [134] Global optimization toolbox, <http://www.mathworks.se/products/global-optimization/index.html>, accessed 11 November 2012.
- [135] *Internoise 2001*, The 2001 International Congress and Exhibition on Noise Control Engineering, The Hague, The Netherlands, 2001 August 27-30, 2001.
- [136] *Proceedings 6th Forum Acusticum*, Aalborg, Denmark, 2011, EAA, 2011.
- [137] *Proceedings of the Internoise 2012/ASME NCAD meeting* August 19-22, 2012, New York City, NY, USA, 2012.
- [138] *DAGA 2012*, Fortschritte der Akustik, 38. Deutsche Jahrestagung für Akustik, 19.–22. März 2012, Darmstadt, Deutsche Gesellschaft für Akustik e.V. (DEGA), Deutsche Gesellschaft für Akustik e.V. (DEGA), 2012.
- [139] *Euronoise Prague 2012*, 10-13 June 2012, European Acoustics Association (EAA), European Acoustics Association (EAA), 2012.

